

Alma Mater Studiorum – Università di Bologna

**DOTTORATO DI RICERCA IN  
SCIENZE CHIMICHE**

Ciclo XXVI

**Settore Concorsuale di afferenza:** 03/A2 MODELLI E METODOLOGIE PER LE  
SCIENZE CHIMICHE

**Settore Scientifico disciplinare:** CHIM/02 CHIMICA FISICA

**MODELING AND SIMULATIONS OF  
NANOPARTICLES  
IN LIQUID CRYSTALLINE SYSTEMS**

Presentata da: ERIKA BENINI

Coordinatore Dottorato:

Prof. ALDO RODA

Relatore:

Prof. CLAUDIO ZANNONI

Correlatori:

Dr.ssa SILVIA ORLANDI

Dr. MATTEO RICCI

**Esame finale anno 2014**





# Contents

<b>Introduction</b>	<b>2</b>
<b>1 Liquid Crystals and Nanoparticles</b>	<b>5</b>
1.1 Liquid Crystals . . . . .	5
1.1.1 Nematic mesophases . . . . .	6
1.1.2 Smectic mesophases . . . . .	7
1.1.3 Blue phases . . . . .	9
1.1.4 Discotic columnar phases . . . . .	10
1.2 Doping LC with nanoparticles . . . . .	12
1.3 Theoretical background . . . . .	20
<b>2 Computer simulations</b>	<b>21</b>
2.1 Introduction . . . . .	21
2.2 Monte Carlo simulations . . . . .	22
2.3 Molecular Dynamics . . . . .	26
2.4 Microscopic Models . . . . .	28
2.4.1 Gay–Berne coarse grained model . . . . .	30
2.4.2 Models for LC–NP systems . . . . .	32
<b>3 Observables</b>	<b>37</b>
3.1 Introduction . . . . .	37
3.2 Single particle properties . . . . .	37
3.2.1 Orientational order . . . . .	39
3.2.2 Second rank order parameter . . . . .	41

3.3	Pair properties . . . . .	44
3.4	Aggregate analysis . . . . .	49
3.4.1	Nanoparticle diffusion . . . . .	49
<b>4</b>	<b>Results – Doping LC with nanoparticles.</b>	
	<b>Effect of shape and size</b>	<b>55</b>
4.1	Pure mesogen simulations . . . . .	55
4.2	Effect of nanoparticle shape . . . . .	61
4.2.1	Sphere–shaped Nanoparticle . . . . .	61
4.2.2	Rod–shaped Nanoparticle . . . . .	72
4.2.3	Disk–shaped Nanoparticle . . . . .	83
4.2.4	Conclusions . . . . .	93
4.3	Effect of NPs size . . . . .	96
<b>5</b>	<b>Results - Doping LC with nanoparticle</b>	
	<b>Effect of nanoparticle–mesogen and nanoparticle–nanoparticle interactions</b>	<b>105</b>
5.1	NP rod with dipoles . . . . .	105
5.1.1	The dipolar interaction . . . . .	106
5.1.2	Pure mesogenic system with dipoles . . . . .	107
5.2	Effect of the strength of interactions (nanoparticle–nanoparticle and nanoparticle–mesogen) . .	111
5.2.1	High solvent affinity . . . . .	111
5.2.2	Low solvent affinity . . . . .	123
5.2.3	Effect of nanoparticle embedded dipoles . . . . .	134
<b>6</b>	<b>Conclusions</b>	<b>147</b>
	<b>Bibliography</b>	<b>149</b>

# Introduction

## Aim of the work

The aim of this thesis is to study the effect of embedded nanoparticles on liquid crystalline systems using Monte Carlo computer simulations. Dispersed liquid crystal composite materials have received significant attention by research community due to their potential impact for technological advancements in the field of displays and sensors. Among these, nanoparticle doped liquid crystals (LCs) systems have shown tremendous interest due to their properties and prospective applications in electronic industry for view in various important phenomena such as electro-optic, dielectric, and memory effects. For example, in LC displays a voltage must be applied to the LCs in order to change their orientation; importantly this voltage must be above a particular threshold for this reorientation. It is shown that, if the mesogen is doped with nanoparticles (NPs), there is a reduction in the threshold voltage, something that would be beneficial in reducing energy usage in these devices. On the other hand, the highly anisotropic environment of LCs may enable the self-assembly of dispersed NPs in two or three dimensional architectures exhibiting high processability and self healing properties; i.e. particular, self-assembled nanoparticles can serve as alignment layers for nematic LCs for the use in sensors; the possible utility of such assemblies has inspired a significant effort to understand and control their formation. In this context we address the lack of fundamental knowledge of the properties and phase behaviour

of these novel composite materials: we focus first on the changes induced by NPs on the orientational LC order and secondly on the key factors determining when and how NPs assemble. This dissertation is organized as follows: in Chapter 1 we will introduce the relevant properties of liquid crystals and describe some of the applications of the doping of LC with various types of nanoparticles. In Chapter 2 we will briefly present the approach used to study these nanocomposite materials, using a Monte Carlo simulation technique. We will describe in some detail the intermolecular multisite Gay–Berne potential, which constitutes our reference model for investigating the organization of these mixture systems. In Chapter 3 we will introduce the single and pair particle properties used to characterize liquid crystalline phases and discuss how they can be determined from computer simulations. We will present a systematic method to identify and characterize nanoparticles aggregates. In Chapter 4 we will present the results of a series of Monte Carlo simulations on systems of rod–like Gay–Berne molecules taking into account the effect of the nanoparticle shape, in particular spherical, rod or disk–like, and dimension. Then, in Chapter 5, we study the effect of the specific interactions between nanoparticles and between nanoparticles and mesogens and of the presence of embedded nanoparticle dipoles. Final remarks of Chapter 6 conclude the dissertation.

# Chapter 1

## Liquid Crystals and Nanoparticles

### 1.1 Liquid Crystals

Liquid crystals (LCs) are states of matter intermediate between the crystalline and isotropic liquid state. Solid crystalline phases are characterized by an high degree of both positional and orientational order: the constituent molecules sit on lattice points, which form a repeat pattern and the direction of the molecular axes are dictated by this arrangement. Instead, in an isotropic liquid phase a random distribution of molecules exists, devoid of both positional and orientational long range orders and molecules are free to translate and rotate. Liquid crystalline materials phases (also called mesophases) show some fluid-like properties (e.g. they can flow and have viscosities similar to those of ordinary liquids) while maintaining a residual degree of orientational order: mesogens exhibit an average preferred alignment and the direction of this preferred orientation is called director of the system. The orientational order gives different optical dielectric magnetic and mechanical properties in different directions, that is the material is anisotropic.

Mesogens can be divided into thermotropic and lyotropic; the first undergo

phase transitions as the temperature changes, while lyotropics are typically amphiphilic molecules that change their organization when dissolved in a suitable solvent upon varying the concentration. The present thesis deals with thermotropic LCs. On the basis of the degree of orientational and positional order thermotropic mesophases can be classified in nematics, which may also include chiral nematic mesophases called cholesterics, and different classes of smectics.

### 1.1.1 Nematic mesophases

Nematic phases exhibit long-range orientational order, while having no order in their translational degrees of freedom. Indeed molecules in that phase can still move freely maintaining the fluidity typical of a liquid but, on average, align each other in the same general direction.

The classical example of room temperature mesogens showing a transition to nematic phase is that of p,p'-cyanobiphenyls, composed of an aromatic biphenyl core substituted by an alkyl chain at one end and by a polar cyano group at the other (see, e.g. the 5CB molecule, Figure 1.1). The presence of the alkyl chain influences the arrangement of the molecules: for  $n < 5$  nCBs do not form LC phases, for 5CB this sequence of phases Crystal  $\xrightleftharpoons{23.0^{\circ}\text{C}}$  Nematic  $\xrightleftharpoons{35.0^{\circ}\text{C}}$  Isotropic is observed. The isotropic - nematic transition is a weakly first order one.

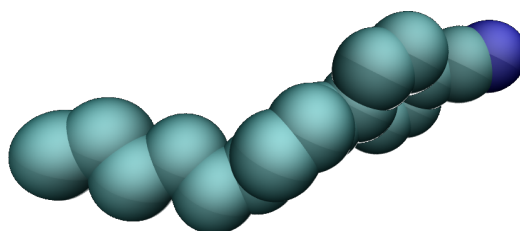


Figure 1.1: 4-pentyl-4'-cyanobiphenyl (5CB) molecule.

In Figure 1.2 is a sketch of a typical monodomain nematic organization is reported as well as a picture showing the typical thread-like texture observed at the microscope between crossed polarizers for a sample where

locally ordered domains are macroscopically disordered. Typically nematics appear to be uniaxial around a preferred orientation called the director, that is their properties are invariant for an arbitrary rotation around the director. As the temperature decreases, the degree of alignment and hence the order typically increases.

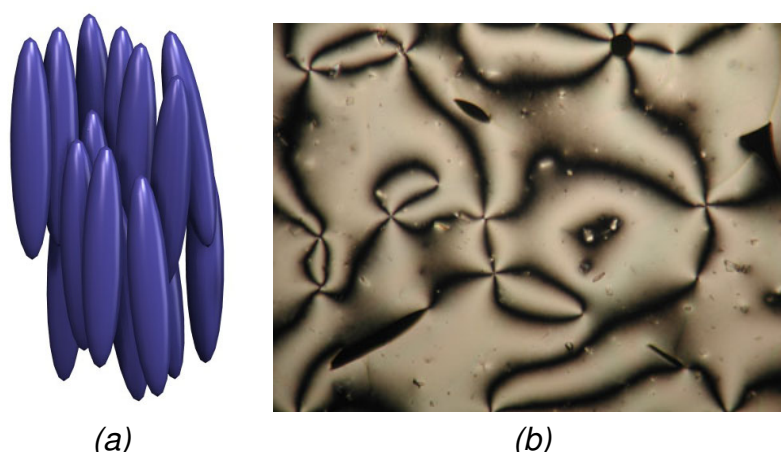


Figure 1.2: Sketch of the molecular organization of a nematic phase monodomain of a thermotropic liquid crystal (a) and typical optical texture of a non aligned nematic between crossed polarizers (b).

The chiral nematic phase is also commonly called cholesteric because it was observed for the first time in derivatives of cholesterol. The molecules in this phase are organized, similarly to those of a nematic, with the molecular axis aligned with respect to the local director, while the director itself assumes a helical structure (Figure 1.4), characterized by the parameter  $p$ , the chiral pitch, which measures the repeat distance between local directors with the same orientation.

### 1.1.2 Smectic mesophases

In smectic phases, molecules are arranged in layers thus exhibiting both long-range orientational order (just as in the nematic phase) and 1D po-

sitional order. The most common phases are called smectic A, in which molecules are on average perpendicular to the layers, smectic B, characterized by an hexagonal clustering of the molecular centres, and smectic C, in which molecules form an angle (tilt angle) with respect to the layer normal (see Figure 1.3). In many cases the layer thickness is equal to the length of the molecule; while for those compounds forming partial or complete bilayers, the layer thickness could approach or be nearly twice the molecular length, due to interpenetration between molecules of the two nearby layers.

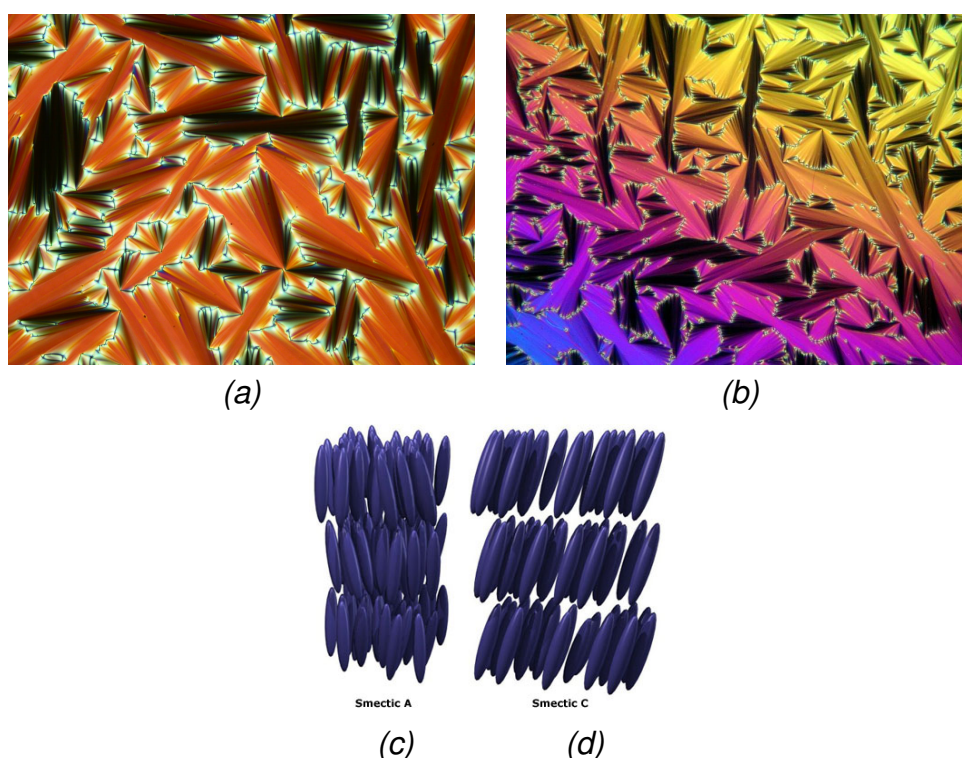


Figure 1.3: Optical textures of thermotropic smectic liquid crystals between crossed polarizers: smectic A (a) and smectic C (b) - Note the typical appearance of fans. Sketch of the molecular organization in smectic A (c) and C phases (d).

Chiral smectic C phases (or  $C^*$  denoting the chirality) also exist, where molecules show a tilted layered structure, like in a Smectic C, but where the director of each layer twists of a finite angle while proceeding along the



direction normal to the layers; as a consequence, a kind of helical structure is formed [1, 2]. Ferroelectric LC phases are obtained from smectic C\* mesogens with a transverse dipole.

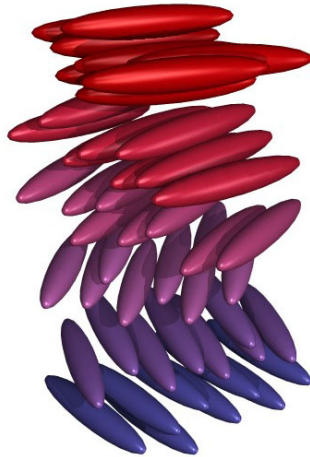


Figure 1.4: Chiral liquid crystal.

### 1.1.3 Blue phases

Blue phases (BPs) are particular liquid crystalline defect phases of chiral mesogens, which thermodynamically exist in a very small range of temperature, between the isotropic liquid and the chiral nematic phase. Blue phases are built from double twist cylinders, which are arranged mutually perpendicular. While two double twist cylinders are placed to form a continuous director field, a third double twist cylinder can only be merged through a creation of a defect; these defects form a cubic lattice with different arrangements. see Figure 1.3 for a schematic representation. Blue phases can be easily identified by polarized optical microscopy thanks to a characteristic platelet texture, see Figure 1.5.

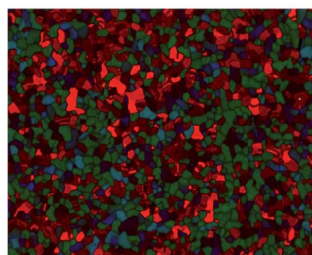
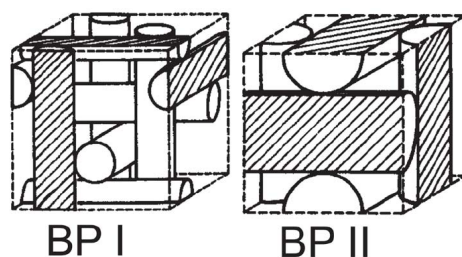


Figure 1.5: Schematic arrangement of the double twist cylinders forming the body-centered and simple cubic defects (typical of Blue Phase I and II) and distinctive texture of a BP seen with an optical microscope under polarized light, adapted from [3]

#### 1.1.4 Discotic columnar phases

Liquid crystal phases are formed from non-spherical mesogens but not necessarily only rodlike ones. For molecules such as HHTT (see Figure 1.6) in which one of the molecular axis is much shorter than the other two, the alternative family of discotic phases arise. Discotic molecules typically have a core composed of aromatic rings with alkyl chains at the periphery. In the discotic nematic phase the director is the average orientation of the short molecular axis. Discotic nematic phases are, however, rather infrequent and most often discotic molecules pack into stacks, giving rise to the so called discotic columnar phases (see Figure 1.7).

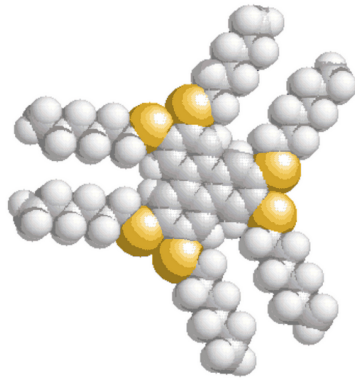


Figure 1.6: Representation of a discotic mesogen.



Figure 1.7: Representation of a discotic columnar LC phase.

## 1.2 Doping LC with nanoparticles

The major applications of nematic LC concern displays (LCD) and other devices where the LC molecular organization and optical properties are changed by the application of external fields. For instance, in a classical twisted nematic (TN) display (Figure 1.8 ), an helical director configuration is established in a thin nematic film by the contrasting aligning effect of the two confining walls of the cell that are treated to impose planar parallel alignment along two perpendicular directions.

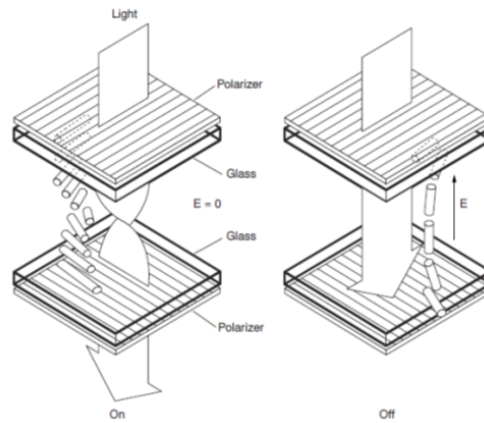


Figure 1.8: Sketch of a twisted nematic LC display pixel in its field off (left) and field on (right) state.

In this type of applications the threshold field needed to switch from one state to the other, the field-on switching time and the time taken to restore the initial helical configuration are important material features to optimize. Doping liquid crystals with nanoparticles provides an important method for tuning material properties and attracts growing attention since the properties of such composites may differ significantly from those of the pure materials. An advantage of tuning properties by the addition of NP is that the optical transparency in the visible, essential for displays, can be maintained. Scattering in fact, strongly depends on the relative size of the particles compared to relevant wavelengths (Figure 1.9) and is relatively negligible for these small sizes. In addition NP suspensions can also be

stable over long times, again an essential requirement for industrial applications.

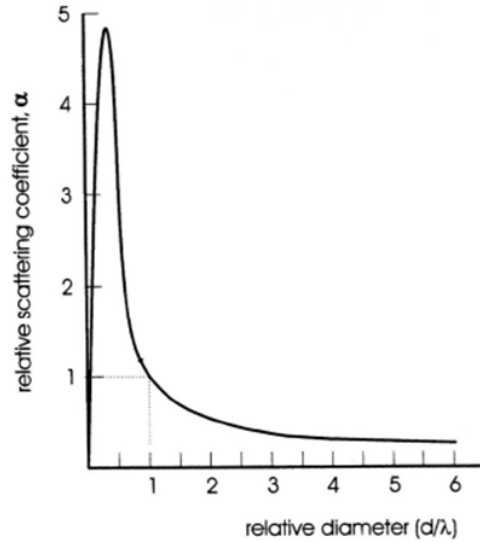


Figure 1.9: Schematic illustration of the effect of particle size, expressed as relative diameter (particle diameter,  $d$  / wavelength of light  $\lambda$ ) on the relative scattering coefficient,  $\alpha$  [4]. The scattering becomes negligible for  $d \ll \lambda$ .

There are many reports showing that doping of a nematic LC with even a small amount of nanoparticles (NPs) results in a decrease of the threshold and switching voltages as well as in reducing the switching times of LC displays [5–9].

Enhancement of LCs properties is dependent on the size, type, concentration and intrinsic characteristic of nanoparticles used for doping, but the overall outlook is far from clear. Here we attempt to give a brief overview of the effects of embedding nanoparticles and relate them to specific nanoparticle features.

### (i) Electro-optic response

Nematics doped with ferroelectric NPs are known to enhance dielectric and optical anisotropy, increase the electro-optic response [10, 11] and

improve the photorefractive properties of composites [12]. Para- and ferromagnetic particles in nematic mesogens are promising candidates for magnetically tunable structures. On the other hand metal and silica nanoparticles in ferroelectric LCs improve the spontaneous polarization and dielectric permittivity and decrease switching times [13–15].

Ha et al. [16] investigated LC displays in which the nematic liquid crystal were doped with metallic Ti nanoparticles ( $\sim 100$  nm) at different concentrations, from 0.1% wt to 2.0% wt. The nematic LC (MJ001929) had a positive refractive index anisotropy  $\Delta n = 0.077$ , an isotropic–nematic transition temperature of  $72^\circ\text{C}$  and a dielectric anisotropy  $\Delta\epsilon = 8.2$ . For a

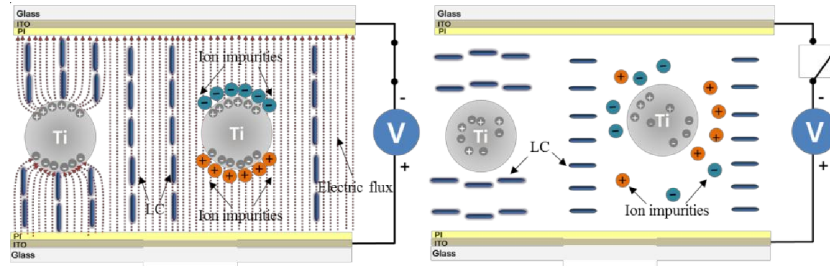


Figure 1.10: Schematic diagram to illustrate the operation of NLCs in an on-state (left) and off-state (right) NLC cell with doping of Ti NPs. Adapted from [16].

metallic conductive particle in an electric field, the tangential component of the electric field at the conductor surface is zero, and the normal component is equal to the surface charge density on the conductor divided by the permittivity of space. The metallic Ti NPs change the electric flux path with a focusing effect of the electric flux and an electric flux density increase around the nanoparticles. As a result, at the same applied voltage level, the local voltage increases around the nanoparticles and as the Ti NP concentration increases, lower threshold voltages and faster response times are obtained. Therefore, this results demonstrates that LCDs performance can be controlled by changing the NPs concentration.

## (ii) Nematic-Isotropic phase transition

NPs may also affect the Nematic-Isotropic (NI) phase transition temperature. While the effect of solute impurities in a nematic LC is typically that of destabilizing the ordered phase, thus lowering the NI transition temperature, the NP effect is far less clear and predictable. Examining published data on this transition temperature and the order of the phase change, it is difficult to find a common pattern among the several experiments carried out in the last years. One of the problems lies in the need to consider a large number of variables, ranging from the nature of the different liquid crystals employed, up to the characteristics of the nanoparticles, where size and polydispersity, concentration and chemical nature seem to be of considerable importance in the study of the interactions with the solvent. From the Table 1.1 we can see that the behavior is very dif-

LC system	NPs	NPs size	NPs conc	$T_{NI}$
8CB [17]	R812 aerosil	7nm	1-10%wt	$= T_{NI}, = T_{NSmA}$
5CB [18]	R812 aerosil	7nm	0.3-3%wt	$= T_{NI}, < P_2$
5CB [19]	R812 aerosil	7nm	1-10%wt	$= T_{NI}, < P_2$
5CB [20]	$Sn_2P_2S_6$ +Oleic acid	20 nm	03% v/v	$< \text{or} > T_{NI}$
ZLI-4801 [13]	$Sn_2P_2S_6$ +Oleic acid	10 nm	0.3% v/v	$< T_{NI}$
LSCE [21]	$PbTiO_3$ (F)	40-800 nm	1-5% w/w	$=$

Table 1.1: Summary of the effects of different classes of NPs on the NI transition in relation to type, size and concentration. In particular, in the last column, the nematic–isotropic transition temperature is indicated with  $T_{NI}$ , while  $T_{NSmA}$  represent the nematic–smectic A transition temperature. Also the orientational order parameter  $P_2$  of the nematic liquid crystalline phase is reported.

ferent, depending on the kind of nanoparticle. Same NP types seem to have a consistent behaviour, e.g. metal nanoparticles such as gold and silver have been shown to have a tendency to lower the transition temperature [13, 14, 22–24]. The addition of very small silica nanoparticles (aerosils) seems instead to have very little effect on the transition temperature, despite the formation of aggregates, which could easily disturb

the local order [17–19]. A non consistent behaviour is shown by other members of the same category, such as  $Sn_2P_2S_6$  which shows contrasting effects depending on the concentration [13, 20].

The effect of the size in the case of a ferroelectric nanoparticle seems to be irrelevant, since  $PbTiO_3$  nanoparticles of different, even if all relatively large, sizes (from 40 to 800 nm) do not seem to vary the clearing transition, even when concentration is increased [21].

The N–I transition temperature increases in nematics doped with strongly anisotropic NPs including nanotubes [25], magnetic nanorods [26] and various ferroelectric particles [10, 11]. One example is the effect of  $BaTiO_3$  nanoparticles: of considerable interest is the work of *Reznikov et al.* [14], which reported an increase in the N–I transition temperature of  $9^\circ C$ . In this case, despite the variation of the solvent, the size of the nanoparticles appears to be the most relevant factor influencing the increase and decrease of  $T_{NI}$  (see Table 1.2). It is important to take into account NPs aggregation which is likely to happen when adding nanoparticles to LCs, especially ferroelectric ones. In all the experiments considered in Table 1.2 the surfactant oleic acid was added in order to increase the interaction of NPs with the solvent and decrease their aggregation tendency; it is therefore of great importance to consider the *affinity* between nanoparticle and mesogen.

LC system	NPs	NPs size	NPs conc	$T_{NI}$
MLC-6609 [14]	$BaTiO_3$ +OA <sup>1</sup> (F)	50-100 nm	0.2%	$> (9^\circ C)$
TL205 [27]	$BaTiO_3$ +OA	9 nm	0.5% w/w	$<$
5CB [28]	$BaTiO_3$ +OA	150 nm	4% v/v	$> (> P_2)$
TL205 MLC6815 [29]	$BaTiO_3$ +OA	10-28 nm	1% w/w	$<$
8CB [30]	$BaTiO_3$ +OA	1 2nm	0.2-0.4%w/w	$< (= T_{NSmA})$
8OCB 8CB 1:3 [31]	$BaTiO_3$ +OA	15 nm	5-10mg/g	$< (< T_{NSmA})$
EN18 [32]	$BaTiO_3$ +OA	15 nm	5mg/g	$< (< T_{NSmA})$

Table 1.2: Summary of the effects of ferroelectric NPs on the NI transition in relation to type, size and concentration.

---

<sup>1</sup>Oleic acid



In general, when NPs and LC sizes are similar, the N–I transition temperature decreases with NPs increasing concentration. This kind of phase separation is very important for the application of LC nanocomposites, and it has been observed in few anisotropic soft matter systems.

### (iii) Metamaterials

LC-NP composites are also investigated as the building blocks of novel metamaterials. Sub-wavelength metallic or semiconductor particles can be used to tailoring the optical response, achieving very high or very low and negative values of refractive index, permittivity and/or permeability [33]. Upon immersing a metamaterial into a nematic LC one can switch the LC alignment by changing the temperature or external voltages and modify the overall optical properties of the composite. The smallest size of NPs may be close to molecular dimensions, but the properties of the particles differ significantly from those of surrounding mesogenic molecules and therefore a phase separation should be a common phenomenon. One example is given by the self-assembly of liquid crystalline gold metamaterials. Combining gold nanoparticles with liquid crystals, could provide materials that can be induced to assemble in a controlled way and have a particular and unique optical properties [34]. Coating the Au nanoparticles

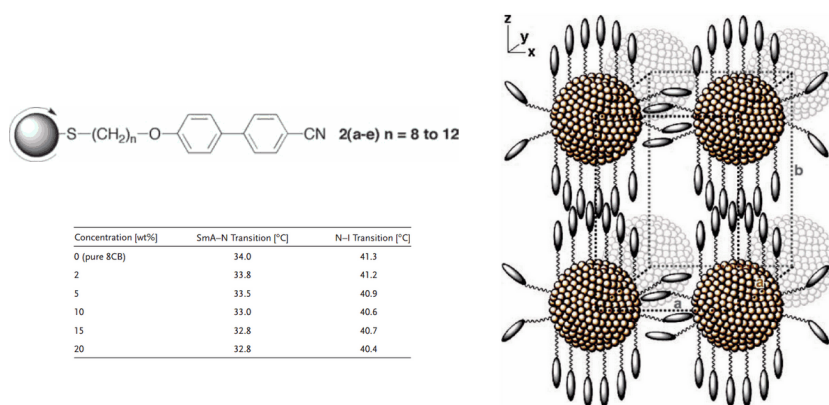


Figure 1.11: Target liquid crystal coated gold nanoparticles; transition temperatures of mixtures of 8CB and NPs determined by DSC (on table); a simplified illustration of the arrangement of NPs in a condensed mixed phase. Adapted from [34].

with specific ligands can allow NPs to be mixed into other media without segregation, beyond affect the organization properties.

#### (iv) Blue Phases

Phase separation in LCs doped with NPs is not always a negative effect which should be avoided. For examples, the introduction of spherical nanoparticles in LC blue phases seems to have a stabilizing effect. [35] In fact NPs mainly concentrate in the vicinity of defects, i.e. of regions with the highest (most unfavourable) free energy which results in a decrease of their energy, opening the way to building new molecular and NP 3D organizations by exploiting them. The stabilization effect depends on the NPs size.

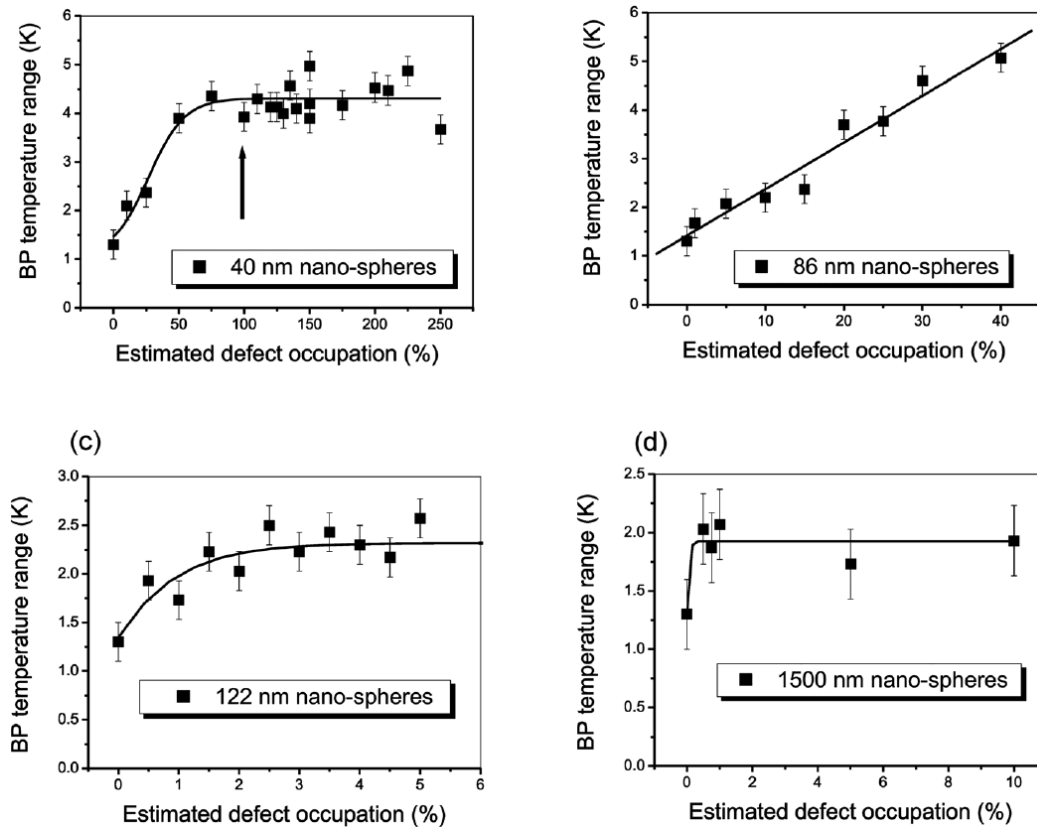


Figure 1.12: (a) For small nanoparticles a large filling ratio can be achieved and stabilization effects level off at 100% defect occupation. (b) and (c) For increasing NPs sizes, dispersion becomes increasingly difficult, so the efficiency in stabilization decreases. (d) For particles much larger than the BP unit cell, the stabilization is not effective at all. Adapted from [3].

### 1.3 Theoretical background

To make progresses with these materials it is essential to develop some theory for the interaction between liquid crystals and ferroelectric nanoparticles. In the theory proposed by *Reshetnyak et al.* the key issue is how an ensemble of NPs with aligned dipole moments can polarize the LC molecules [14, 36, 37]. This electrostatic effect enhances the I-N transition temperature and reduces the Frederiks transition voltage. Molecular dynamics simulations of ferroelectric NPs doping a nematic liquid crystal [38] which assume aligned NPs, show an enhancement of LC order. *Lopatina and Selinger* [15, 39], on the other hand, proposed a different type of explanation based on statistical mechanics for ferroelectric nanoparticles behaviour. They suppose that both LC and NPs have distributions of orientations characterized by two different order parameters.

# Chapter 2

## Computer simulations

### 2.1 Introduction

Computer simulation provide an important way of linking microscopic models and experimental observables. Theoretical, statistical mechanics studies, while aiming at retaining the essential physics, tend to be based on very and sometimes oversimplified models; thus it is often difficult to compare predictions with experimental results. Computer simulation methods, represent, as we shall see, brute force numerical approaches to the problem of calculating observable properties for bulk or nano size systems from molecular models that, although still approximate, can be much more detailed and representative of real systems with respect to statistical theories. The results of computer simulations can then be used to test theories and to check the validity of models in comparison to experimental results, but more importantly they also provide a connection between specific molecular features (shapes, charges, dipoles, etc..) and macroscopic material properties. Computer simulations allow also to determine properties in situations out of the reach of experiment, such as extreme pressure and temperature conditions. However it should be remembered that a successful prediction of properties is dependent on a good representation of the interaction between molecules. For any simulation study, the basic

methodology can be divided into three parts:

- constructing a model that describes the system under investigation, typically starting with a description of a single molecule and of pair-wise interactions;
- implementing the model in a simulation procedure, e.g. Monte Carlo or Molecular Dynamics;
- using output to monitor the progress of the simulation and to calculate macroscopic properties.

This chapter provides first a description of the two principal methods used in simulations of LC at the molecular scale, namely Monte Carlo and Molecular Dynamics methods [40–43]. Then, since any molecular simulation has at its hearth an interaction potential which represents the microscopic energetics defining the molecular system, the potentials developed to model both LC and NPs are discussed.

## 2.2 Monte Carlo simulations

The Monte Carlo method used in statistical mechanics was proposed by Metropolis et al. [44] to evaluate equilibrium statistical averages. Typical examples of thermodynamic properties calculated according to this method are the energy  $\langle U \rangle$ , pressure  $\langle p \rangle$ , volume  $\langle V \rangle$ , density  $\langle \rho \rangle$  and so on (where  $\langle \rangle$  symbolizes a statistical average).

Considering a system of  $N$  rigid particles interacting with each other through a pair potential  $U_{ij} = U(X_i, X_j)$ , for a fixed value of each of the positional-orientational coordinates  $X_i$  of each particle  $i$ , we have that the total energy of the system will be:

$$U(\{X\}) = \frac{1}{2} \sum_{i \neq j} U(X_i, X_j) \quad (2.1)$$

Note that  $\{X\} = X_1, X_2, \dots, X_N$  represents the set of positional and orientational coordinates, also called configuration. For this system, in canonical conditions, constant number of particles  $N$ , volume  $V$  and temperature  $T$ , all static properties can be expressed as the Boltzmann average

$$\langle A \rangle = \frac{\int \{dX\} A(\{X\}) e^{-U(\{X\})/k_B T}}{\int \{dX\} e^{-U(\{X\})/k_B T}} \quad (2.2)$$

where  $k_B$  is the Boltzmann constant. In a real system we can imagine to consider a number  $M$  of configurations sampled from the equilibrium distribution (“importance sampling”) and to calculate  $A^{(j)}$  for each  $j$  configuration. In this case the integral can be approximated, for  $M$  sufficiently large, with the simple arithmetic mean

$$\langle A \rangle = \frac{1}{M} \sum_{j=1}^M A^{(j)} \quad (2.3)$$

This simplification is possible since, once the equilibrium is reached, a given system has a probability of having a certain configuration  $\{X\}$  associated with energy  $U(\{X\})$  that is proportional to the Boltzmann factor  $\exp(-U(\{X\})/k_B T)$ .

The Monte Carlo method in this context represents a technique for generating these equilibrium configurations: the order in which the configurations are generated is not important since we are interested in static quantities. In order to have an efficient method the frequency with which the configurations are generated must be proportional to the Boltzmann factor and the sequence must be random and independent from the initial configuration.

### **Markovian processes and Metropolis algorithm**

The mathematical justification of the MC method lies in the theory of Markov processes [45], ie. stochastic processes, where a system evolves through

a sequence of states with memory limited to the previous state. The probability that a system evolving in accord to a Markov process is in a state  $k$ , at time  $t$ , depends only on the state at time  $(t - 1)$ . For a system at equilibrium we require that each state  $j$  with energy  $U^{(j)}$  belongs to the Markov chain, then the relative frequency  $w_j$  is given by its Boltzmann probability:

$$w_j = e^{-[U^{(j)}/k_B T]} / Z_N \quad (2.4)$$

where the configurational partition function  $Z_N$  is a normalization constant. The Metropolis algorithm provides a simple way of producing a Markov chain; in its most basic form, it considers a system of  $N$  interacting particles at temperature  $T$  in a volume  $V$ . Configuration space is sampled by choosing one particle  $i$  at random and assigning it a new random position–orientation. The move is accepted if it goes downhill in energy  $\delta U = U^{new} - U^{old} \leq 0$ . Instead, if the move is uphill in energy, i.e.  $\delta U > 0$ , then it is accepted with a probability  $e^{-\delta U/k_B T}$ . This is performed by generating a random number  $\xi \in [0; 1)$ : the move is accepted if  $\xi \leq e^{-\delta U/k_B T}$  and rejected otherwise. This procedure (called MC step) will be repeated for a suitable large number of steps in order to achieve a good convergence to the equilibrium values. The method can be applied to rigid molecules of arbitrary shape, but even to non rigid molecules where new states are created by changing the positions, orientations and conformations of the molecules [40]. A schematic representation of Monte Carlo algorithm is shown Figure 2.1.

The Monte Carlo method has been and is applied with success to the study of condensed phases in various statistical ensembles, including the canonical ensemble (NVT), and, as a generalization, the isobaric–isothermal (NPT). In these cases the number  $N$  of particles is kept constant and typically has values ranging between a few hundreds and a few million, still very small compared to the Avogadro number. Nevertheless, using periodic boundary conditions it is possible to reduce the effect of finite size and thus approximate the thermodynamic limit ( $N \rightarrow \infty$ ;  $V \rightarrow \infty$ ,



1. Choose a particle  $i$  at random
2. Assign a new random position and orientation
3. IF  $(\delta U \leq 0)$  OR  $(\xi \leq e^{-\delta U/k_B T})$   
    Accept move  
    ELSE  
        Reject move
4. Store instantaneous observable
5. Return to step 1 until  $n_{\text{step}}$  performed
6. Compute observable average

Figure 2.1: The Monte Carlo algorithm in the canonical ensemble.

$\rho = N/V = \text{const.}$ ).

If the initial configuration is not an equilibrium state at the chosen temperature, the simulation is let to evolve until the equilibrium is reached.

The number of cycles (a cycle is a set of  $N$  MC moves) necessary to reach the equilibrium is not predictable a priori, even if it depends on the effectiveness of the configurational space sampling and on the probability with which the generated configurations are accepted. At each step the size of the move is governed by the maximum displacement  $\delta X_{max}$ , roughly an adjustable parameter whose value is usually chosen so that 50% of the trial moves are accepted. If  $\delta X_{max}$  is too small, then many moves will be accepted but the states generated will be very similar to the previous ones and the system will explore phase space very slowly; if  $\delta X_{max}$  is too large, then very few moves will be accepted.

### Extention to the isothermal–isobaric ensemble

The Metropolis solution can be extended to other ensembles; Wood [46] proposed a method to extend it to isothermal–isobaric one. In that case the equilibrium probability for the system to be in state with enthalpy  $H^{(j)}$  is:

$$w_j = e^{-\frac{H^{(j)}}{k_B T}} / Z_N \quad (2.5)$$

where  $H = U + PV$ ,  $P$  represents the pressure and  $V$  the volume. The difference in the algorithm with respect to the one used for the canonical ensemble, lies in the change of volume that is performed periodically in order to keep the pressure constant. Trial volume changes ( $V_{nt} - V_t$ ) are evaluated by testing the variation in enthalpy  $\delta H$  given by:

$$\delta H = \delta U + P(V_{nt} - V_t) - Nk_B T \ln \left( \frac{V_{nt}}{V_n} \right) \quad (2.6)$$

so that a given volume change move is accepted if  $\delta H \leq 0$  or  $\xi \in [0; 1] \leq e^{-\delta H/k_B T}$  and rejected otherwise.

## 2.3 Molecular Dynamics

The Molecular Dynamics (MD) simulation method [43], first introduced by Alder and Wainwright in 1959 [47], studies the macroscopic behaviour of systems by following the evolution of all the constituent interacting particles over a finite, usually short, time. The engine of a MD code is its time integration algorithm, required to integrate the Newton equation of motion for the interacting particles and follow their trajectories. Indeed in MD simulations the collective properties are determined starting from the trajectory of all particles. The ensemble average of a specific property  $A$  of an ergodic system can be obtained from a time average of its instantaneous values

over a total time  $t_T$ :

$$A = \langle A(\{\mathbf{X}(t)\}) \rangle_{time} = \frac{1}{t_T} \int_0^{t_T} A(\{\mathbf{X}(t)\}) dt \quad (2.7)$$

where  $\mathbf{X}(t)$  describes the set of positions and orientation of the  $N$  particles system at time  $t$ . The integration algorithms are based on finite difference

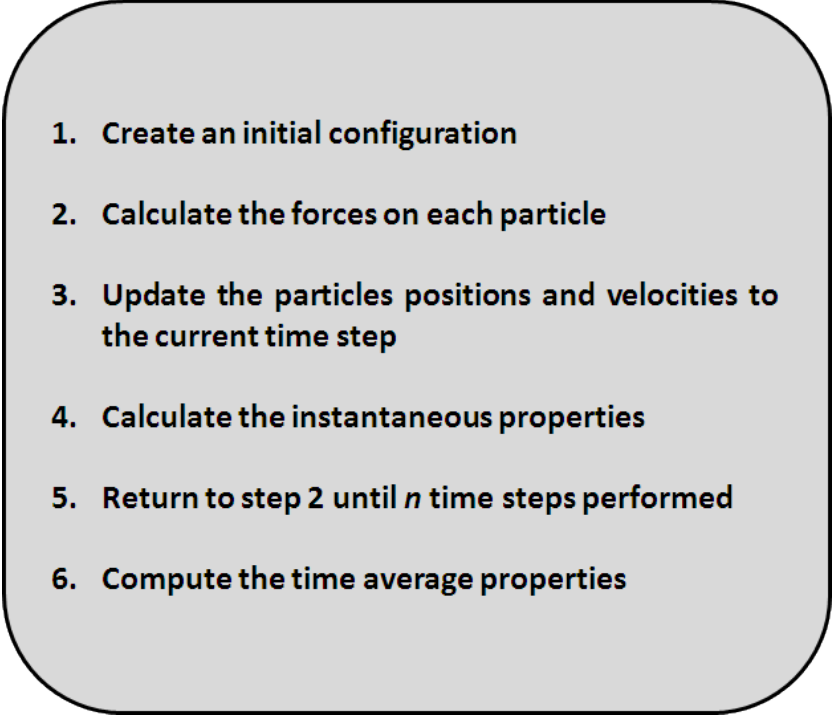
- 
- 1. Create an initial configuration**
  - 2. Calculate the forces on each particle**
  - 3. Update the particles positions and velocities to the current time step**
  - 4. Calculate the instantaneous properties**
  - 5. Return to step 2 until  $n$  time steps performed**
  - 6. Compute the time average properties**

Figure 2.2: The Molecular Dynamics algorithm.

methods where time is discretized on a finite grid. The most popular integration methods are the Verlet algorithm [48], the *leap-frog* algorithm [49] and the velocity-Verlet algorithm [50]. The basic microcanonical MD technique has been readily extended to perform simulations at constant temperature and pressure; considerable number of thermostats and barostats are currently available [41]. The general algorithm of the Molecular Dynamics method is sketched on Figure 2.2.

## 2.4 Microscopic Models

In constructing a model it is important to consider the level of detail that is to be used since the time and length scales of any simulation should reflect the scale of the phenomenology that is under investigation. For example quantum molecular dynamics approaches, using schemes like the Car–Parrinello [51] technique, are able to investigate a small number of atoms over a short amount of time: a typical case for a quantum molecular dynamics study could be to investigate  $\approx 64$  water molecules for  $\approx 100$  ps. They are particularly important in situations where bonds between atoms can form and break, e.g. when chemical reactions take place. In our case we are interested in studying instead systems with well defined composition and investigate molecular organizations and their changes and suitably parametrized classical mechanics simulations of molecular systems suffice. In particular, atomistic studies, in which each atom in a molecule is represented by a specific site, may at present time be employed to explore systems of tens of thousands of atoms over nanosecond timescales. Atomistic simulations are essential when a specific chemical structure is assumed and predictions on the resulting observable properties, e.g. phase transitions, order parameters, etc. are sought. To look at larger systems over longer times, coarse grained approaches have been developed [52–55]. Here groups of atoms are represented by specifically tailored potentials. Using coarse grained models, it is possible to examine systems equivalent to hundreds of thousands of atoms over hundreds of nanoseconds. While the name coarse grained suggests a systematic procedure to generate the potential starting from a more detailed atomistic description, the same name is often used to indicate molecular resolution models where an entire molecule is replaced by a simple anisotropic particle with approximately the appropriate size, shape and possibly specific interaction features.

Over the last decades, liquid crystalline materials have been modelled us-

ing a range of scales and levels of detail. The characteristics and level of detail of a model must be taken into account when conclusions are drawn from the results of a computational study. For example, a mesogenic molecule that is represented by a simple single site has a fixed shape and dimensions and therefore describes a rigid molecule. Most real mesogens are not completely rigid, but rather have both a flexible and a rigid part. This difference between the real system and the model can have a profound effect on the formation of ordered phases because the packing of rigid particles is less efficient. The effect of this discrepancy is seen in the difference between the change in density at the phase transition in the real and model systems. In essence any computational study must balance the constraints that the physics of the system under investigation creates with the availability of computer resources.

For this research, the main considerations when deciding upon the choice of a model is the nanocomposite nature of the systems which requires large system sizes and requires a coarse-grained approach. Moreover, for these complex systems, understanding general behaviour and trends rather than reproducing specific chemical systems is already a very ambitious target.

Regarding liquid crystalline systems, a large variety of models is available [42, 53, 54, 56] . The most common potentials in LC simulations are often assuming rigidity and are divided in hard and soft potentials.

The form of the first type is very simple and purely repulsive: the only interaction present is that to prevent inter-penetration of particles and the effect of the particles nature on the phase behaviour depends only on shape and density. The simplest model is the hard sphere, and strings of spherical repulsive beads have been used to model LC, although LC models are often represented as rods or disks, respectively for calamitic and discotic mesogens (see Figure 2.3).

Soft potentials have the peculiarity of smoothly changing from repulsive to attractive with increasing the separation distance between particles. A

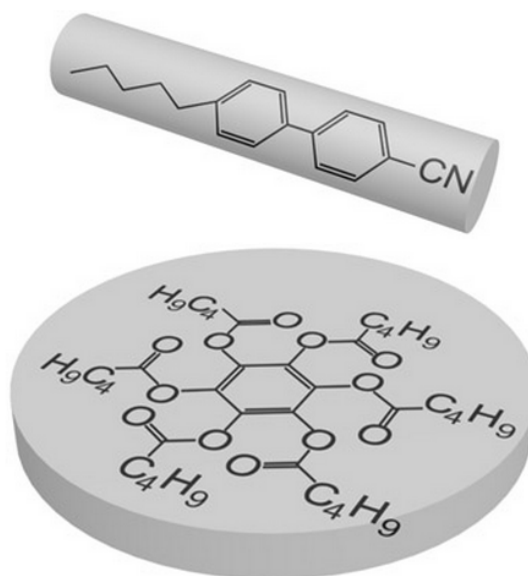


Figure 2.3: Molecular structure of 5CB and benzene-hexan-n-alkanoate derivatives liquid crystals (adapted from [57]).

smooth potential which is soft and has long-range attractive interactions and short-range repulsive ones, represents a good choice to fit the van der Waals dispersion forces existing between molecules. Examples of such kind of potentials are Lennard-Jones for isotropic particles and Gay-Berne for anisotropic ones.

### 2.4.1 Gay-Berne coarse grained model

The Gay-Berne (GB) potential is the most successful and popular interaction model for soft anisotropic particles, described as rigid bodies of ellipsoidal shape, particularly studied in the field of thermotropic mesogens simulations. Originally developed [58] to fit a linear arrangement of four Lennard-Jones (LJ) [59] sites with a single ellipsoidal particle, the model can be considered as a generalization of the LJ 12-6 potential, where shape and interaction anisotropies have been introduced. The GB interaction potential between particles  $i$  and  $j$ , assumed to be uniaxial, therefore depends on their orientations, defined by the unit vectors  $\hat{u}_i$ ,  $\hat{u}_j$ , and by

their vector distance,  $\mathbf{r}_{ij}$ :

$$U(\hat{\mathbf{u}}_i, \hat{\mathbf{u}}_j, \hat{\mathbf{r}}_{ij}) = 4\epsilon_0 \epsilon(\hat{\mathbf{u}}_i, \hat{\mathbf{u}}_j, \hat{\mathbf{r}}_{ij}) \times \left[ \left( \frac{\sigma_0}{r_{ij} - \sigma(\hat{\mathbf{u}}_i, \hat{\mathbf{u}}_j, \hat{\mathbf{r}}_{ij}) + \sigma_0} \right)^{12} - \left( \frac{\sigma_0}{r_{ij} - \sigma(\hat{\mathbf{u}}_i, \hat{\mathbf{u}}_j, \hat{\mathbf{r}}_{ij}) + \sigma_0} \right)^6 \right] \quad (2.8)$$

where  $\sigma_0$  and  $\epsilon_0$  define the scales of length and energy, while  $\sigma(\hat{\mathbf{u}}_i, \hat{\mathbf{u}}_j, \hat{\mathbf{r}}_{ij})$  and  $\epsilon(\hat{\mathbf{u}}_i, \hat{\mathbf{u}}_j, \hat{\mathbf{r}}_{ij})$  are the anisotropic contact distance and potential well depth, respectively. The contact distance reads:

$$\sigma(\hat{\mathbf{u}}_i, \hat{\mathbf{u}}_j, \hat{\mathbf{r}}) = \sigma_0 \left\{ 1 - \frac{\chi}{2} \left[ \frac{(\hat{\mathbf{u}}_i \cdot \hat{\mathbf{r}} + \hat{\mathbf{u}}_j \cdot \hat{\mathbf{r}})^2}{1 + \chi(\hat{\mathbf{u}}_i \cdot \hat{\mathbf{u}}_j)} + \frac{(\hat{\mathbf{u}}_i \cdot \hat{\mathbf{r}} - \hat{\mathbf{u}}_j \cdot \hat{\mathbf{r}})^2}{1 - \chi(\hat{\mathbf{u}}_i \cdot \hat{\mathbf{u}}_j)} \right] \right\}^{-1/2} \quad (2.9)$$

where

$$\chi = \frac{k^2 - 1}{k^2 + 1} \quad (2.10)$$

is the shape anisotropy parameter, defined by the length-to-breadth ratio,  $k$ . The well depth is determined by two functions:

$$\epsilon(\hat{\mathbf{u}}_i, \hat{\mathbf{u}}_j, \hat{\mathbf{r}}) = [\epsilon_1(\hat{\mathbf{u}}_i, \hat{\mathbf{u}}_j, \hat{\mathbf{r}})]^\mu [\epsilon_2(\hat{\mathbf{u}}_i, \hat{\mathbf{u}}_j)]^\nu \quad (2.11)$$

where

$$\epsilon_1(\hat{\mathbf{u}}_i, \hat{\mathbf{u}}_j, \hat{\mathbf{r}}) = 1 - \frac{\chi'}{2} \left[ \frac{(\hat{\mathbf{u}}_i \cdot \hat{\mathbf{r}} + \hat{\mathbf{u}}_j \cdot \hat{\mathbf{r}})^2}{1 + \chi'(\hat{\mathbf{u}}_i \cdot \hat{\mathbf{u}}_j)} + \frac{(\hat{\mathbf{u}}_i \cdot \hat{\mathbf{r}} - \hat{\mathbf{u}}_j \cdot \hat{\mathbf{r}})^2}{1 - \chi'(\hat{\mathbf{u}}_i \cdot \hat{\mathbf{u}}_j)} \right] \quad (2.12)$$

$$\epsilon_2(\hat{\mathbf{u}}_i, \hat{\mathbf{u}}_j) = [1 - \chi^2(\hat{\mathbf{u}}_i, \hat{\mathbf{u}}_j)^2]^{-1/2}. \quad (2.13)$$

while the parameter

$$\chi' = \frac{(k')^{1/\mu} - 1}{(k')^{1/\mu} + 1} \quad (2.14)$$

is defined in terms of the well depth anisotropy  $k'$ , i.e. the ratio between well depths for the side-by-side and end-to-end interactions, respectively. The exact form of the GB potential is determined by the four parameters  $\mu, \nu, k, k'$ , with the exponents  $\mu, \nu$  tuning the orientational dependence of

the energy. The original formulation, with parameters  $k = 3$ ,  $k' = 5$ ,  $\mu = 2$ ,  $\nu = 1$ , gives rise to stable nematic and smectic LC phases.

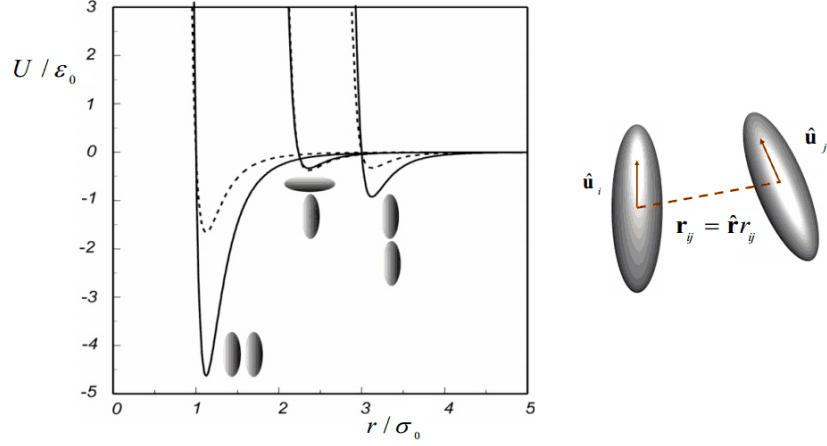


Figure 2.4: The GB potential as a function of dimensionless intermolecular distance for  $k = 3$ ,  $k' = 5$  in side-by-side, T-shaped, and end-to-end configurations (left panel). Energy parameters are  $\mu = 2$ ,  $\nu = 1$  (dashed line) and  $\mu = 1$ ,  $\nu = 3$  (continuous line). Adapted and reproduced from [53]. The sketch on the right defines  $\hat{\mathbf{u}}_i$ ,  $\hat{\mathbf{u}}_j$  and  $\mathbf{r}_{ij}$  for a pair of GB particles.

## 2.4.2 Models for LC–NP systems

### Generic LC

We have considered a system of uniaxial ellipsoidal particles characterized by positional and orientational degrees of freedom and interacting with a pair potential  $U_{ij}^* = U_{ij}/\varepsilon_S$  that is sum of a Gay–Berne dispersive potential and, in presence of dipoles, an electrostatic contribution  $U_{ij}^* = U_{GB}^* + U_d^*$ . In particular, for the GB potential, we have employed shape anisotropy  $k = \sigma_e/\sigma_s = 3$ , interaction anisotropy  $k' = \varepsilon_S/\varepsilon_e = 5$ , cutoff  $R_c^{(GB)*} = R_c^{(GB)}/\sigma_S = 6.0$  and the parametrization indicated in Table 2.5, with GB exponential coefficients  $\mu = 2$  and  $\nu = 1$  as in the original formulation [58].

The graph above is relative to the pair potential curves obtained for three typical configurations of a pair of molecules. We can notice that among



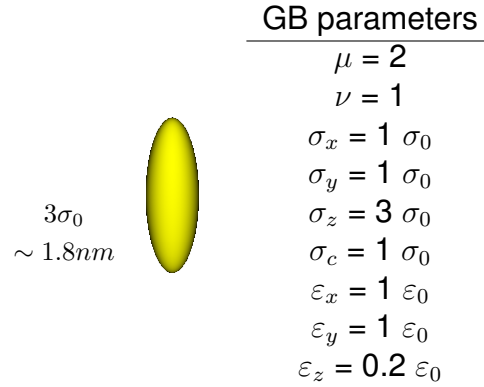


Figure 2.5

the three, the curve characterized by the deepest potential well is the one referring to parallel molecules with  $\hat{\mathbf{r}}_{ij} \perp \hat{\mathbf{u}}_i, \hat{\mathbf{u}}_j$  (thus the side-side configuration corresponds to the strongest interaction).

### Nanoparticle model

While a variety of models have been developed for liquid crystals, as shown in the above paragraphs, the studies carried out, at the theoretical level, on nanoparticles are not so widespread. Nanoparticles used to study NP-LC mixtures are generically modelled as a spherical or rod-like particles of similar size with respect to the mesogen. Also in this case, as for simple fluids, hard square well or Lennard–Jones (see Figure 2.7) are used.

However, it is of great importance that the potential could be tunable as much as possible, in order to study a number of interesting effects at the nanoscale level, such as that of a particular type of anchoring (see Figure 2.8), how the molecules prefer to orient at the NP surface, or how NPs self-assemble between them.

In our case we have chosen to model a nanoparticle not as a single site, but as a collection of spherical Lennard-Jones sites rigidly connected to each other to form different NPs shapes. This type of modeling has been chosen as it makes the treatment of intermolecular interactions easier (e.g.

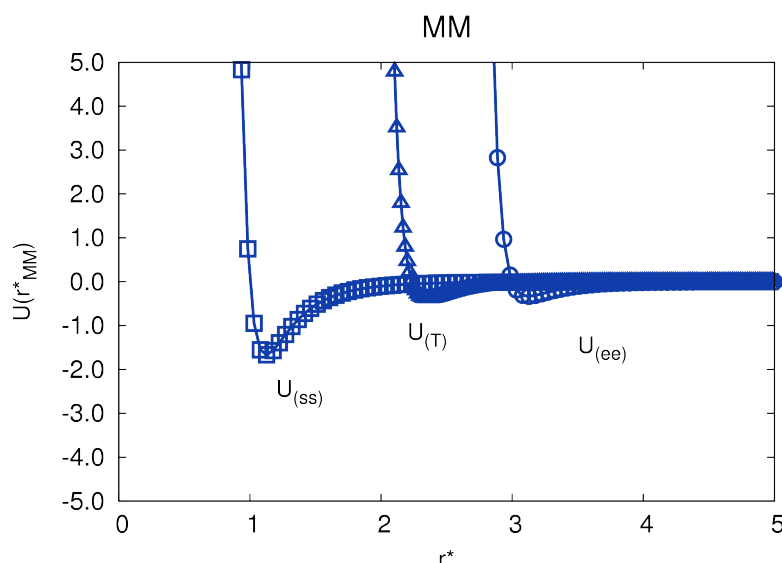


Figure 2.6: The graph shows the potential energy profiles obtained for three directions of approach (side-side, end-end and T) of a second molecule with respect to the first.

it allows substantially lowering the cutoff values for intermolecular interactions) and at same time it allows treating more realistic nanoparticles shape. In practice using this approach has made possible the study of the influence of different shape and size nanoparticles on the liquid crystalline phase. The shapes taken into account here are a sphere, an elongated rod and disks of two different sizes. For the case of rodlike nanoparticles we have also compared the effects of apolar NPs with that of polar NPs, where a dipole moment placed in the center of the rod was added.

Another interesting feature of our cluster-like modeling lies in the possibility of varying the intensity of the interaction between nanoparticles by adjusting the value of the energetic parameter  $\varepsilon_S$  characteristic of each LJ sphere. This has allowed us to investigate one important aspect present in real NP suspensions, i.e. the aggregation of NPs and the effect of the aggregates on liquid crystalline phases as a function of the degree of NPs aggregation.

Nanoparticles parameterization in terms of energy leads to a planar an-

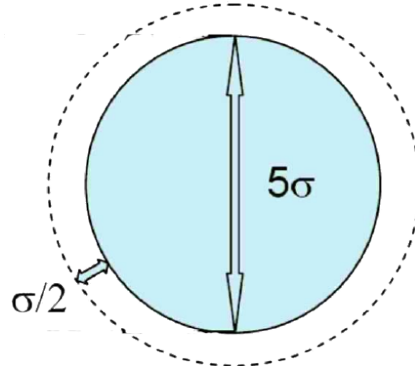


Figure 2.7: Schematic representation of a spherical nanoparticle adapted from [60].

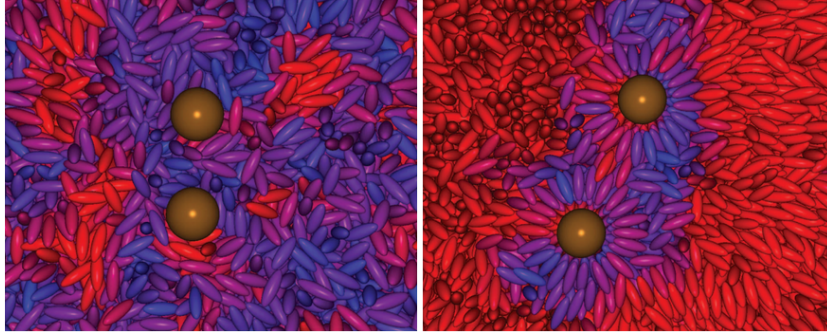


Figure 2.8: Representative configurations for LC-NP mixtures with respectively planar and homeotropic anchoring, adapted from [61].

choring of the liquid crystal on the nanoparticle surface. It is known that LC molecules adopt one orientation over another depending on the functionalization of the particle surface, on the bulk spatial properties of LCs and on the relative strength of the interactions between mesogen and nanoparticles (MN). It is therefore interesting to be able to modify the heterogeneous interactions, to simulate different possible situations with regard to the aggregation of nanoparticles from one part, and the variation of the liquid crystalline phase from the other. With this aim, an additional parameter  $e_{NM}$  is thus introduced in the heterogeneous GB potential to take into ac-

count the solvation affinity of the NP towards the mesogen:

$$U_{AB}(\omega_1, \omega_2, \hat{\mathbf{r}}_{12}) = 4\varepsilon_0 e_{NM} \varepsilon_{AB}^\nu(\omega_1, \omega_2) \varepsilon_{AB}^{\prime\mu}(\omega_1, \omega_2, \hat{\mathbf{r}}_{12}) \times \left[ \left( \frac{\sigma_c}{r_{12} - \sigma_{AB}(\omega_1, \omega_2, \hat{\mathbf{r}}_{12}) + \sigma_c} \right)^{12} - \left( \frac{\sigma_c}{r_{12} - \sigma_{AB}(\omega_1, \omega_2, \hat{\mathbf{r}}_{12}) + \sigma_c} \right)^6 \right] \quad (2.15)$$

The parameter  $e_{MN}$  allows to rescale the amplitude of the single site-site pair energy, without altering the distance dependence in our investigation of nematic systems doped with polar rod NPs and disk shaped NPs, making it easier to separate solvent affinity and electrostatic effects.

# Chapter 3

## Observables

### 3.1 Introduction

In this Chapter we introduce the most relevant observables considered for the analysis of the simulation results together with the needed computational details and in particular we discuss the description of orientational order and of relevant pair particle properties. Simulation studies are able to provide much more detailed information on the molecular level, if compared with their experimental counterparts, as each simulation determines positions and orientations of every particle for a large number of equilibrium configurations. These "snapshots" that we shall also represent with the help of computer graphics are themselves very useful to provide a qualitative understanding of phenomena like phase organizations and aggregations, that can then be quantified by suitable observables.

### 3.2 Single particle properties

As already mentioned, MC computer simulations generate equilibrium configurations. A complete knowledge of the static equilibrium properties of the system of  $N$  rigid particles studied can be obtained from a sufficiently large set of  $M$  configurations (i.e. set of positions  $\mathbf{r}_i = (x_i, y_i, z_i)$  and orien-

tations  $\omega_i$  of all the particles). Indeed, calculating the value of an arbitrary property  $A(\mathbf{r}_i, \omega_i, \dots, \mathbf{r}_N, \omega_N)$ , depending on molecular positions and orientations, in each of these equilibrium configurations ( $\mathcal{J}$ ) we can obtain the average value of  $A$  as

$$\langle A \rangle = \frac{1}{M} \sum_{\mathcal{J}}^M A^{\mathcal{J}}(\mathbf{r}_i, \omega_i, \dots, \mathbf{r}_N, \omega_N) \quad (3.1)$$

where the angular brackets  $\langle \dots \rangle$  indicate a statistical average over all required positions and orientations. If the probability density  $P^{(1)}(\mathbf{r}, \omega)$  for a molecule to have a certain position ( $\mathbf{r} + d\mathbf{r}$ ) and orientation ( $\omega + d\omega$ ) is known, the average of any property  $A(\mathbf{r}, \omega)$ , relating to a single molecule can be calculated as

$$\langle A \rangle = \langle A(\mathbf{r}, \omega) \rangle_{\mathbf{r}, \omega} = \int d\mathbf{r} d\omega A(\mathbf{r}, \omega) P^{(1)}(\mathbf{r}, \omega) / N \quad (3.2)$$

Therefore  $P^{(1)}$  contains all the microscopic information necessary to calculate one particle properties and viceversa the structure and order of the system will be reflected by  $P^{(1)}$ . Thus the organization in liquid crystal phases can be characterized first by the one particle probability distribution function  $P^{(1)}(\mathbf{r}, \omega)$  of finding a molecule at position  $\mathbf{r}$  with orientation  $\omega$ . A common and useful way of writing the singlet distribution is through the Dirac delta functions. Indeed, since  $\delta(\mathbf{r}_1 - \mathbf{r}'_1)$  is different from zero only when the position  $\mathbf{r}_1$  of molecule 1 is  $\mathbf{r}'_1$ , we can use a delta function as a device for counting the molecules at a certain position–orientation

$$P^{(1)}(\mathbf{r}_1, \omega_1) / N = \langle \delta(\mathbf{r}_1 - \mathbf{r}'_1) \delta(\omega_1 - \omega'_1) \rangle_{\mathbf{r}'_1, \omega'_1} \quad (3.3)$$

which gives the average number of molecules with the desired position–orientation.

### 3.2.1 Orientational order

The description of long range orientational order, is a central issue when treating LC systems, since this type of order is common to all the various mesophases. If we consider a molecule as a rigid uniaxial particle we can specify its orientation  $\omega$  with respect to a laboratory frame with the Euler angles  $(\alpha, \beta)$ ,  $0 \leq \alpha \leq 2\pi$ ;  $0 \leq \beta \leq \pi$ . In general we can obtain a purely orientational distribution  $P(\omega)$  integrating out positions in eq. 3.3. For uniform fluids such as nematics, the singlet probability is independent of the position of molecules:  $P^1(\mathbf{r}, \omega) = \rho P(\omega)$  where  $\rho = N/V$  is the number density. The probability of finding the molecule at a certain orientation with respect to the axis of the mesophase is

$$P(\omega) = P(\alpha, \beta). \quad (3.4)$$

If the laboratory  $Z$  axis is taken along the director of the phase and if the mesophase is uniaxial around the director, then rotating the sample around  $Z$  should leave all the observable properties unchanged. This means that the probability for a molecule to have an orientation  $(\alpha, \beta)$  should be the same, independently of the angle  $\alpha$ , i.e.  $P(\alpha, \beta) = P(\beta)/2\pi$ . A useful approach is that of expanding  $P(\beta)$  in an orthogonal basis set and connecting the expansion coefficients to a set of observable quantities that we can obtain from experiment [62]. A suitable set of orthogonal functions (when integrated over  $d\beta \sin\beta$ ) is that of Legendre polynomials  $P_L(\cos\beta)$  [63, 64] for which we have

$$\int_0^\pi d\beta \sin\beta P_L(\cos\beta) P_N(\cos\beta) = \frac{2}{2L+1} \delta_{LN}. \quad (3.5)$$

The explicit form of the first few Legendre polynomials is [64]:

$$\begin{aligned}
P_0(\cos \beta) &= 1 \\
P_1(\cos \beta) &= \cos \beta \\
P_2(\cos \beta) &= \frac{3}{2} \cos^2 \beta - \frac{1}{2} \\
P_3(\cos \beta) &= \frac{5}{2} \cos^3 \beta - \frac{3}{2} \cos \beta \\
P_4(\cos \beta) &= \frac{35}{8} \cos^4 \beta - \frac{30}{8} \cos^2 \beta + \frac{3}{8}
\end{aligned} \tag{3.6}$$

Notice that  $P_L(\cos \beta)$  is an even function of  $\cos \beta$  if the rank  $L$  is even and viceversa. For normal nematics and smectics, there is a head to tail symmetry

$$P(\beta) = P(\pi - \beta) \tag{3.7}$$

and only even  $L$  terms need to be retained in writing the even orientational distribution in terms of  $P_L(\cos \beta)$  functions. However in some cases, it is useful to consider also odd  $L$  terms, e.g. when testing for the existence of polar ferroelectric phases [65–67]. In general:

$$P(\beta) = \sum_{L=0}^{\infty} \frac{2L+1}{2} \langle P_L \rangle P_L(\cos \beta) \tag{3.8}$$

where the coefficients have been obtained exploiting the orthogonality of the basis set. The average

$$\langle P_L \rangle = \int_0^\pi d\beta \sin \beta P_L(\cos \beta) P(\beta) / \int_0^\pi d\beta \sin \beta P(\beta) \tag{3.9}$$

represents the orientational order parameter of rank  $L$ . The knowledge of the set of  $\langle P_L \rangle$  completely defines the distribution:

$$P(\beta) = \frac{1}{2} + \frac{3}{2} \langle P_1 \rangle P_1(\cos \beta) + \frac{5}{2} \langle P_2 \rangle P_2(\cos \beta) + \frac{7}{2} \langle P_3 \rangle P_3(\cos \beta) + \frac{9}{2} \langle P_4 \rangle P_4(\cos \beta) + \dots \tag{3.10}$$



The most common and useful term is the second rank order parameter

$$\langle P_2 \rangle = \frac{3}{2} \langle \cos^2 \beta \rangle - \frac{1}{2}. \quad (3.11)$$

$\langle P_2 \rangle$  has the properties one could expect from a good order parameter: for a system of molecules perfectly aligned  $\beta = 0$ , so  $\langle P_2 \rangle = 1$ ; on the other hand, for a system completely disordered (isotropic fluid)  $\langle \cos^2 \beta \rangle = \frac{1}{3}$  and thus  $\langle P_2 \rangle = 0$ . In general

$$0 \leq \langle P_2 \rangle \leq 1. \quad (3.12)$$

This treatment can be extended to rigid molecules of arbitrary symmetry and to complex phases, expanding  $P(\alpha, \beta, \gamma)$  in a set of Wigner matrices  $D_{m,n}^L$ , orthogonal in  $(\alpha, \beta, \gamma)$  space and systematically applying the symmetry properties of the molecules and of the phase [62].

### 3.2.2 Second rank order parameter

The second rank order parameter  $\langle P_2 \rangle$  can be calculated by averaging  $P_2(\cos \beta)$  over the probability  $P(\beta)$  of finding the molecule at an orientation  $\beta$  with respect to the director (see Eq. 3.9). In the ordinary MC method we do not work in a director frame but in an arbitrary, fixed, laboratory frame. In the absence of a preferred direction imposed, for example by an external electric or magnetic field, the director  $\hat{n}$  is not fixed *a priori* in the laboratory frame, but can fluctuate during the simulations from one configuration to another one. Thus, in principle, we have to determine  $\hat{n}$  for each configuration produced in the MC chain, in order to compute the values of the orientational order parameters. The problem is solvable introducing a single molecule matrix property  $\mathbf{A}$  [62, 68], whose only non vanishing component is along the molecule symmetry axis, that is we can define  $\mathbf{A}$  as the direct square of a vector  $\mathbf{u}$  taken along the molecular axis

$$\mathbf{A} = \mathbf{u} \otimes \mathbf{u}, \quad (3.13)$$

where  $\mathbf{u} = (0, 0, 1)$  in the molecule fixed frame. The sample average of  $\mathbf{A}$  in our arbitrary laboratory frame is obtained relating the components of  $\mathbf{A}$  to the molecule fixed components and summing over all particles:

$$\begin{aligned}\langle A_{ab}^{LAB} \rangle_S &= \frac{1}{N} \sum_{i=1}^N \sum_{a'b'} (R_i)_{aa'} (A_i)_{a'b'}^{MOL} (\tilde{R}_i)_{b'b} \\ &= \langle \mathbf{R}_{az} \mathbf{R}_{bz} \rangle_S \\ &= Q_{ab} + \frac{1}{3} \delta_{ab}\end{aligned}\tag{3.14}$$

where  $\mathbf{R}$  is the orthogonal matrix rotating from the laboratory to the molecular frame and we have taken advantage of the fact that  $A_{ab}^{MOL} = \delta_{az} \delta_{bz}$ ;  $\langle \dots \rangle_S$  indicates an average over the sample and where we have defined the ordering matrix  $\mathbf{Q}$  as

$$Q_{ab} = \langle R_{az} R_{bz} - \frac{1}{3} \delta_{ab} \rangle_S.\tag{3.15}$$

Notice that  $\mathbf{Q}$  is symmetric and traceless. The director frame is identified diagonalizing the  $\langle \mathbf{A}^{LAB} \rangle_S$  or the  $\mathbf{Q}$  tensor. We shall take the instantaneous director to be parallel to the direction  $Z$ , defined by the eigenvector associated with the largest eigenvalue of  $\mathbf{A}$  [62, 69]. Then we can obtain the second rank order parameter since

$$\begin{aligned}\langle A_{ZZ}^{DIR} \rangle_S &= \sum U_{aZ} U_{bZ} \langle A_{ab}^{LAB} \rangle_S \\ &= \langle \cos^2 \beta \rangle_S \\ &= \frac{2}{3} \langle P_2 \rangle_S + \frac{1}{3},\end{aligned}\tag{3.16}$$

where  $\mathbf{U}$  is the matrix rotating the laboratory into the director frame (i.e. the matrix of eigenvectors of  $\langle \mathbf{A}^{LAB} \rangle_S$ ) and the angle  $\beta$  gives the orientation of the molecular axis in the director frame. In practice we calculate and diagonalize the  $\mathbf{Q}$  tensor for every configuration we wish to use, say  $\mathbf{Q}^{(\mathcal{J})}$  for the  $\mathcal{J}$ -th one. By diagonalizing  $\mathbf{Q}^{(\mathcal{J})}$  we obtain an order parameter

$P_2^{(\mathcal{J})}$  and a director  $\hat{\mathbf{n}}^{(\mathcal{J})}$ , that can change from one configuration to the next.  $P_2^{(\mathcal{J})}$  is obtained maximizing the expression

$$\langle P_2 \rangle_s^{(\mathcal{J})} = \frac{1}{N} \sum_{i=1}^N P_2(\hat{\mathbf{u}}_i \cdot \hat{\mathbf{n}}^{(\mathcal{J})}), \quad (3.17)$$

with respect to the unit vector  $\hat{\mathbf{n}}^{(\mathcal{J})}$ . If the director  $\hat{\mathbf{n}}^{(\mathcal{J})}$  is parallel to the  $Z$  axis we see immediately that

$$\mathbf{Q} = \begin{pmatrix} -\frac{1}{3}\langle P_2 \rangle_s - \xi & 0 & 0 \\ 0 & -\frac{1}{3}\langle P_2 \rangle_s + \xi & 0 \\ 0 & 0 & \frac{2}{3}\langle P_2 \rangle_s \end{pmatrix}. \quad (3.18)$$

The sample biaxiality parameter  $\xi$  corresponds to different ordering with respect to the laboratory  $X$  and  $Y$  axis and will tend to zero at large sample size if the mesophase has uniaxial symmetry [70].

### 3.3 Pair properties

After discussing the single particle distribution  $P^{(1)}(\mathbf{r}, \omega)$  which gives the probability of finding a molecule at a particular position and orientation, and its expansion, we now focus on the pair distribution, which defines the probability  $P^2(\mathbf{r}_1, \omega_1, \mathbf{r}_2, \omega_2)$  of finding any two particles at  $(\mathbf{r}_1, \omega_1, \mathbf{r}_2, \omega_2)$  considering a pair property  $A(\mathbf{r}_1, \omega_1, \mathbf{r}_2, \omega_2)$ , whose average is

$$\langle A(\mathbf{r}_1, \omega_1, \mathbf{r}_2, \omega_2) \rangle_{\mathbf{r}, \omega} = \frac{1}{N(N+1)} \int d\mathbf{r}_1 d\omega_1 d\mathbf{r}_2 d\omega_2 A(\mathbf{r}_1, \omega_1, \mathbf{r}_2, \omega_2) P^{(2)}(\mathbf{r}_1, \omega_1, \mathbf{r}_2, \omega_2). \quad (3.19)$$

We can write this pair distribution using delta functions for counting the molecules at a certain position–orientation:

$$P^{(2)}(\mathbf{r}_1, \omega_1, \mathbf{r}_2, \omega_2) / [N(N-1)] = \langle \delta(\mathbf{r}_1 - \mathbf{r}'_1) \delta(\omega_1 - \omega'_1) \delta(\mathbf{r}_2 - \mathbf{r}'_2) \delta(\omega_2 - \omega'_2) \rangle. \quad (3.20)$$

The last form is useful to evaluate the pair distribution by computer simulation; in practice the delta functions are replaced by functions which are non-zero in a small range of separations or orientations, and a multidimensional histogram is constructed for all pair separations and also orientations falling within such range. The pair distribution will reduce for large intermolecular separations to the product of the singlet distributions for the two molecules:  $P(\mathbf{r}_1, \omega_1)$ ,  $P(\mathbf{r}_2, \omega_2)$ , that is

$$\begin{aligned} \lim_{r \rightarrow \infty} \langle \delta(\mathbf{r}_1 - \mathbf{r}'_1) \delta(\omega_1 - \omega'_1) \delta(\mathbf{r}_2 - \mathbf{r}'_2) \delta(\omega_2 - \omega'_2) \rangle \\ = \langle \delta(\mathbf{r}_1 - \mathbf{r}'_1) \delta(\omega_1 - \omega'_1) \rangle \langle \delta(\mathbf{r}_2 - \mathbf{r}'_2) \delta(\omega_2 - \omega'_2) \rangle. \end{aligned} \quad (3.21)$$

At short and intermediate distances the position-orientation of the two molecules are correlated. The spatial–orientational correlation is expressed by the reduced pair distribution function or simply *pair correlation function*:

$$g^{(2)}(\mathbf{r}_1, \omega_1, \mathbf{r}_2, \omega_2) \equiv P^{(2)}(\mathbf{r}_1, \omega_1, \mathbf{r}_2, \omega_2) / P(\mathbf{r}_1, \omega_1) P(\mathbf{r}_2, \omega_2), \quad (3.22)$$

so that  $g^{(2)}(\mathbf{r}_1, \omega_1, \mathbf{r}_2, \omega_2)$  goes to one in the limit of large intermolecular separations

$$\lim_{r_{12} \rightarrow \infty} g(\mathbf{r}_1, \omega_1, \mathbf{r}_2, \omega_2) = 1, \quad (3.23)$$

i.e. the density of particles at large distances just becomes that of the bulk. Moreover, for uniform systems we can write

$$P^{(2)}(\mathbf{r}_1, \omega_1, \mathbf{r}_2, \omega_2) = \rho^2 P(\omega_1) g^{(2)}(\mathbf{r}_1, \omega_1, \mathbf{r}_2, \omega_2). \quad (3.24)$$

Given the anisotropy of liquid crystals, it is useful to define distributions along different orientations  $\omega_{12}$  of the intermolecular vector relative to the director. Considering a molecule as the origin, i.e. assuming  $\mathbf{r}_{12} \equiv \mathbf{r}$ , the distributions along different orientations  $\omega_r$ , are obtained by integration over the orientations of the two particles and the position of the first particle [67, 71, 72]:

$$g(r, \omega_r) = \frac{\int d\mathbf{r}_1 d\omega_1 d\omega_2 g^{(2)}(\mathbf{r}_1, \omega_1; \mathbf{r}_1 + \mathbf{r}, \omega_2)}{\int d\mathbf{r}_1 d\omega_1 d\omega_2} \quad (3.25)$$

This quantity gives the probability of finding a particle at a certain distance  $r$  from a particle chosen as origin when their intermolecular vector has orientation  $\omega_r = (\alpha_r, \beta_r)$ . If the system investigated is uniaxial, and we consider orientations defined with respect to a laboratory system with  $Z$  axis parallel to the director, we do not need to consider the angle  $\alpha_r$  and the intermolecular vector distribution reduces to  $g(\mathbf{r}) = g(r, \beta_r)/2\pi$ . Thus, by integrating the  $g^{(2)}(\mathbf{r}, \omega_1, \omega_2)$  over the orientations of the two particles, one obtains the intermolecular vector correlation function [67]

$$g_0(\mathbf{r}) = \frac{1}{64\pi^4} \int d\omega_1 d\omega_2 g^{(2)}(\mathbf{r}, \omega_1, \omega_2) \quad (3.26)$$

which gives the probability for the intermolecular vector to have module  $r$  and orientation  $\omega_r$ . The intermolecular vector correlation function  $g(r, \beta_r)$

can be expanded in series of Legendre polynomials as

$$g(r, \beta_r) = g_0(r) \sum_L (2L+1) g_L^+(r) P_L(\cos \beta_r) \quad (3.27)$$

where  $g_0(r)$  is the standard *radial distribution*

$$\begin{aligned} g_0(r) &= \frac{1}{2} \int d\beta_r \sin \beta_r g(r, \beta_r) \\ &\equiv \frac{1}{4\pi r^2 \rho} \langle \delta(r - r_{12}) \rangle_{ij} \end{aligned} \quad (3.28)$$

giving the probability of finding a molecule inside the spherical shell  $r \pm dr$  from another molecule. Notice that in the second form of eq. 3.28, a delta function is used as before as a device for counting the molecules with a certain separation; here  $\langle \dots \rangle_{ij}$  is the average computed over all the molecular pairs  $i, j$ , while  $4\pi r^2 \rho$  represents the average number of molecular pairs having separation  $r$  for an isotropic fluid.

In computer simulations it is useful to replace the delta functions with functions which are non-zero in a small range of separations;  $g(r)$  is constructed by computing an histogram of all pair separations falling within such range, i.e.  $r_{12} \in [r : r + \delta r]$  where  $r \in [0 : L_{min}/2]$  and  $L_{min}$  is the shortest simulation box length. The histogram bin heights represent the average particle occupancies in concentric spherical shells around any particle taken as reference (see Figure 3.1). In order to obtain  $g(r)$ , the histogram must be normalized by the average expected occupancy of an ideal gas at the same density. In order to obtain a smooth function, it is also required averaging  $g(r)$  over several uncorrelated configurations, taken during the course of a simulation, to obtain a smooth function. This means that the histogram must be normalized also by the number of configurations and the number of particles used. In the case of liquid crystalline phases, it is necessary to consider different distribution functions in different directions due to the anisotropic nature of the fluid. In particular the distribution functions resolved along directions parallel and perpen-

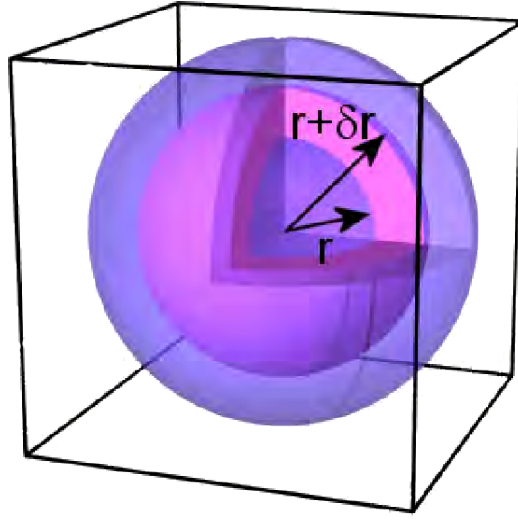
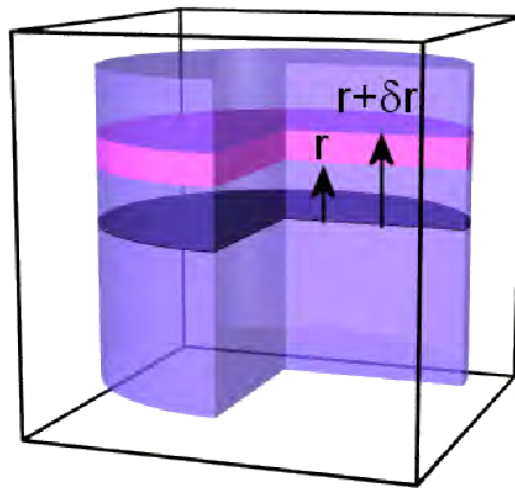


Figure 3.1: Representation of the volume corresponding to a spherical shell between the distance  $r + \delta r$  adapted from [73].

pendicular to the director, respectively  $g_{\parallel}(r_{\parallel})$  and  $g_{\perp}(r_{\perp})$  are useful to study smectic phases. The approach used in computing these functions is very similar to that used for  $g(r)$ : the histograms of the projection of  $\mathbf{r}_{12}$  parallel ( $r_{\parallel} = \hat{\mathbf{n}}\mathbf{r}_{12}$ ) and perpendicular ( $r_{\perp} = \sqrt{r_{12}^2 - r_{\parallel}^2}$ ) to the director  $\hat{\mathbf{n}}$  are considered. In order to simplify the process, all histograms are computed within a cylindrical geometry, as shown in Figure 3.2.



$$g_{\parallel}(r_{\parallel})$$

Figure 3.2: Representation of the volumes corresponding to a cylindrical shell between the distance  $r + \delta r$ , as used for the computation of  $g_{\parallel}(r_{\parallel})$  and  $g_{\perp}(r_{\perp})$  adapted from [73].



## 3.4 Aggregate analysis

The first step in aggregation analysis is to determine aggregate in systems. Clusters determination are based on the minimum neighbour distance criteria. With this method two NPs are assigned to the same cluster if the distance between their centers is less than some distance  $R_{agg}$ . In order to assess also the shape of the resulting aggregate, beyond the visual analysis of the snapshots, we have calculated the aggregate principal radii of gyration and, from them, the asphericity parameters for each formed cluster. The procedure is as follows: for each configuration we first calculate the radius of gyration<sup>1</sup> tensor for every aggregate. Next, we diagonalize the matrix to find three eigenvalues, says  $R_x^2$ ,  $R_y^2$  and  $R_z^2$ , which we order from the smallest to the largest. We then find the average of each ordered eigenvalue, over all aggregates, and then take the square root of these averages. The results are the mean-squared princial radii of gyration of aggregate  $(R_i^2)^{1/2}$  with  $i = 1, 2, 3$ . The asphericity parameter is a single number characterizing the shape, calculated from  $R_i^2$  through

$$\alpha_S = \frac{\sum_{i>j=1}^3 (\langle R_i^2 \rangle - \langle R_j^2 \rangle)^2}{2(\sum_{i=1}^3 \langle R_i^2 \rangle)^2} \quad (3.29)$$

Clearly if the aggregate is a perfect sphere, all the principal radii of gyration are equal and  $\alpha_S = 0$ , if it is elongated along one direction, the two smaller one are equal and  $\alpha_S > 0$ .

### 3.4.1 Nanoparticle diffusion

It is interesting to try to extend to Monte Carlo simulations the study on molecular diffusion, typically examined via MD simulations by taking into account the dynamics of particles affecting the transport properties. This is not possible in general, since the MC dynamic is an arbitrary Markov one

---

<sup>1</sup>Radius of gyration defined as  $R_g = r^{mc} - r^i$

that we have assumed. However, if we only consider realistic MC moves (e.g. small translations and rotations), some dynamic information can be gathered, although on a MC time scale and not a real one. In particular understanding the translational diffusion of nanoparticles in bulk solvent, in relation to particle size, could be interesting i.e. in their use as tracer particles. The translational motion of particles may be analyzed through the self-diffusion coefficient

$$D_t = \frac{1}{6} \lim_{t \rightarrow \infty} \frac{d}{dt} \langle |\mathbf{r}_c(t) - \mathbf{r}_c(0)|^2 \rangle = \frac{1}{6} \lim_{t \rightarrow \infty} \frac{d}{dt} \langle \Delta r^2 \rangle \quad (3.30)$$

where  $\mathbf{r}_c(t)$  is the centre of mass position of the nanoparticle at time  $t$  and the angled brackets denote averaging over different time origins.  $D_t$  is extracted from the slope of the mean-squared diffusion (MSD) at long times. MSD in our case could be defined as

$$\langle \Delta r^2(n) \rangle = \langle (r_n - r_0)^2 \rangle \quad (3.31)$$

where  $r - r_0$  is the displacement vector moved by a given particle in  $n$  consecutive MC moves per particle and the angled brackets indicate an average over all particles and the run length. Even if we cannot access true dynamics of the systems, since we perform MC simulations, we can still consider these as useful indicators: the greater the gradient of  $\langle \Delta r^2 \rangle$  the more fluid the studied phase. As may be expected the translational motion of the NP depends on the particle radius with smaller particles diffusing more rapidly.

### Relation between rotational and translational diffusion

For a sphere in an ordinary (isotropic) liquid the diffusion tensor components can be related, in the stick boundary hydrodynamic limit, to the vis-

cosity, via the Stoke–Einstein relation.

$$D_t \equiv \frac{kT}{f_{trans}} = \frac{kT}{6\pi\eta r} = \frac{4}{3}D_{rot}r^2\pi \quad (3.32)$$

$$D_{rot} = \frac{kT}{6\pi\eta(\frac{4}{3}\pi r^3)} \quad (3.33)$$

Notice that strictly one should use the equivalent of the Stokes–Einstein relation in a medium like a liquid crystal, where the viscosity itself is a tensor. In a situation where relations like 3.32 or 3.33 are valid it is possible to get informations on translational diffusion from rotational diffusion data (e.g. from spin probe techniques). Equations for the brownian motion of an ellipsoid (with semiaxes  $a, b=c$ ) in an isotropic liquid:

### Translation

$$X_0 = f_1 u \quad (3.34)$$

$$Y_0 = f_2 v \quad (3.35)$$

$$Z_0 = f_3 w \quad (3.36)$$

where  $X, Y, Z$  are viscous force and  $u, v, w$  are velocity components;  $f_1, f_2, f_3$  are translational friction coefficients.

$$f_1 = 16\pi\eta \frac{a^2 - b^2}{(2a^2 - b^2)S - 2a} \quad (3.37)$$

$$f_2 = f_3 = 32\pi\eta \frac{a^2 - b^2}{(2a^2 - 3b^2)S + 2a} \quad (3.38)$$

## Rotation

The friction coefficients  $\beta_1, \beta_2, \beta_3$  are

$$\beta_1 = \frac{32}{3} \pi \eta \frac{(a^2 - b^2)b^2}{2a - b^2 S} \quad (3.39)$$

$$\beta_2 = \beta_3 = \frac{32}{3} \pi \eta \frac{a^2 - b^2}{(2a^2 - b^2)S - 2a} \quad (3.40)$$

where  $\eta$  is the viscosity.

$$S = \int_0^\infty \frac{ds}{(b^2 + s)\sqrt{a^2 + s}} \quad (3.41)$$

For  $a > b$  (elongated, prolate, ellipsoid) this reduces to

$$S = \frac{2}{\sqrt{a^2 - b^2}} \log_a \frac{a + \sqrt{a^2 - b^2}}{b} \quad (3.42)$$

For  $a < b$  (oblate, disk-like ellipsoid)

$$S = \frac{2}{\sqrt{b^2 - a^2}} \operatorname{arctg} \frac{\sqrt{b^2 - a^2}}{a} \quad (3.43)$$

Remember that

$$D_i^{\text{trasl}} = \frac{kT}{f_i} \quad (3.44)$$

$$D_i^{\text{rot}} = \frac{kT}{\beta_i} = R_i \equiv D_i^R \quad (3.45)$$

We can obtain simple approximate for  $f_i, \beta_i$  in limiting situation, e.g. for a

very elongated ellipsoid  $a \gg b$  in the sense that  $a^2 - b^2 \sim a^2$ .

$$S = \frac{2}{a} \ln \frac{2a}{b} \quad (3.46)$$

$$\beta_1 = \beta_{//} = \frac{16}{3} \pi \eta \frac{a^3}{\left(\frac{a}{b}\right)^2 - \ln \frac{2a}{b}} \quad (3.47)$$

$$\beta_2 = \beta_3 = \beta_{\perp} = \frac{16}{3} \pi \eta \frac{a^3}{2 \ln \frac{2a}{b} - 1} \quad (3.48)$$

so that for  $a \gg b$

$$D_{//}^R \sim \frac{3kT}{16\pi\eta a^3} \left[ \left(\frac{a}{b}\right)^2 - \ln \frac{2a}{b} \right] \quad (3.49)$$

$$D_{\perp}^R \sim \frac{3kT}{16\pi\eta a^3} \left[ 2 \ln \frac{2a}{b} - 1 \right] \quad (3.50)$$

Notice that  $D_{//}/D_{\perp}$  should be independent of  $\eta$ ,  $T$  and only depend on  $a/b$  (This is true in general, not just for  $a > b$  of course).

Again for  $a \gg b$  we find

$$f_1 = f_{//} = 8\pi\eta a \left[ 2 \ln \frac{2a}{b} - 1 \right]^{-1} \quad (3.51)$$

$$f_2 = f_3 = f_{\perp} = 16\pi\eta a \left[ 2 \ln \frac{2a}{b} + 1 \right]^{-1} \quad (3.52)$$

Therefore for  $a \gg b$

$$D_{//}^T = \frac{kT}{8\pi\eta a} \left( 2 \ln \frac{2a}{b} - 1 \right) \quad (3.53)$$

$$D_{\perp}^T = \frac{kT}{16\pi\eta a} \left( 2 \ln \frac{2a}{b} + 1 \right) \quad (3.54)$$



## **Chapter 4**

### **Results – Doping LC with nanoparticles.**

#### **Effect of shape and size**

As was presented in Chapter 1, there are many key factors that affect the stability and properties of the liquid crystalline phase. In the first part of this dissertation we study in detail the effect of the nanoparticles shape, taking into account three different shapes, while in the second part we concentrate on the effect of nanoparticle size (see sketch in Figure 4.1). To perform this study, we start from the nanoparticle model introduced in Chapter 2, to build four distinct nanoparticles by arranging in different ways their forming units (spherical LJ sites) according to different symmetries and sizes.

#### **4.1 Pure mesogen simulations**

We have first performed Monte Carlo simulations on a pure mesogenic rod-like system, which will be the reference for the following investigations. As already explained in Chapter 2, we have modelled the rod mesogen

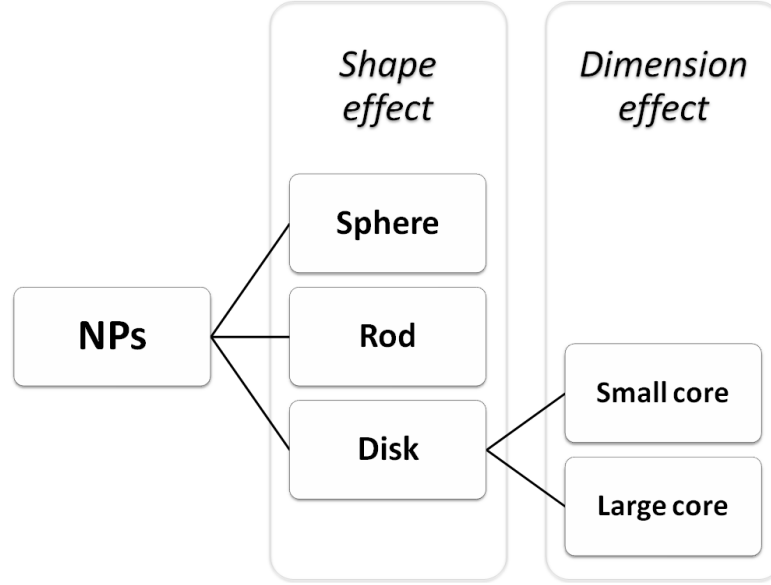


Figure 4.1: Schematic representation of the work illustrate on this Chapter.

through a Gay–Berne potential [58] with a parameterization already used by [74–76], namely:  $\sigma_x = \sigma_y = 1, \sigma_z = 3$ , interaction well depth  $\varepsilon_x = \varepsilon_y = 1, \varepsilon_z = 0.2$ , and energy parameters  $\mu = 2$  and  $\nu = 1$ . Here  $\sigma_0$  and  $\varepsilon_0$  are used as molecular units of length and energy, which taking the 5CB as typical elongated mesogenic molecule can be approximated as 6 Å and 0.2 kcal/mol. The interaction cutoff radius adopted is  $R_c^{(GB)} = 4\sigma_0$ .

We considered systems of  $N = 1000$  GB rods contained in a orthogonal box with periodic boundary conditions, in the isothermal–isobaric ensemble (NPT). We kept the dimensionless pressure  $P^* = 8$  fixed, while varying the temperatures  $T^*$  in a range wide enough to observe both isotropic–nematic and nematic–smectic transitions. We performed a series of simulations in a progressive cooling sequence, starting from an isotropic sample ( $T^* = 1.8$ ), where each new lower temperature was studied using as starting configuration an equilibrated one resulting from the previous simulation at higher temperature. For each temperature, we first let the system equilibrate for 2000 kcycles, then we have collected observables during production runs of 500 kcycles.



From the simulations we computed the equilibrium averages of several physical quantities, like the adimensional energy  $\langle U^* \rangle$  and the orientational order parameter (Figure 4.2), as well as instantaneous configuration snapshots like the one in Figure 4.3, showing three state points in different mesophase regions.

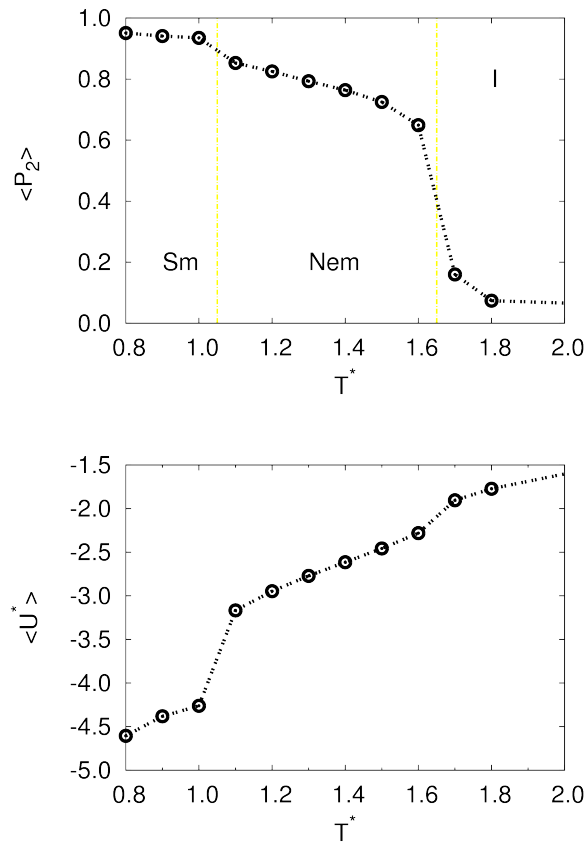


Figure 4.2: Average simulation values for adimensional energy  $\langle U^* \rangle$  and orientational order parameter  $\langle P_2 \rangle$  versus temperature  $T^*$ . Pressure is  $P^* = 8$ . Three regions are shown, corresponding to stable mesophases, i.e. Sm (smectic), Nem (nematic) and I (isotropic).

These instantaneous configurations show at once that the phases obtained on cooling correspond to isotropic, nematic, smectic A or B. To provide an immediate visualization of the existing short and long range order, here and in the following, LC molecules are represented with ellip-

soidal particles and their orientation is indicated by a colour code ranging from yellow to blue (see palette on the right of Figure 4.3). In particular at  $T^* = 1.7$ , it is visible a steep increase in  $\langle P_2 \rangle$  corresponding to the first order isotropic–nematic transition, while at  $T^* = 1.15$  a further jump in  $\langle P_2 \rangle$  denotes the nematoc–to–smectic transition.

Structural informations can be obtained from the radial distribution function  $g_0(r)$  which, as explained in Chapter 3, estimates the probability of finding other molecules at a given radius from each mesogen composing the system, averaged on all the configurations. The radial distribution in particular shows a sharp peak at  $r^* = 1$ , corresponding to the *side–side* configuration (see Figure 4.4). At lowest temperature ( $T^* = 1.0$ ) the radial distribution shows also a splitting of the second peak, characteristic of hexagonal order in the plane and thus of a smectic B type ordering. The density profile along the director  $g(z)$  shows a clear smectic periodicity with peaks essentially centered at slightly lower values of multiples of the molecular length  $\sigma_z$ , confirming a partial interdigitation of smectic layers.

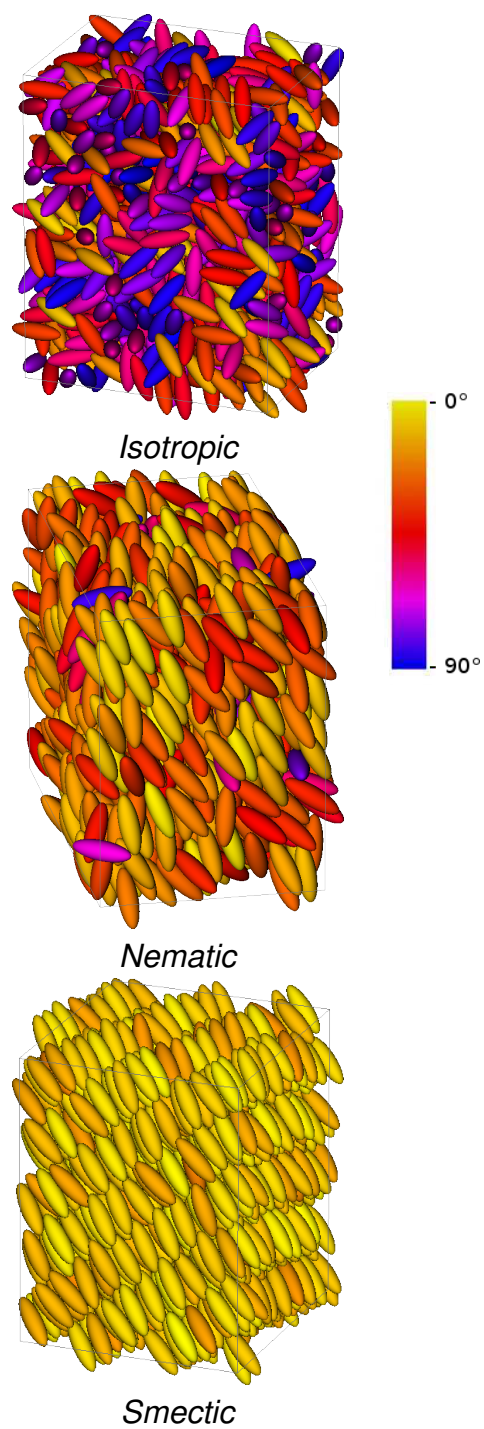


Figure 4.3: Molecular organization for the  $N = 1000$  system in isotropic  $T^* = 1.8$ , nematic  $T^* = 1.5$ , and smectic  $T^* = 1.0$ , phase. The palette is also shown on the right.

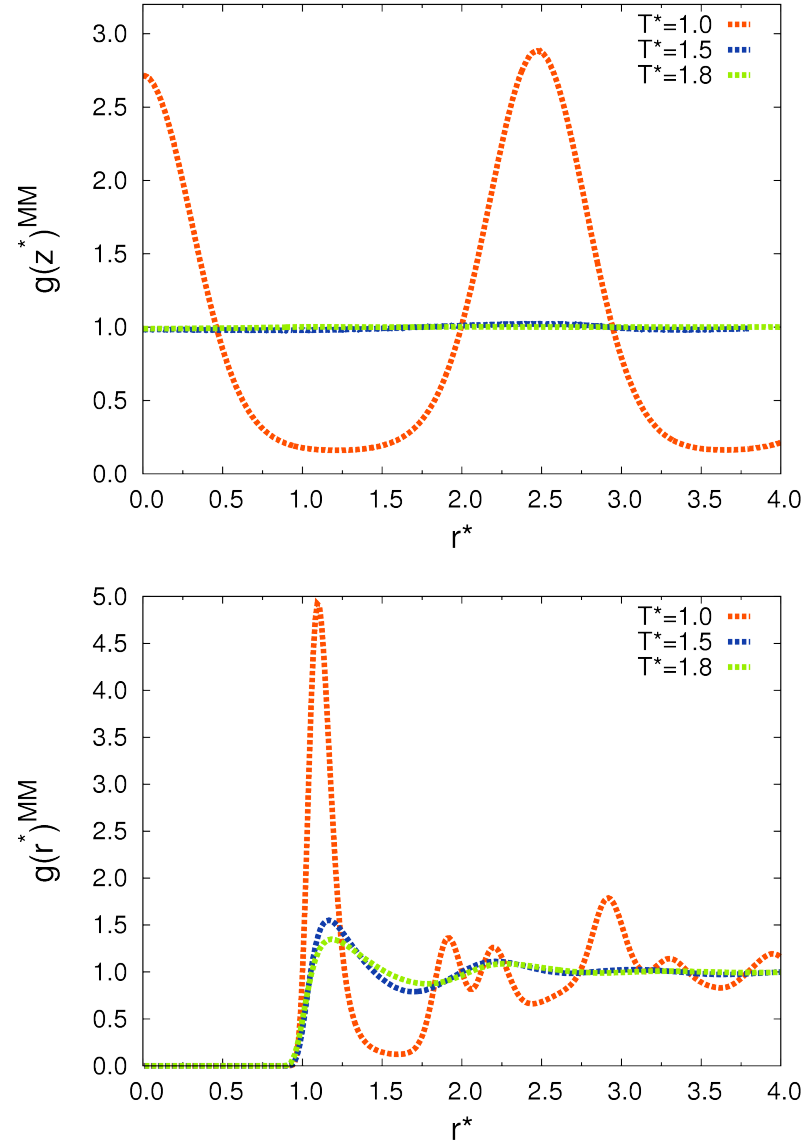


Figure 4.4: Radial correlation function (bottom) and density correlation function (top) along the director in smectic B ( $T^* = 1.0$ ) and nematic ( $T^* = 1.5$ ) and isotropic ( $T^* = 1.8$ ) phase.

## 4.2 Effect of nanoparticle shape

We studied the effect of the shape of dopant NP on the mesophase organization, and ordering in a system of rod-like Gay-Berne molecules. Three different NP shapes are considered: spherical, rod-like, disk-like. For all these cases, we considered three possible concentrations of dopant NP and performed temperature scans in order to monitor the mesogen orientational order, as well as locate the isotropic-nematic phase transitions. The nanoparticle-mesogen coupling parameter ( $e_{NM}$ ) was set to a maximum value (i.e.  $e_{NM} = 2.0$ ) in order to avoid phase separation and aggregation of NPs.

### 4.2.1 Sphere-shaped Nanoparticle

Spherical nanoparticles are assumed as closed packed bulk clusters of 32 identical Lennard-Jones (LJ) sites which can be viewed as a stacking of 4 dense LJ layers, where each of the two inner layers has an octagonal basis and contains 12 LJ spheres, while the two outer have a square basis and contains 4 LJ spheres (see Figure 4.5). LJ spheres have dimensions  $\sigma_S = \sigma_x = \sigma_y = \sigma_z = 2.0\sigma_0$  and are slightly overlapping, in order to form a quasi spherical shape of diameter  $\approx 6\sigma_0$  without large surface discontinuities.

Concerning the energetic parameterization, we choose well depths:  $\varepsilon_S = \varepsilon_x = \varepsilon_y = \varepsilon_z = 0.15\varepsilon_0$ , while the exponents  $\mu$  and  $\nu$  were set to 2 and 1 respectively, as for the model of the pure LC (Figure 4.6).

In Figure 4.7 we show the representative pair potential profiles relative to the homogeneous interaction NN, as well as the heterogeneous NM one. We note that for the chosen coupling parameter, the NM interaction strengths (well depths) relative to lateral (*side-side*) configuration is almost equal to the (nearly spherically symmetric) NN interaction, while it is slightly larger than the *end-end* NM interaction; this suggests that a weak planar anchoring is preferred, because the configurational interaction corresponding to planar anchoring is energetically slightly more favored than

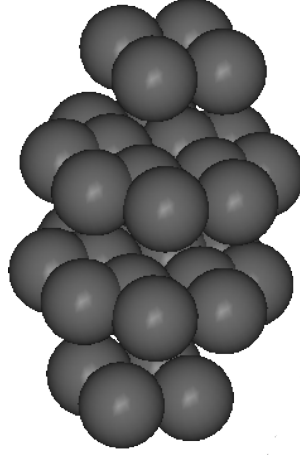
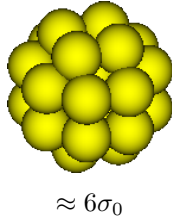


Figure 4.5: Exploded view of the four LJ layers forming the sphere-shaped nanoparticle.



	$\sigma_S$			$\varepsilon_S$		
	$\sigma_x$	$\sigma_y$	$\sigma_z$	$\varepsilon_x$	$\varepsilon_y$	$\varepsilon_z$
Sphere	2.0	2.0	2.0	0.15	0.15	0.15

Figure 4.6

the homeotropic one. We used as potential cutoff radius  $r_c^{*(GB)} = 4.0$  for the mesogen–mesogen interaction and  $r_c^{*(LJ)} = 6$  for the interaction between spherical sites, while that for the mixed interaction is calculated through the mixing rules adopted in [77].

Simulations have been performed of sample mixtures of  $N = N_M + N_N = 4000$  total particles with  $N_N = 4, 8, 20$ , corresponding respectively to the numerical nanoparticles concentration 0.1%, 0.2%, 0.5%, in the isobaric–isothermal (NPT) ensemble, using 3d periodic conditions. As in the pure LC system, dimensionless pressure  $P^*$  was set to 8, while the temperature  $T^*$  spanned the range 1.0 – 1.8. For each concentration, MC experiments were run in a cooling sequence starting from well equilibrated isotropic configurations, obtained inserting the proper number of uniformly embedded nanoparticles in the previously equilibrated pure LC configuration at

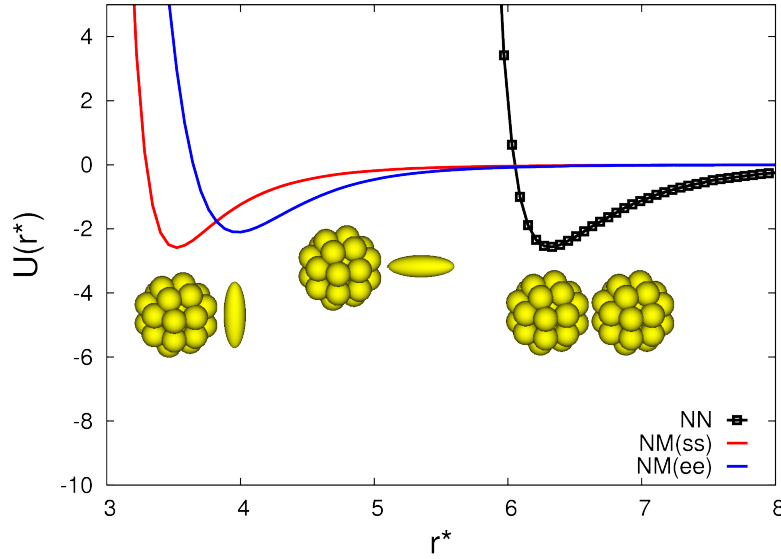


Figure 4.7: Pair potential profiles relative to homogeneous interaction NN and heterogeneous NM for pairs in *side-side* (ss) and *end-end* (ee) configurations.

the same pressure and temperature. In Figure 4.8 we plot the resulting temperature dependence of the orientational order parameter.

From the plots we see that, compared to the pure LC, all systems undergo a general decrease of the LC orientational order for all the concentrations. Also, for the  $c = 0.2\%$  and  $0.5\%$  cases, a shift of the NI transition towards lower temperatures with respect to the pure LC system (black line) is evident; in addition, for the maximum concentration  $c = 0.5\%$ , the smectic phase become unstable, to the point that it is not observed at any temperature, at least in the range explored, as can be seen from the radial correlation function  $g(r)^{MM}$  and from the correlation along the director  $g_z(r)^{MM}$  (see Figure 4.9). In general, the main effect of adding spherical NP seems to be to disfavour the positional as well the orientational ordering.

However, the resulting phase structuring is difficult to anticipate and it is instructive to get an idea of the molecular organization by examining snapshots of the low-temperature system configurations. In Figures 4.10, 4.11, 4.12 typical configuration snapshots for the temperatures corresponding to

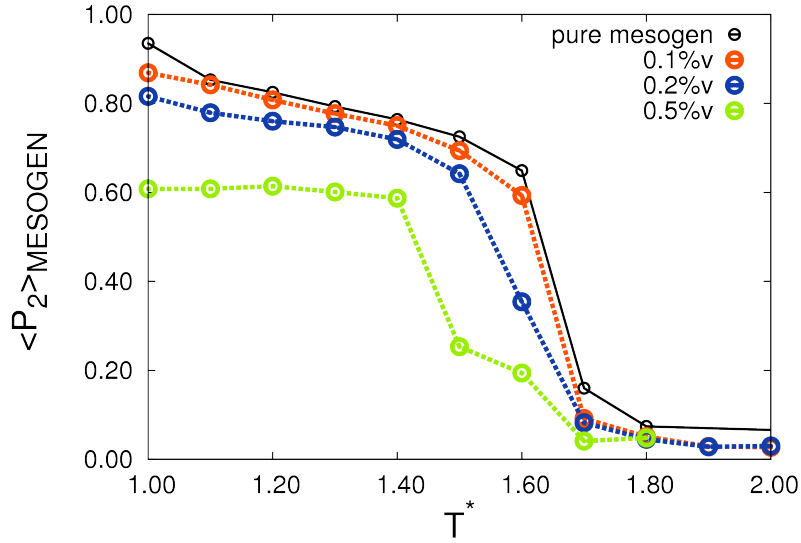


Figure 4.8: Orientational order parameter  $P_2$  (top) for the NPT simulation at  $P^* = 8$ , against the dimensionless temperature  $T^*$  of the three LC/spherical NP mixtures, as increasing concentrations; the data for the pure system are reported here for comparison.

isotropic, nematic and smectic phases are given for increasing concentrations. Here, the NPs are rendered with gray spheres while, as before, LC molecules are represented with ellipsoidal particles and their orientation is indicated by a colour code ranging from yellow to blue.

It is relevant to note that, for the smaller concentration ( $c = 0.1\%$ ), NPs are well dispersed through the LC medium, while for higher concentrations they tend to dimerize ( $c = 0.2\%$ ) or form small chains ( $c = 0.5\%$ ). This is confirmed by the radial correlation functions  $g(r)^{NN}$  of NN pairs in Figure 4.13. In fact, for  $c = 0.2\%$  the first peak at  $r^* = 6$ , which is the diameter of the spherical NP, signals that a certain number of NPs are in close contact (i.e. are first neighbours); for  $c = 0.5\%$  a rise in the magnitude of the first peak, as well as the appearance of a peak on the second coordination shell, are observed.

A longitudinal section of a MC configuration (Figure 4.14) shows the local arrangement of mesogens around one nanoparticle and evidences a



planar-type anchoring as well as the presence of defects. A qualitative information about the local arrangement can also be gained by examining the radial correlation function for nanoparticle–mesogen  $g(r)^{NM}$  pairs as shown in Figure 4.15: for all the concentrations studied the first broad peak at  $r^* = 3.6$ , corresponding to a *side–side* nanoparticle–mesogen configuration, demonstrates a clear parallel anchoring.

In addition to structural informations we have also tried to characterize the fluidity of the systems monitoring the mean square displacement of centers of mass (MSD) of the constituents. Figure 4.16 reports the MSD for both LC and nanoparticles (magnified in the inset) for the system at  $c = 0.5\%$ , showing a decrease in the mobility on cooling down sequences. As expected, the translational motion depends on the particle radius, with smaller particles diffusing more rapidly.

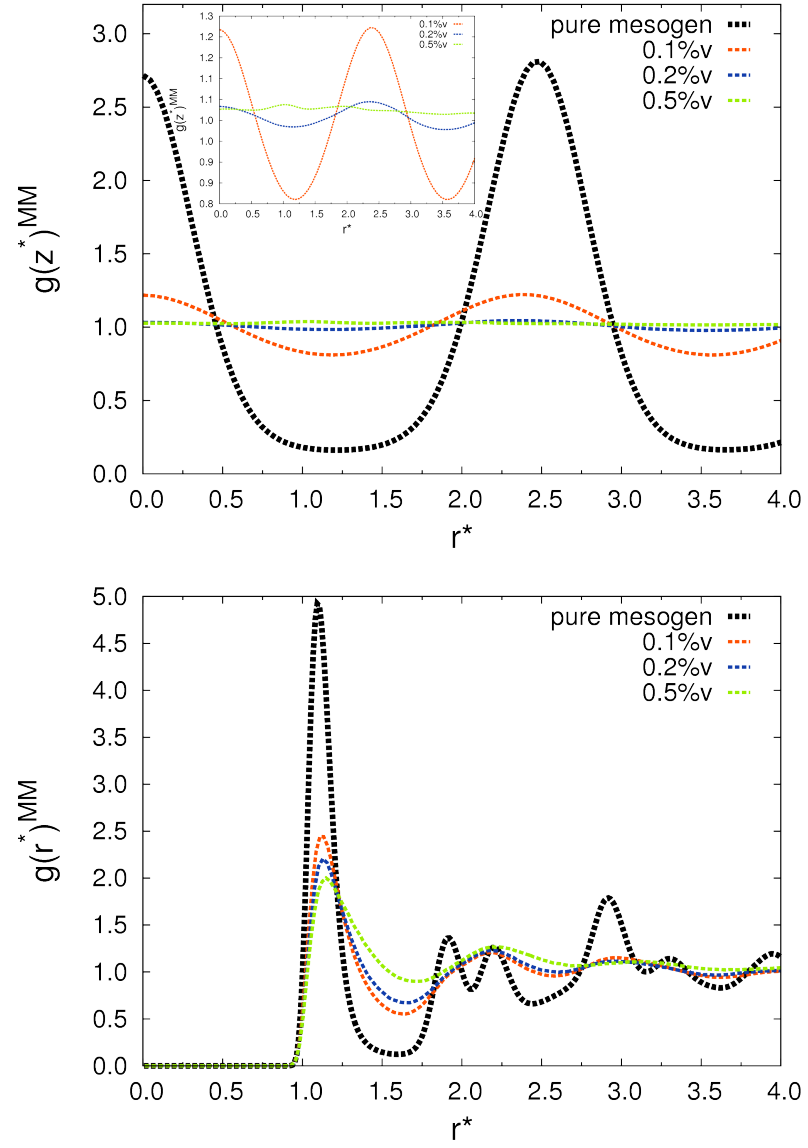


Figure 4.9: Radial correlation function and density correlation function along the director referred to M particles ( $T^* = 1.0$ ). The curves in black report the behaviour of the pure LC system.

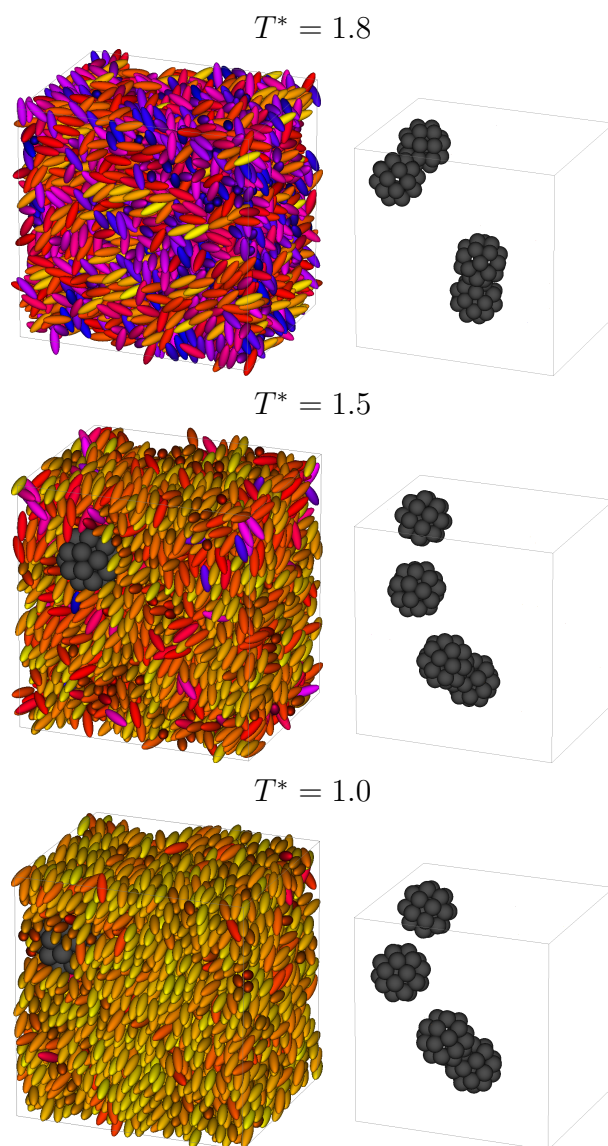


Figure 4.10: Molecular organizations of systems for  $T^* = 1.8$  (Iso),  $T^* = 1.5$  (Nem) and  $T^* = 1.0$  (SmA) phase (concentration is  $c = 0.1\%v$ ).

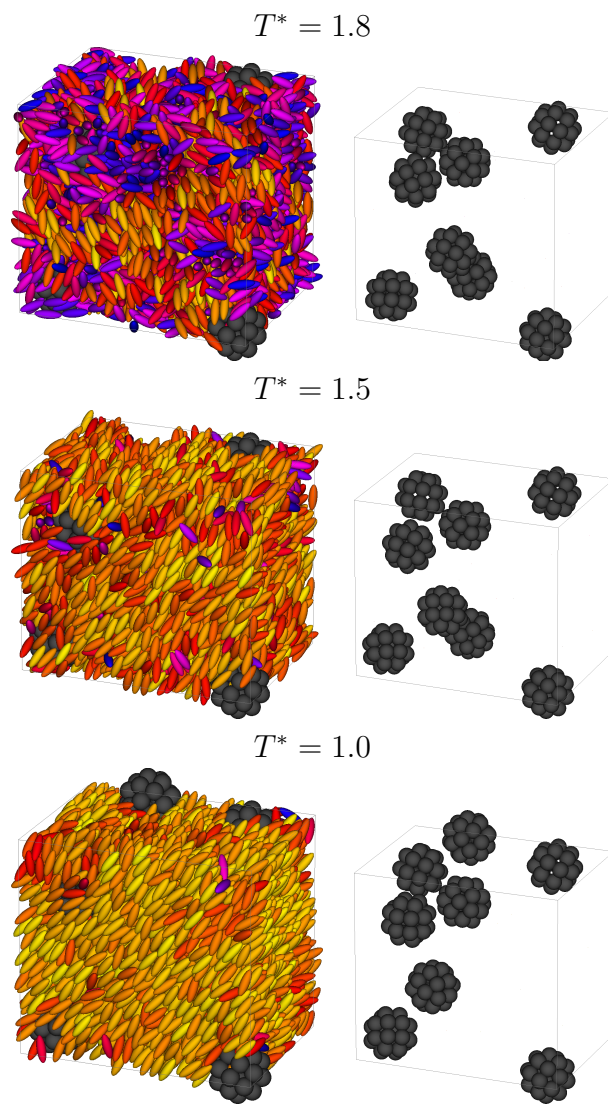


Figure 4.11: Molecular organizations of systems for  $T^* = 1.8$  (Iso),  $T^* = 1.5$  (Nem) and  $T^* = 1.0$  (SmA) phase (concentration is  $c = 0.2\%v$ ).

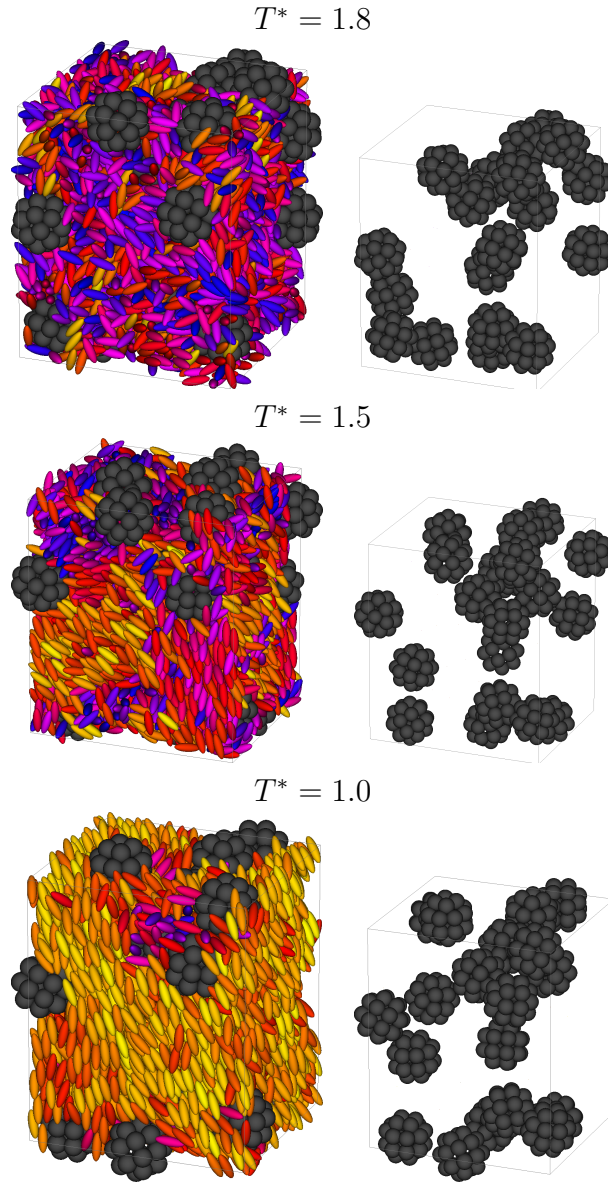


Figure 4.12: Molecular organizations of systems for  $T^* = 1.8$  (Iso),  $T^* = 1.5$  (Nem) and  $T^* = 1.0$  (Nem) phase (concentration is  $c = 0.5\%v$ ).

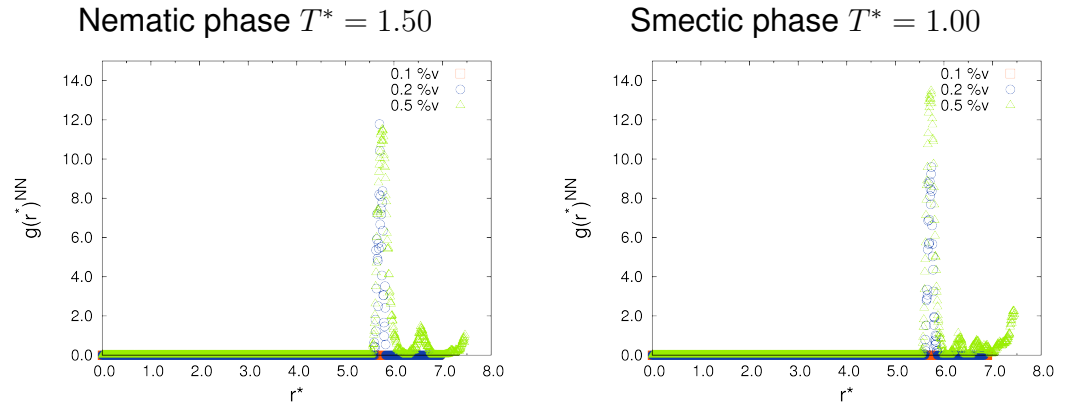


Figure 4.13: Radial correlation function referred to NPs for  $c = 0.1\%$ ,  $0.2\%$  and  $0.5\%$  for two reference temperatures in smectic ( $T^* = 1.0$ ) and nematic ( $T^* = 1.5$ ) phase.

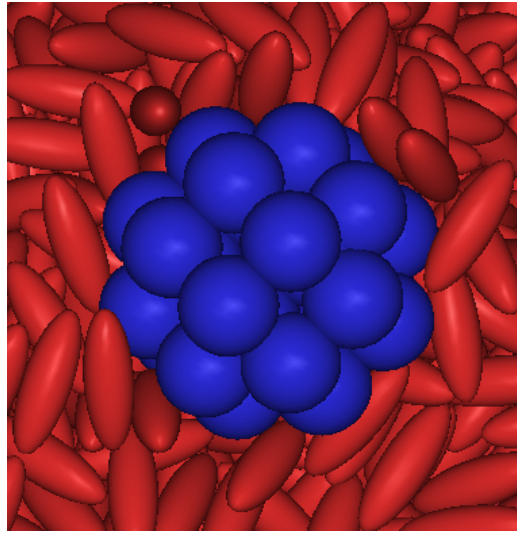


Figure 4.14: Longitudinal section of a portion of an instantaneous configuration at  $T^* = 1.5$  ;  $c = 0.1\%$  showing a parallel weak anchoring.

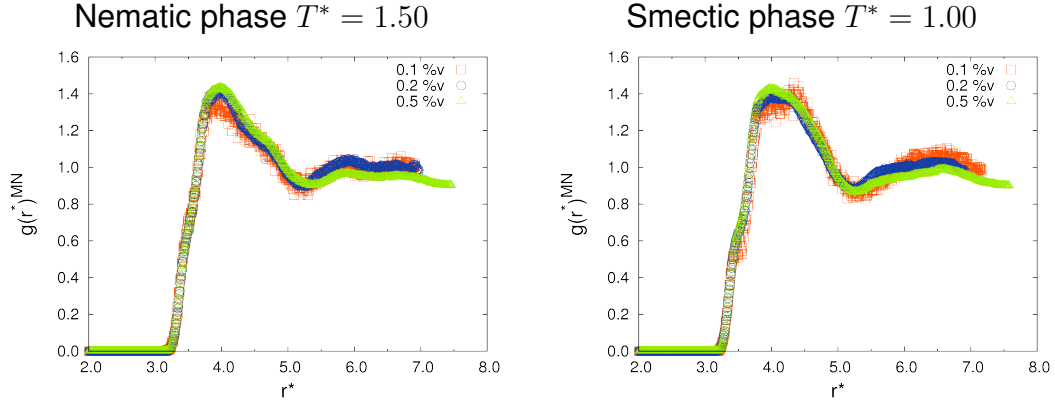


Figure 4.15: Mesogen-nanoparticle  $g(r)^{MN}$  correlation functions at  $T^* = 1.5$  and  $T^* = 1.0$  for nanoparticles concentrations 0.1%, 0.2% and 0.5%.

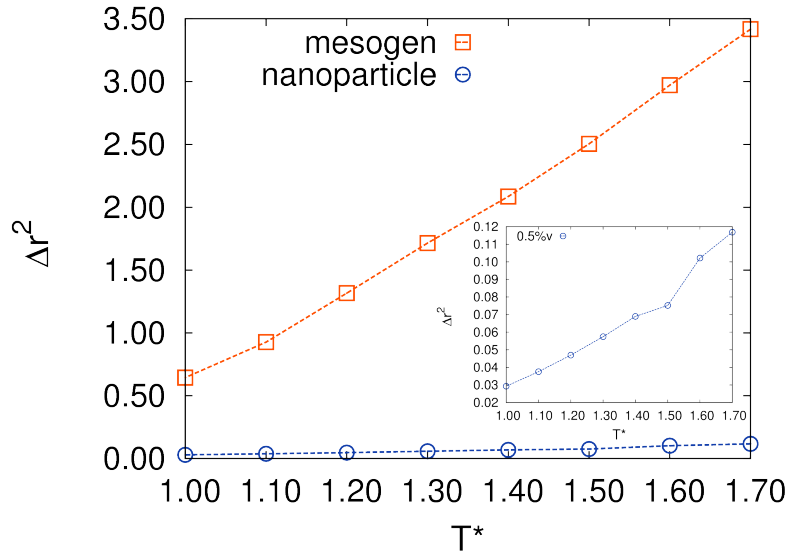


Figure 4.16: Total mean square displacement ( $\sigma_0$  units) plotted against temperature, both for mesogens and nanoparticles (see inset for the nanoparticle expanded curve), calculated after 10 kcycles.

### 4.2.2 Rod-shaped Nanoparticle

Rod-shaped nanoparticles are modelled as close-packed bulk clusters of 14 equal Lennard-Jones sites, which can be viewed as a stacking of three square basis layers (each containing 4 LJ sites), with one single LJ unit at both ends (see Figure 4.17). As in the case of spherical NPs, LJ spheres are characterized by energetic well depths  $\varepsilon_S = \varepsilon_x = \varepsilon_y = \varepsilon_z = 0.15\varepsilon_0$ , and dimensions  $\sigma_S = \sigma_x = \sigma_y = \sigma_z = 2.0\sigma_0$ . Spheres are slightly overlapping, so that the long and the short axis of the overall nanoparticle are about  $8\sigma_0$  and  $3.2\sigma_0$  respectively (Figure 4.18).

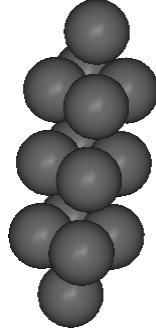


Figure 4.17: Exploded view of the rod-shaped nanoparticle.

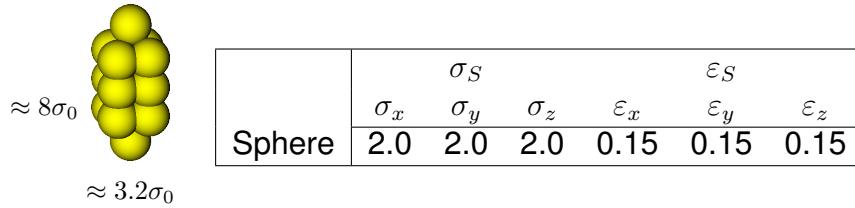


Figure 4.18

In fig 4.19 the representative pair potential profiles relative to the homogeneous interaction NN, as well as the heterogeneous NM are shown. Focusing on the NN interaction profiles, we evidence that the lateral ss interaction is 4 times larger than the T one, and more than 10 times larger of the ee interaction. On the other hand, the NM interaction relative to lateral (ss) configuration is much larger than both the terminal (ee) and T interactions.



This picture suggests the promotion of the parallel-type anchoring, that is again energetically favored with respect to the perpendicular one. The potential cutoff radius was chosen as  $r_c^{*(GB)} = 4.0$  and  $r_c^{*(LJ)} = 6$  respectively for the mesogen–mesogen and the interaction between spherical sites, while the cutoff interaction for the mixed interaction is calculated through the mixing rules adopted in [77].

As in the case of spherical nanoparticles, we performed MC simulations of sample mixtures of  $N = N_M + N_N = 4000$  total particles (with  $N_N = 4, 8, 20$  corresponding respectively to the nanoparticles concentration  $c = 0.1\%, 0.2\%, 0.5\%$ ) in the isobaric–isothermal ensemble, using 3D periodic conditions. Dimensionless pressure  $P^*$  was set to 8 while the temperature  $T^*$  spanned the range 1.0–1.8. Figure 4.20 show the temperature dependence of the orientational order parameter.

This plots reveal that, for any concentration value, the system undergoes a shift of the NI transition towards lower temperatures with respect to the pure LC system (black line); this is particularly strong for the  $c=0.5\%$ . Focusing on the low temperatures, differently from the previous case of spherical embedded NP case, smectic A phase survives irrespective of concentration, as confirmed by both radial correlation function  $g(r)^{MM}$  and correlation along the director  $g(z)^{MM}$  (see Figure 4.21).

Snapshots of molecular configuration in Sm and Nem phase give some hints on the spatial arrangement of nanoparticles. Here at the smaller concentration ( $c=0.1\%$  and  $0.2\%$ ) NPs seems to be dispersed through the mesogenic solvent, while for  $c=0.5\%$  they tend to dimerize. This is proved also by the  $g(r)^{NN}$  curve at  $c=0.5\%$  for  $T^* = 1.0$  showing a peak at  $r^* = 3.0$ , that is the contact distance for NN pairs in *side-side* configuration as well a structure of peaks at larger distance. No evidence of orientational order of nanoparticles is found for any value of the concentration (see Figure 4.20). Focusing on the local arrangement between NM pairs, the radial correlation function for nanoparticle–mesogen  $g(r)^{NM}$  in smectic ( $T^* = 1.0$ ) phase (Figure 4.27) shows, for all the concentration values, a first small peak at

$r^* = 2.5$ , corresponding to nanoparticle–mesogen in *side-side* configuration, and a second broad and more pronounced peak around  $r^* = 4.0$ ; at larger distance, that is far from the NP surface, the correlation function tends to a constant value, especially in the nematic phase. This picture fits with a weak parallel anchoring as evidenced in Figure 4.26 by a longitudinal section of a MC configuration showing the local arrangement of mesogens around the NP surface with formation of LC orientational defects.

We also investigate the mobility of the system, computing the mean square displacement of centers of mass (MSD) of both nanoparticles and mesogens; the behavior of the MSD for both LC and nanoparticles are reported in Figure 4.28, confirming the same trend observed in the previous simulations.

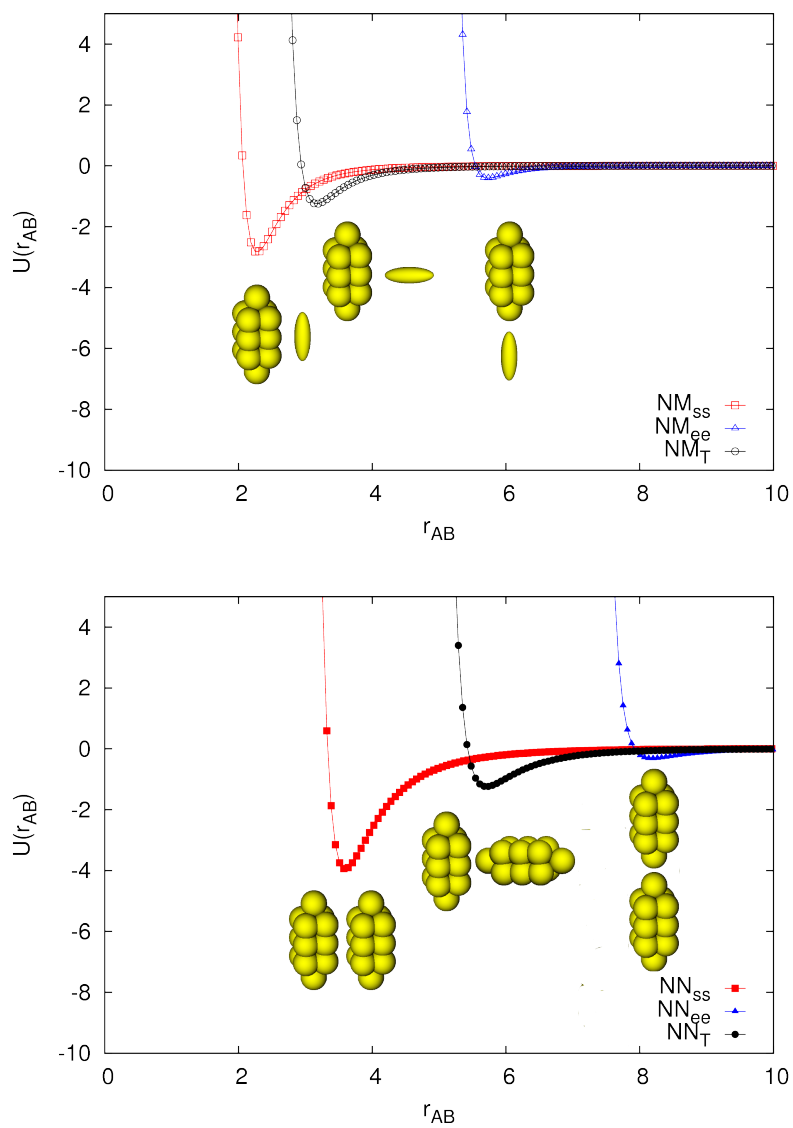


Figure 4.19: Pair potential profiles relative to homogeneous NN (bottom) and heterogeneous NM (top) for pairs in  $ss$ ,  $ee$ ,  $T$  configuration.

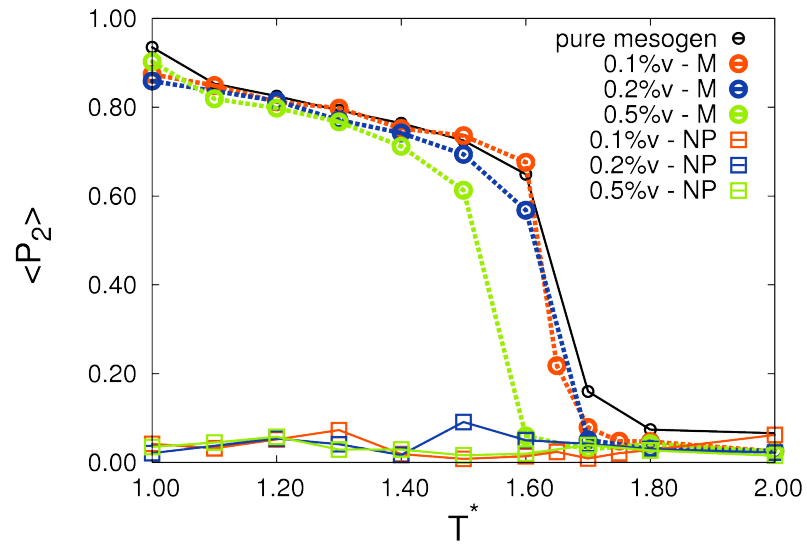


Figure 4.20: Orientational order parameter  $P_2$  for the NPT simulation at  $P^* = 8$ , against the dimensionless temperature  $T^*$  of the mixtures of LC and NP; the data for the pure system are reported here for comparison. The orientational order parameter for rod-like nanoparticles is also reported.

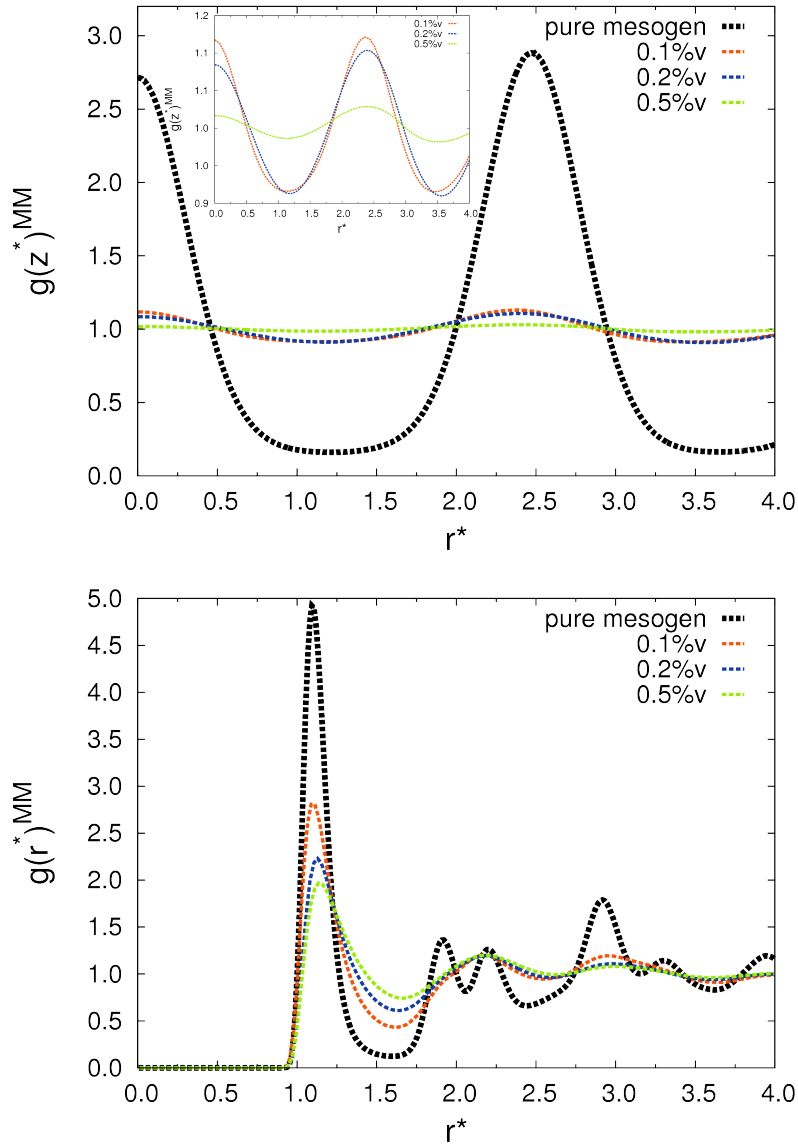


Figure 4.21: Radial correlation function (bottom) and density correlation function (top) along the director referred to M particles for  $c = 0.5\%$  for two reference temperatures in smectic ( $T^* = 1.0$ ) and nematic ( $T^* = 1.5$ ) phase. The curves in black report the behaviour of the pure LC system.

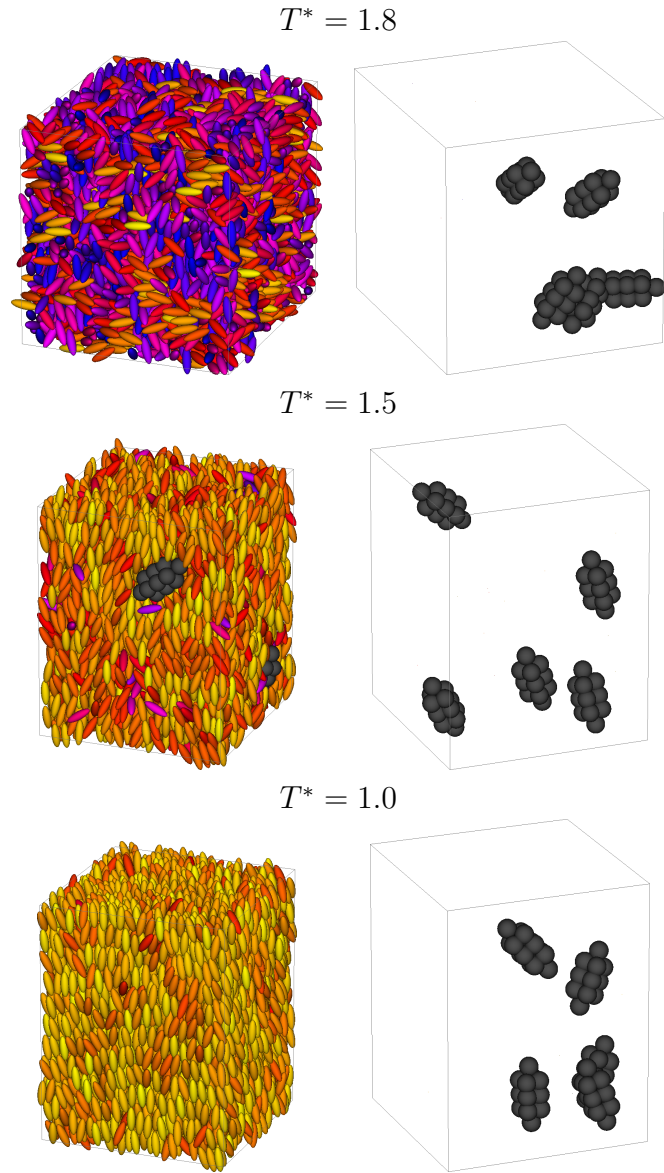


Figure 4.22: Molecular organizations of systems for  $T^* = 1.8$  (Iso),  $T^* = 1.5$  (Nem) and  $T^* = 1.0$  (SmA) phase (concentration is  $c = 0.1\%$ ).

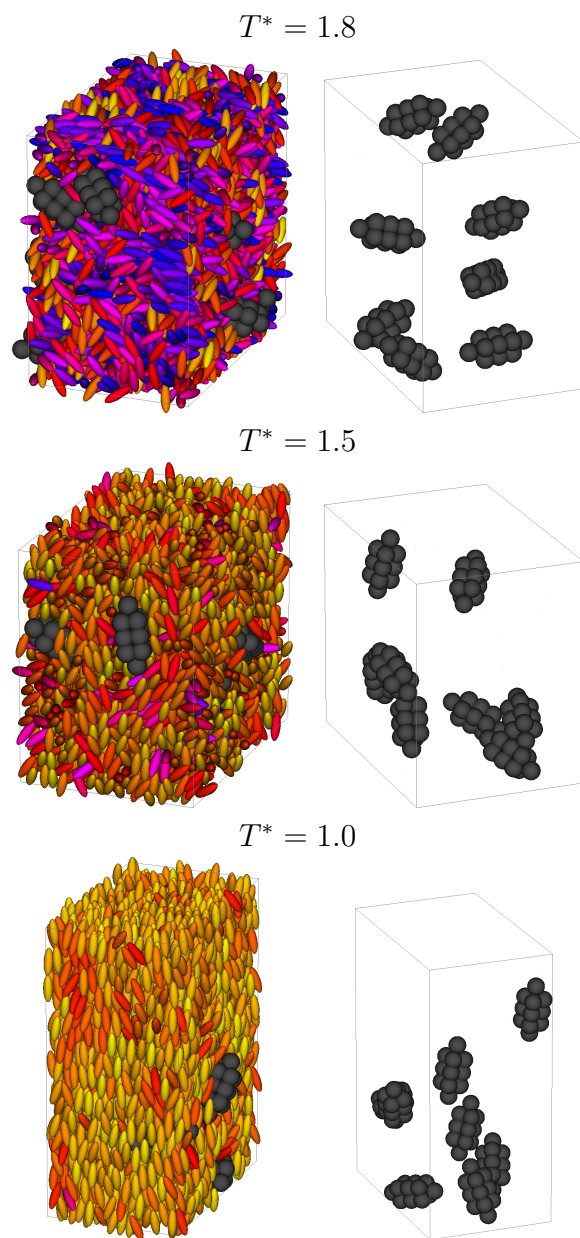


Figure 4.23: Molecular organizations of systems for  $T^* = 1.8$  (Iso),  $T^* = 1.5$  (Nem) and  $T^* = 1.0$  (SmA) phase (concentration is  $c = 0.2\%$ ).

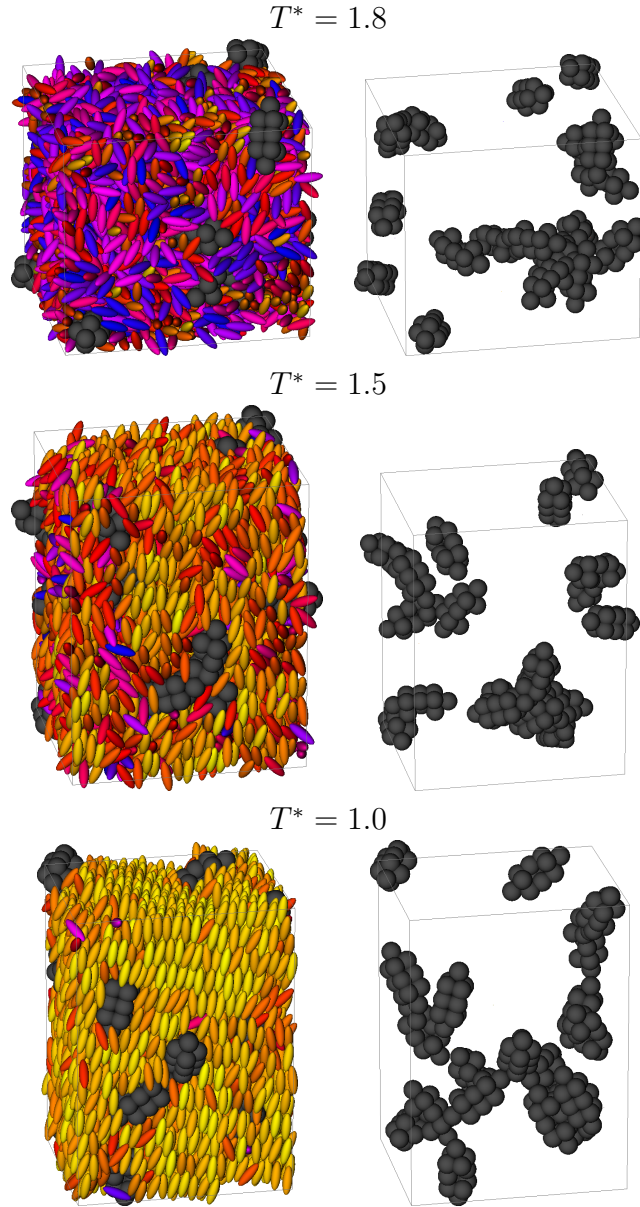


Figure 4.24: Molecular organizations of systems for  $T^* = 1.8$  (Iso),  $T^* = 1.5$  (Nem) and  $T^* = 1.0$  (SmA) phase (concentration is  $c = 0.5\%$ ).



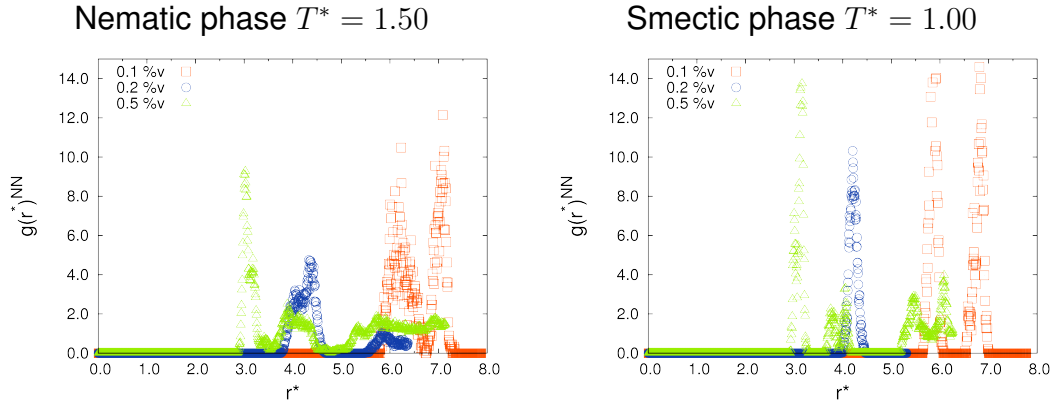


Figure 4.25: Radial correlation function and density correlation function along the director referred to NN particles for  $c=0.1\%$ ,  $0.2\%$  and  $0.5\%$  for two reference temperatures in smectic ( $T^* = 1.0$ ) and nematic ( $T^* = 1.5$ ) phase.

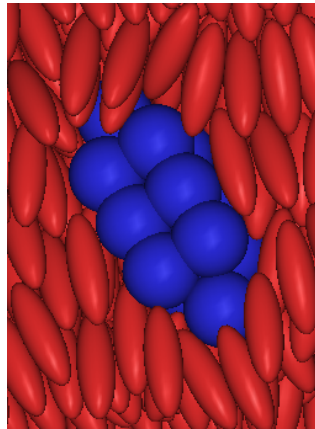


Figure 4.26: Longitudinal section of a portion of an instantaneous configuration at  $T^* = 1.5$ ,  $c = 0.1\%$  showing a parallel anchoring.

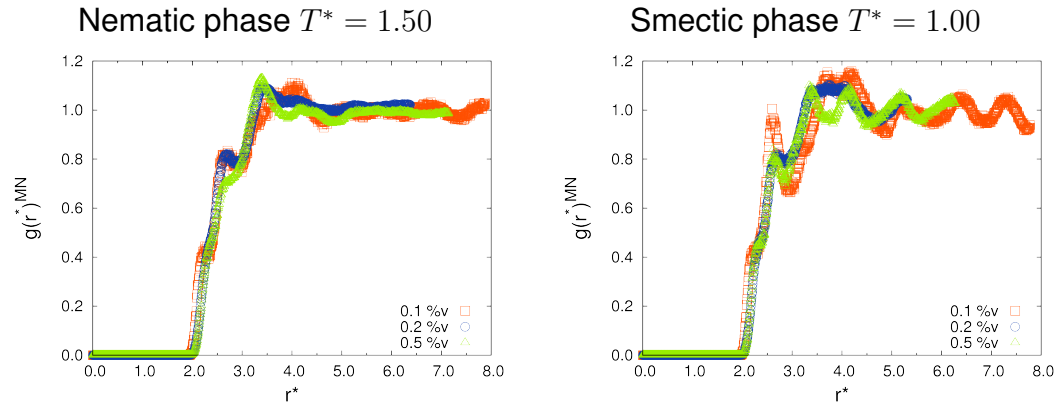


Figure 4.27: Mesogen–nanoparticle  $g(r)^{MN}$  correlation functions at  $T^* = 1.0$  for different nanoparticles concentrations (system  $\varepsilon_S = 0.15$  and  $e_{GBLJ} = 2.0$ ).

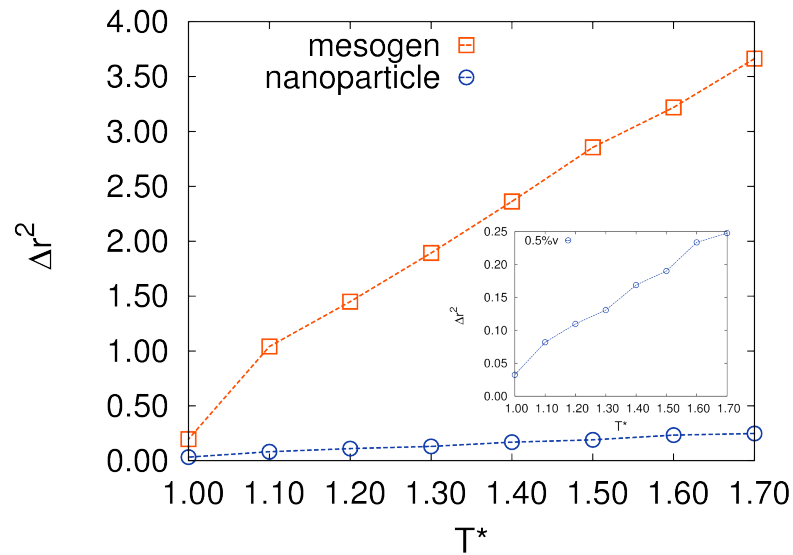
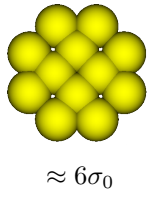


Figure 4.28: Comparison of the mean square displacement plotted against temperature for the mesogen and the nanoparticle (see inset for the nanoparticle expanded curve).

### 4.2.3 Disk-shaped Nanoparticle

Disk-shaped nanoparticles are modelled as clusters of 12 equal Lennard–Jones sites which are placed on a dense octagonal basis layer. As in the case of spherical NPs, LJ spheres are characterized by energetic well depths  $\varepsilon_S = \varepsilon_x = \varepsilon_y = \varepsilon_z = 0.15\sigma_0$  dimensions  $\sigma_S = \sigma_x = \sigma_y = \sigma_z = 2.0\sigma_0$ . Spheres are slightly overlapping, so that the long and the short axis of the overall nanoparticle are about  $6\sigma_0$  and  $2\sigma_0$  respectively.



	$\sigma_S$			$\varepsilon_S$		
	$\sigma_x$	$\sigma_y$	$\sigma_z$	$\varepsilon_x$	$\varepsilon_y$	$\varepsilon_z$
Sphere	2.0	2.0	2.0	0.15	0.15	0.15

Figure 4.29

In Figure 4.30 the representative pair potential profiles relative to the homogeneous interaction NN, as well as the heterogeneous NM are shown. Focusing on the NN interaction profiles, we evidence that the *side-side* interaction at  $r^* \approx 6.0$  is 3 times smaller than the *T* one ( $r^* \approx 4.0$ ), and more than 10 times smaller of the *face-face* interaction ( $r^* \approx 2.0$ ). On the other hand, the NM interaction relative to *T* configuration (at  $r^* = 1.5$ ) is much larger than both the *face-to-end* (at  $r^* = 2.5$ ) and *side-to side* ( $r^* = 3.5$ ) interactions. This picture suggests the promotion of the parallel-type anchoring, that also in this case is energetically favored with respect to the perpendicular one. The potential cutoff radius  $r_c^{*(GB)} = 4.0$  and  $r_c^{*(LJ)} = 6$  respectively for the mesogen–mesogen and the interaction between spherical sites, while the cutoff interaction for the mixed interaction is calculated through the mixing rules adopted in [77].

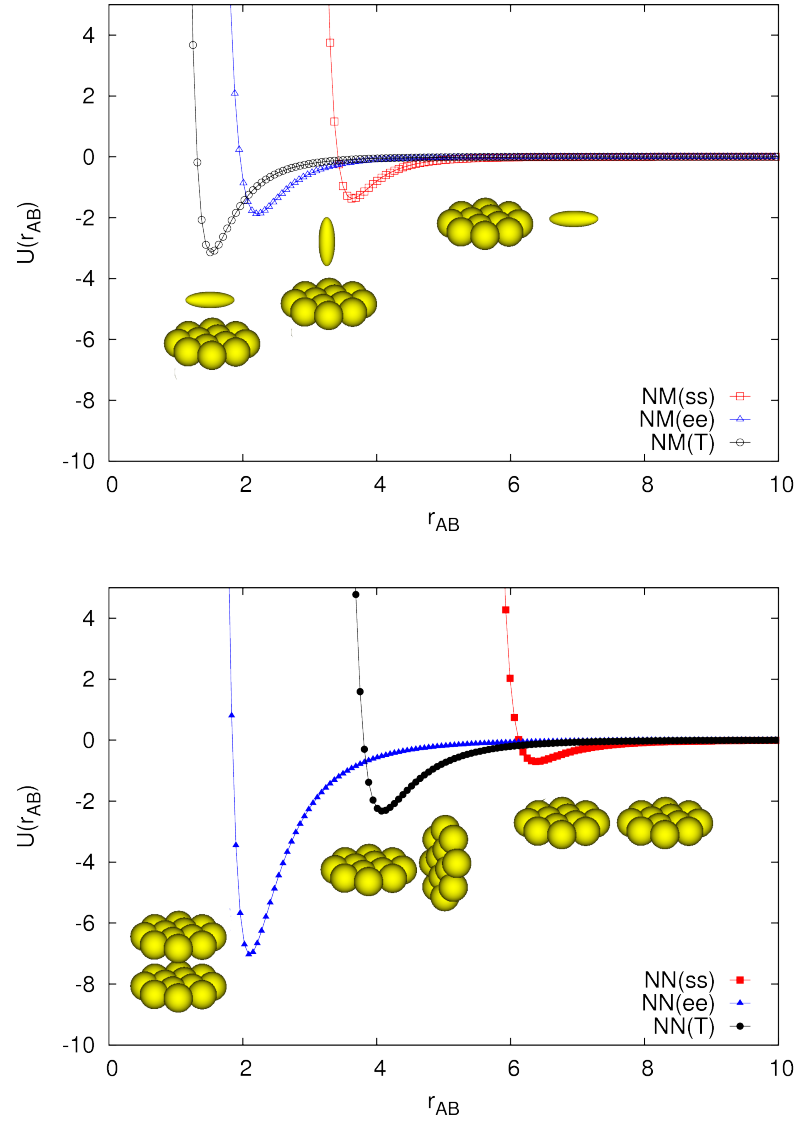


Figure 4.30: Potential profiles relative to both homogeneous disk-like nanoparticle–nanoparticle (NN) and heterogenous nanoparticle–mesogen NM interaction for pairs in side-to-side, T-shape, and end-to-end configurations. The distance is plotted in  $\sigma_0$  units whilst the potential in  $\varepsilon_0$  units.

MC simulations of sample mixtures of  $N = N_M + N_N = 4000$  total particles (with  $N_N = 4, 8, 20$  corresponds respectively to the nanoparticles concentration 0.1%, 0.2%, 0.5%) were performed in the isobaric–isothermal ensemble, using 3D periodic boundary conditions. Dimensionless pressure  $P^*$  was set to 8 while the temperature  $T^*$  spanned the range 1.0–1.8.

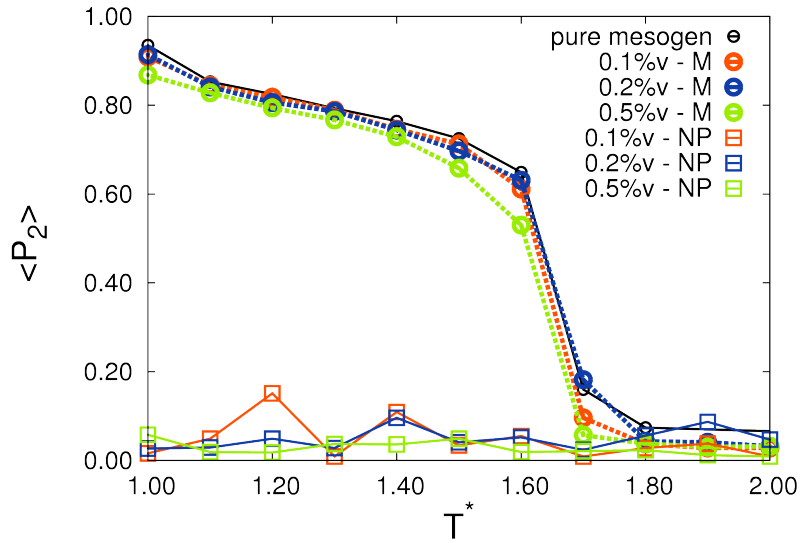


Figure 4.31: LC orientational order parameter  $\langle P_2 \rangle$  for the NPT simulation at  $P^* = 8$ , against the dimensionless temperature  $T^*$  of the three mixtures of LC and NP, at increasing concentrations. The global orientational order parameter relative to disk-like nanoparticles is also reported.

The temperature dependence of the LC orientational order parameter and of the adimensional number density shows the same phase sequence Iso–Nem–Sm of the pure LC (see Figure 4.31); if the concentrations of discotic NP is less or equal to  $c=0.2\%$  a strong layering in the density correlation along the director ( $g(z)^{MM}$ ) and the characteristic double peak typical of an hexagonal arrangement in the radial correlation function  $g(r)^{MM}$  (see Figure 4.35) confirm the presence of a SmB phase, suppressed for  $c=0.5\%$ . Differently from the previous case of spherical and elongated NP, no shift of the NI temperature transition is observed. Still, no evidence of orientational order of nanoparticles is found for any value of the concentration  $c$

(see Figure 4.31).

Concerning the NPs organization, for the smallest concentration ( $c=0.1\%$ ), NPs are well dispersed through the mesogenic media, while for larger concentrations they tend to dimerize and to form larger aggregates. This could be observed also from the  $g(r)^{NN}$  reported in Figure 4.36 curves at  $c=0.5\%$  for both  $T^* = 1.0$  and  $T^* = 1.5$  showing a peak at  $r^* = 2$ , that is the contact distance for NN pairs in face-to-face configuration as well as a structure of peaks at larger distance.

Focusing on the local arrangement between nanoparticles and mesogens, the radial correlation function  $g(r)^{NM}$  in smectic ( $T^* = 1.0$ ) phase (Figure 4.38) shows, for all the concentration values, a first small peak at  $r^* = 2.$ , corresponding to nanoparticle-mesogen pairs in T configuration, a second broad and more pronounced peak around  $r^* = 4.0$  which is consistent with nanoparticle-mesogen pairs in *side-side* configuration; at larger distance, that is far from the NP surface, the correlation function tends to a constant value, especially in the nematic phase. This picture fits with weak planar anchoring situation (see Figure 4.37).

The mobility of the system, computed via the MSD of both nanoparticles and mesogens, is investigated and reported in Figure 4.39.

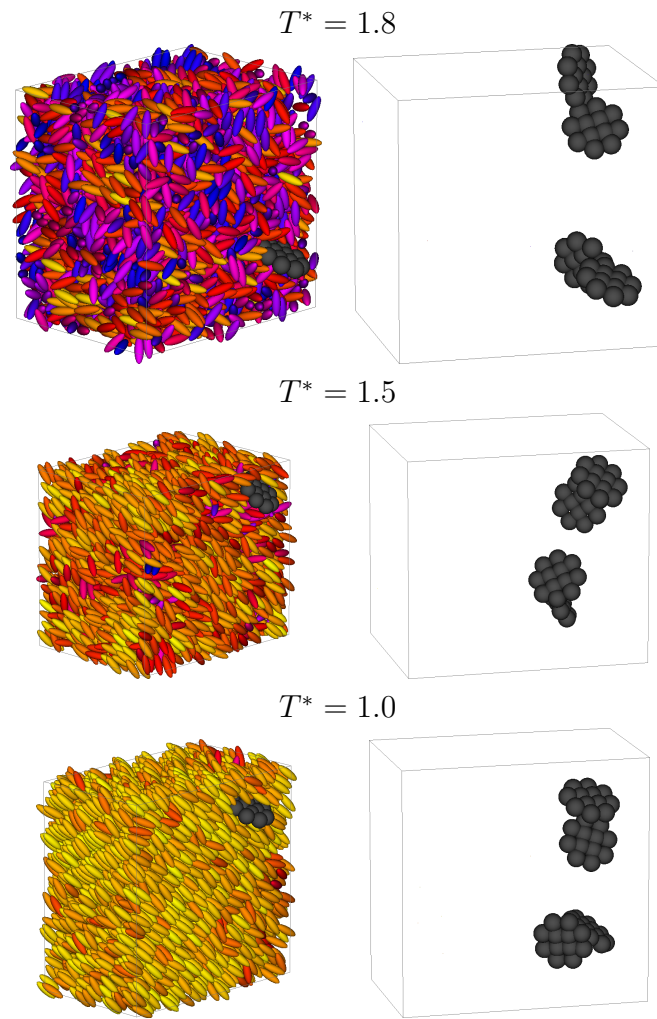


Figure 4.32: Snapshot of instantaneous configurations showing the molecular organization at temperatures  $T^* = 1.0, 1.5, 1.8$  at concentration  $c = 0.1\%$ .

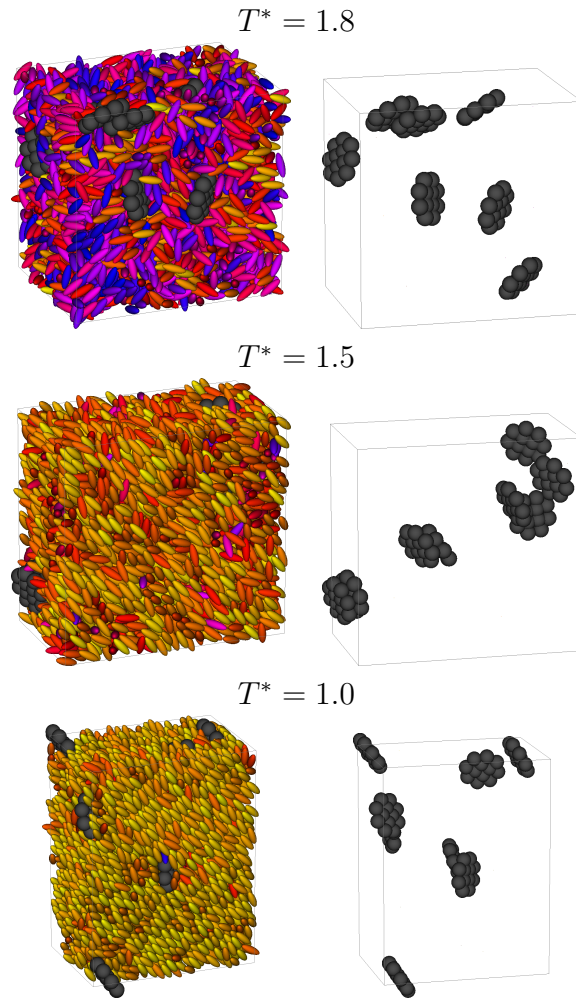


Figure 4.33: Snapshot of instantaneous configurations showing the molecular organization at temperatures  $T^* = 1.0, 1.5, 1.8$  at concentration  $c = 0.2\%$ .



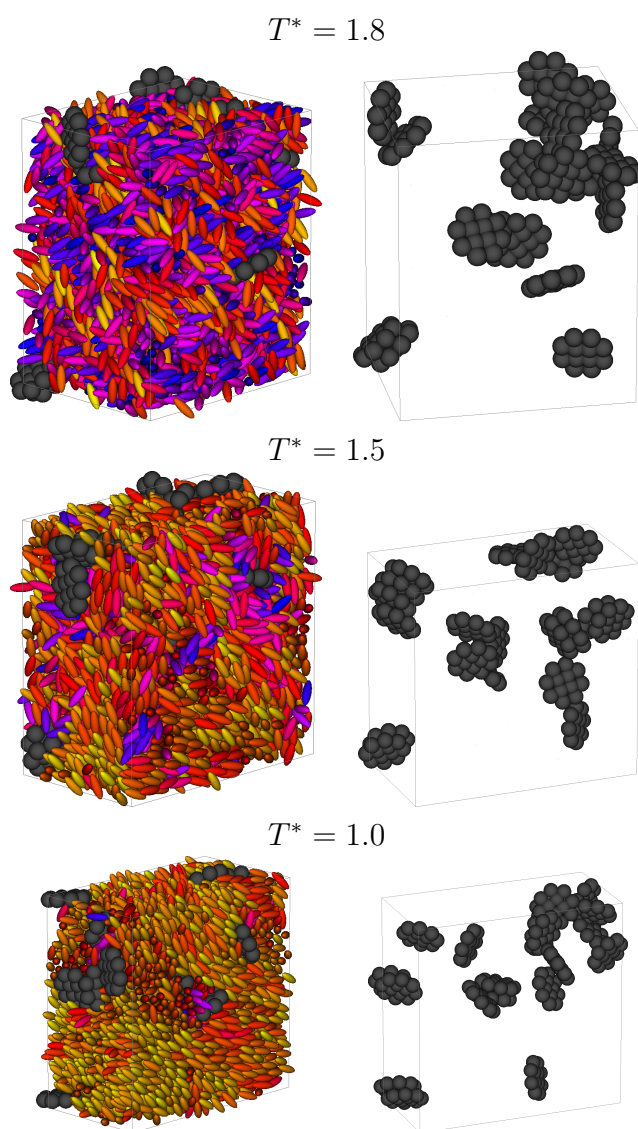


Figure 4.34: Snapshot of instantaneous configurations showing the molecular organization at temperatures  $T^* = 1.0, 1.5, 1.8$  at concentration  $c = 0.5\%$ .

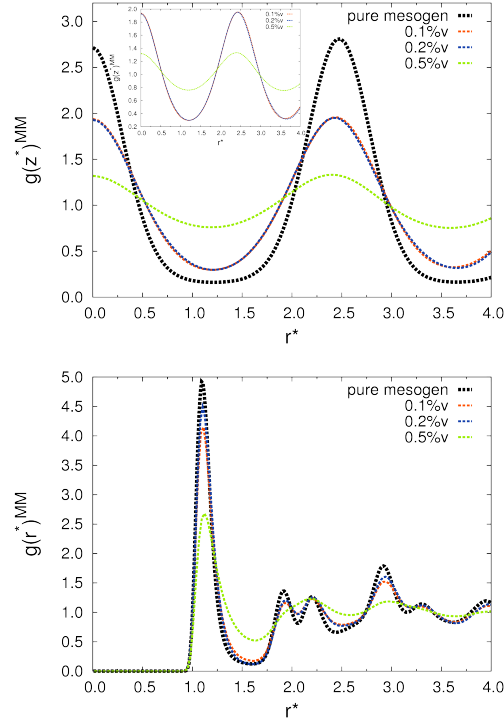


Figure 4.35: Radial correlation function and density correlation function along the director referred to M particles for  $c = 0.1\%$ ,  $0.2\%$ ,  $0.5\%$  for temperature reference in smectic ( $T^* = 1.0$ ) phase. The curves in black report the behaviour of the pure LC system.

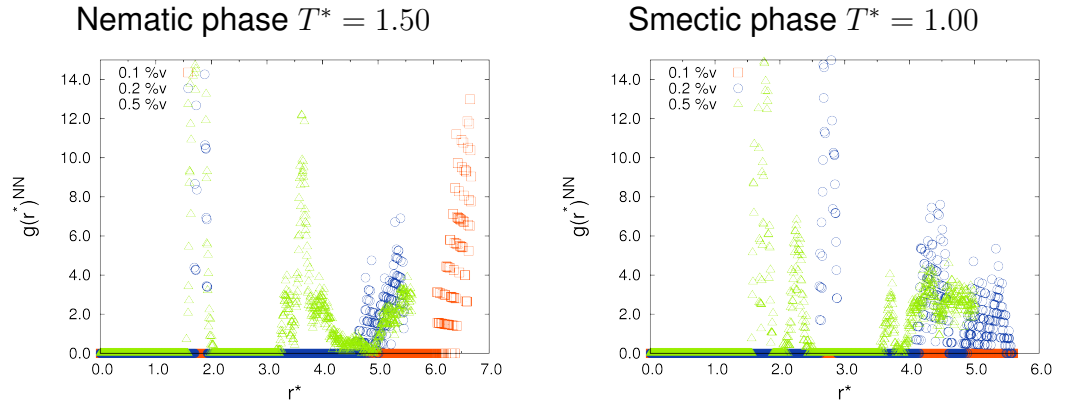


Figure 4.36: Radial correlation function  $g(r)^{NN}$  referred to NN particles for  $c = 0.5\%$  for two reference temperatures in smectic ( $T^* = 1.0$ ) and nematic ( $T^* = 1.5$ ) phase.

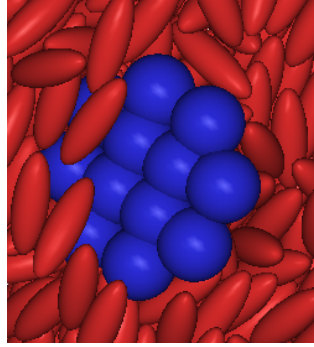


Figure 4.37: Longitudinal section of a portion of a MC configuration showing a nanoparticle embedded in a nematic LC ( $T^* = 1.5$  ;  $c = 0.1\%$ ). A parallel weak anchoring is evident.

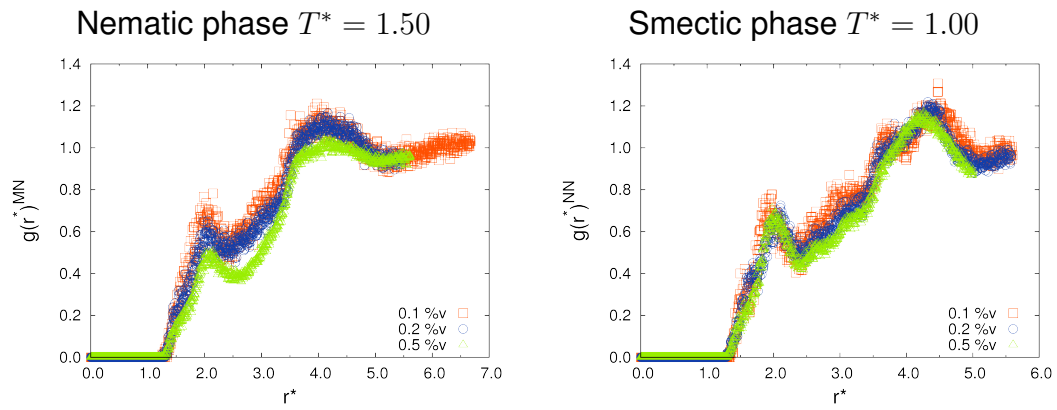


Figure 4.38: Mesogen–nanoparticle  $g(r)^{MN}$  correlation functions at  $T^* = 1.0$  for concentrations  $c = 0.1\%$ ,  $0.2\%$ ,  $0.5\%$ .

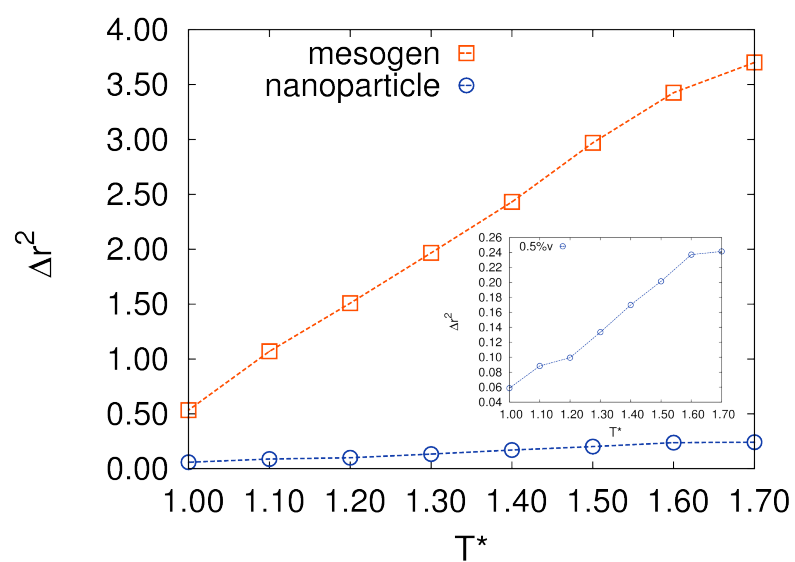


Figure 4.39: Comparison of the mean square displacement plotted against temperature, calculated after 10 kcycles for both mesogens and nanoparticles at  $c = 0.5\%$  (see inset for the nanoparticle expanded curve).

#### 4.2.4 Conclusions

In conclusion, we have shown that doping a mesogenic system with nanoparticles, at least for the chosen values of the well depth ( $\varepsilon_S = 0.15$ ) and the coupling parameter ( $e_{NM} = 2.0$ ), has the effect of reducing both the orientational and positional order, irrespective from the NPs shape (spherical, prolate, oblate). Nevertheless, the most disordering effects are found in the case of spherical nanoparticles, for which the disruption of the mesogenic orientational order is more important. For any shape, the larger the concentration of NP is, the bigger becomes the potential to destroy the long-range positional as well as orientational order.

In order to compare results for the translational motion of NPs of different shapes we take into account the MSD against MC cycles: from the slope of MSD at long time (see Figure 4.40) we could extract the self-diffusion coefficient  $D_t$ .

We report in table 4.1 the  $D_t$  coefficients for the three different NPs shapes at  $c=0.5\%$ , obtained applying equation 3.30. In Figure 4.41 are shown the trends of  $D_t$  against the  $T^*$  for the reference temperatures corresponding to isotropic, nematic and smectic phases. Here we note that disc-like NPs have higher mobility, followed by rods, although with very small differences, while the spheres diffuse considerably less. This trend suggests that the determinant factor enhancing NP mobilities is given by their minimum cross section (6 for spheres, 3.2 for rods and 2 for discs).

	Spherical NPs		Rod-like NPs		Disk-like NPs	
	$\Delta r^2$	$D_t$	$\Delta r^2$	$D_t$	$\Delta r^2$	$D_t$
Isotropic phase	0.115	0.0019	33.3	0.0055	32.46	0.0051
Nematic phase	0.074	0.0012	52.6	0.0032	50.0	0.0033
Smectic phase	0.029	0.0005	303.0	0.0005	172.4	0.0009

Table 4.1

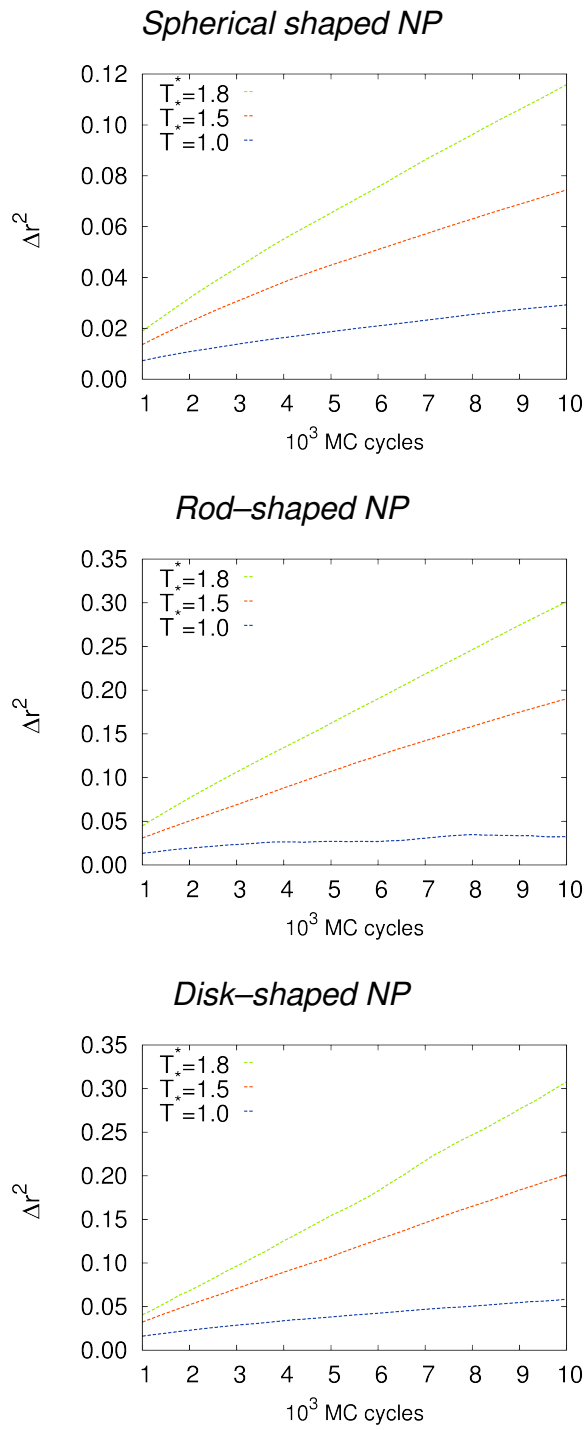


Figure 4.40: Average mean square displacements vs MC cycles for three temperature cases for the systems with spherical, rod and disk-shaped nanoparticles.

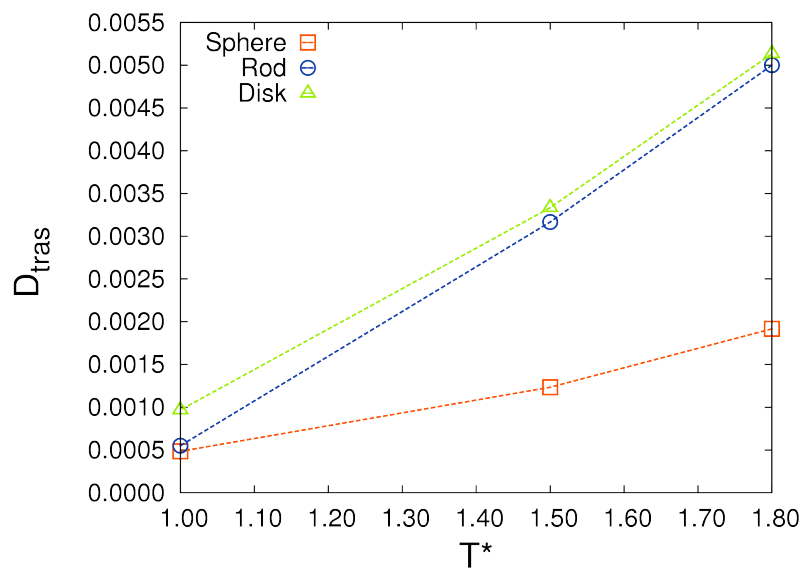


Figure 4.41: Comparison between the translational diffusion coefficient against temperature for the three different NPs shape.

### 4.3 Effect of NPs size

In order to evaluate the effect of the size of dopant NP on the mesophase organization and orientational order of system of rod mesogens, we compared the previous results for disk-shaped NPs with a new series obtained considering dopant NPs with same shape and energetic parameters, but enlarged size.

We modelled this larger disk-shaped nanoparticle via a multi-site model in which a ring of 14 LJ sites has been added to the scheme described in section 4.2.3. The total number of LJ sites is 28 (see Figure 4.42), while the long and the short axis of the overall nanoparticle are about  $8\sigma_0$  and  $2\sigma_0$  respectively.

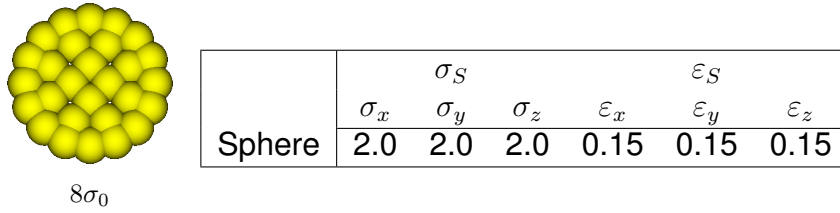


Figure 4.42

Figure 4.43 reports the pair potential profiles relative to homogeneous interaction between NN pairs and heterogeneous interaction between NM. Focusing on the NN profiles, the comparison with the plot in Figure 4.30 (in section 4.2.3) suggests that larger disks has stronger  $ee$  interaction and thus have a greater tendency to aggregate face-to face. No relevant modifications are found on the heterogeneous MN profiles.

We performed MC simulation of sample mixtures of  $N = N_M + N_N = 4000$  total particles with  $N_N = 4, 8, 20$ , as in the previous cases, in the NPT ensemble at the dimensionless pressure  $P^* = 8$  and in the same range of temperature  $1.0 < T^* < 2.0$ .

The simulation of systems doped with these discotic NPs gives a quite different behaviour of the orientational order vs  $T^*$  curve as reported in Figure 4.44. In Fact, for the largest concentration  $c=0.5\%$  the isotropic–



nematic transition temperature is significantly shifted toward lower values and, more in general, the  $\langle P_2 \rangle$  values are diminished with respect to the smaller discotic NPs case. Also the phase sequence is affected: for all concentrations  $c=0.1\%$ ,  $0.2\%$  and  $0.5\%$  the smectic phase is suppressed. This is made evident by the behaviour of radial correlation function  $g(r)^{MM}$  and density along the director  $g(z)^{MM}$  (see Figure 4.45); in particular no splitting of the second peak characteristic of an hexagonal order in the plane is found in the  $g(r)^{MM}$  for any values of nanoparticle concentration, and a lack of the smectic periodicity for  $c=0.5\%$  case is apparent even at low temperature (see  $g(z)^{MM}$ ). Revealing snapshots of configurations of the system at the selected temperature  $T^* = 1.0$ ,  $1.5$  and  $1.8$  for the three concentration cases are shown in Figure 4.46, 4.47, 4.48.

The local arrangement of mesogens around the NPs evidences weak planar-type anchoring and presence of defects. Looking at the NPs organization, as in the previous case, for the smallest concentration ( $c=0.1\%$ ) NPs stay dispersed inside the mesogenic solvent; instead at larger concentration they tend to stack face-to-face, even if no evidence of large aggregates is found. This is apparent also from the  $g(r)^{NN}$  curves at  $c=0.5\%$  for both  $T^* = 1.0$  and  $T^* = 1.5$  showing a peak at  $r^* = 2.0$ , that is the contact distance for NN pairs in face-to face configuration (see Figure 4.50).

In conclusion we have shown that increasing the size of dopant NPs, at least for the discotic-like ones, has the effect to create orientational defects, thus reducing both positional and orientational order of the LC medium and shifting downward the nematic–isotropic transition temperatures.

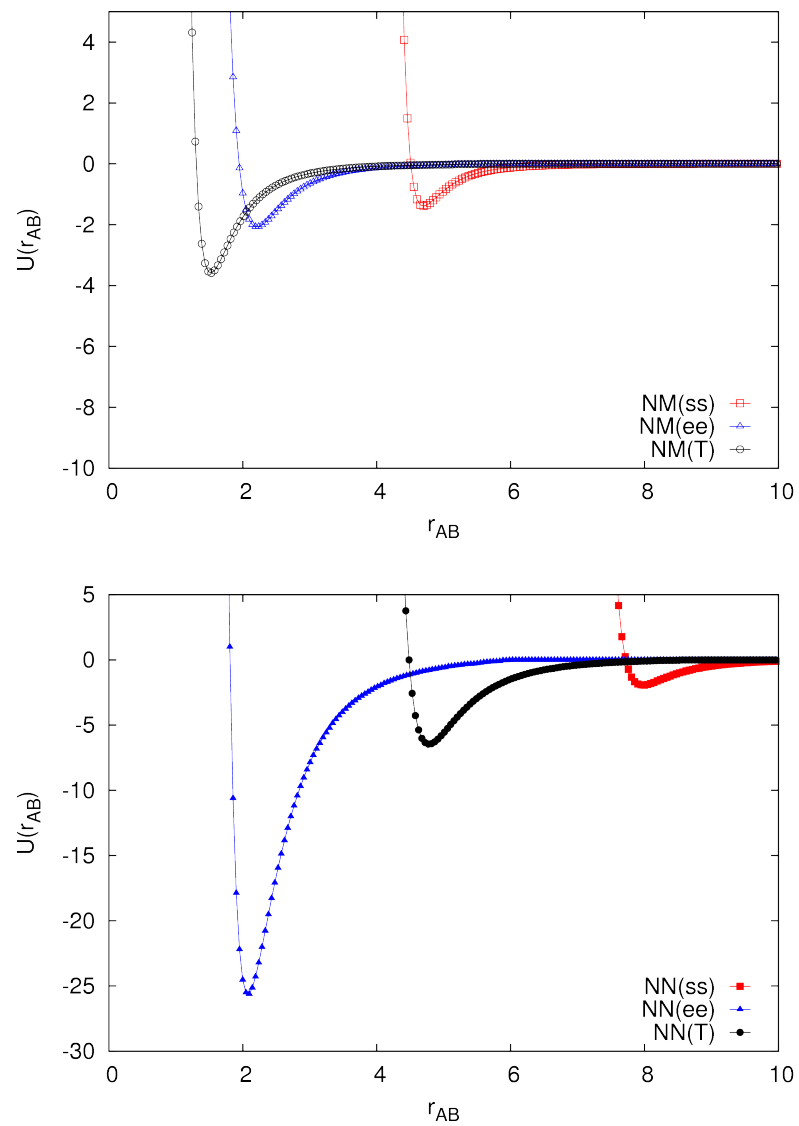


Figure 4.43: Potential profiles relative to both homogeneous disk-like nanoparticle–nanoparticle (NN) and heterogeneous nanoparticle–mesogen NM interaction for pairs in side-to-side, T-shape, and end-to-end configurations. The distance is plotted in terms of  $\sigma_0$  whilst the potential is in terms of  $\varepsilon_0$ .

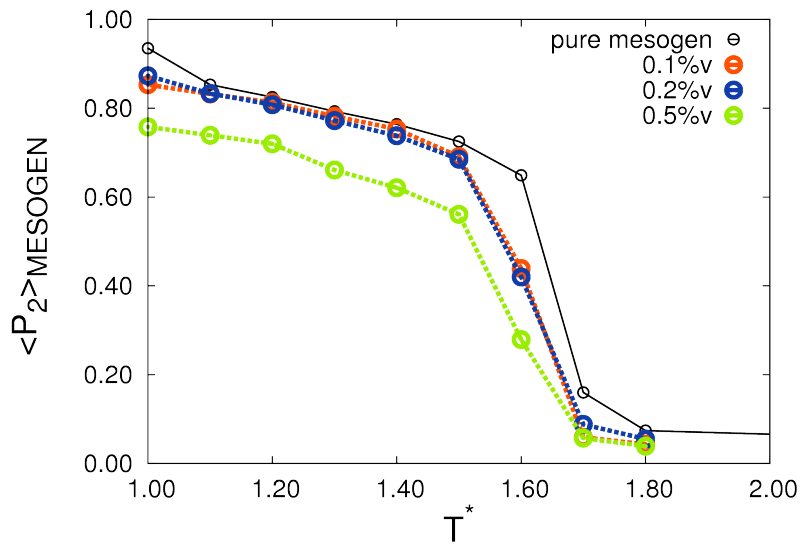


Figure 4.44: Orientational order parameter  $P_2$  for the NPT simulation at  $P^* = 8$ , against the dimensionless temperature  $T^*$  of the three mixtures of LC and NP; the data for the pure system are reported here for comparison.

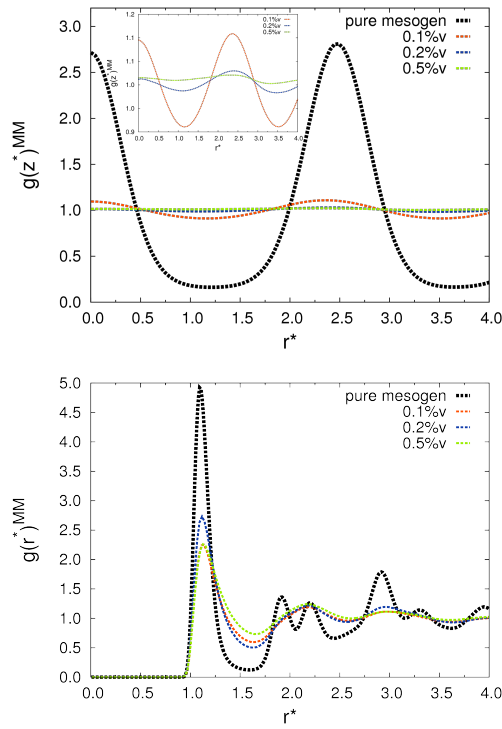


Figure 4.45: Radial correlation function (bottom) and density correlation function along the director (top) for  $c = 0.5\%$  for the reference temperature in smectic ( $T^* = 1.0$ ) phase. The curves in black report the behaviour of the pure LC system.

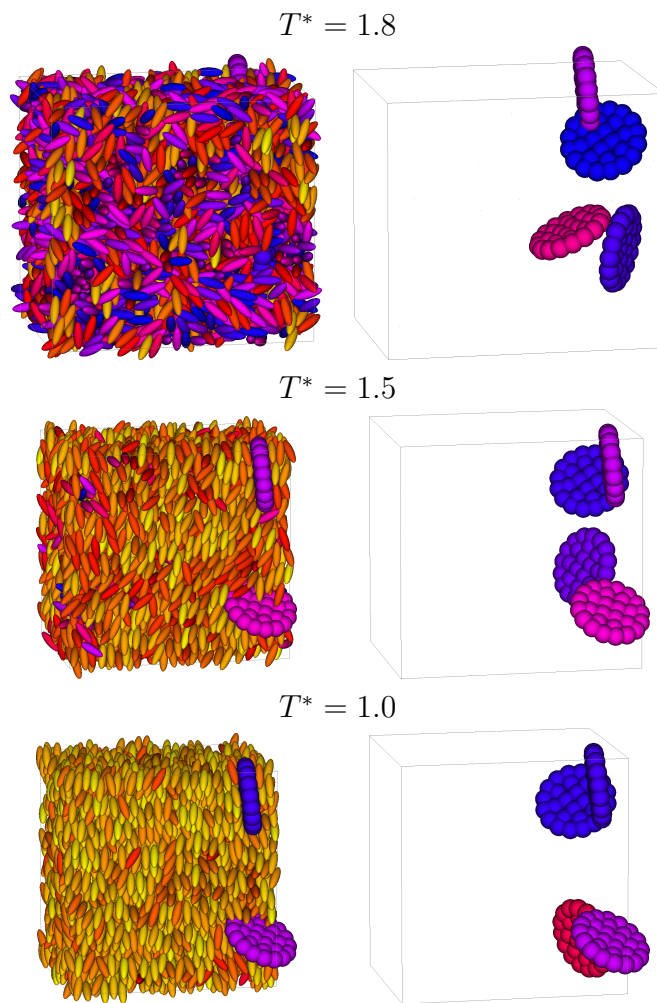


Figure 4.46: Snapshot of instantaneous configurations showing the molecular organization for  $T^* = 1.8, 1.5, 1.0$  at concentration  $c = 0.1\%$ .

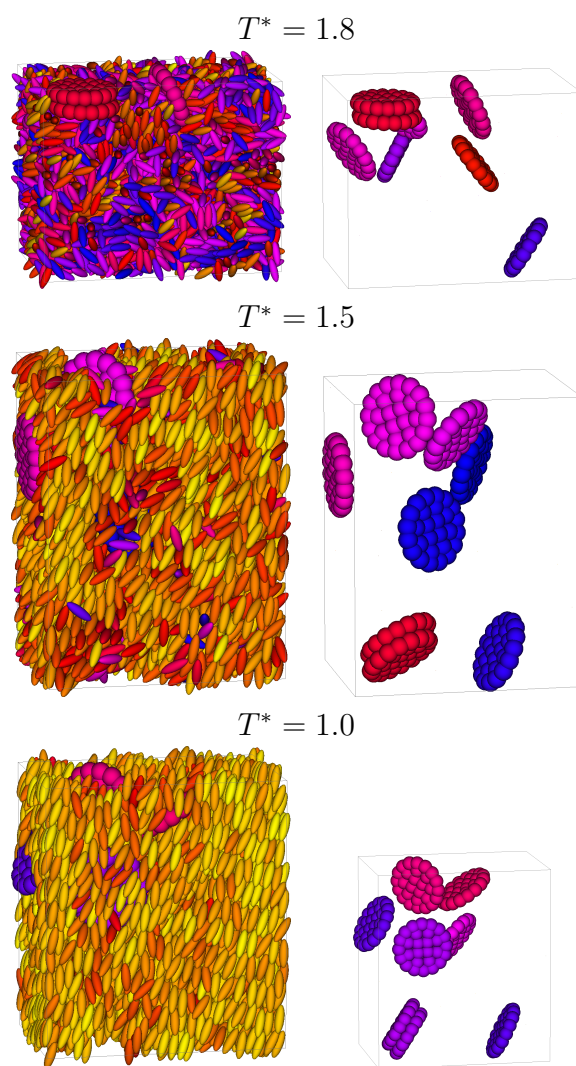


Figure 4.47: Snapshot of instantaneous configurations showing the molecular organization for  $T^* = 1.8, 1.5, 1.0$  at concentration  $c = 0.2\%$ .

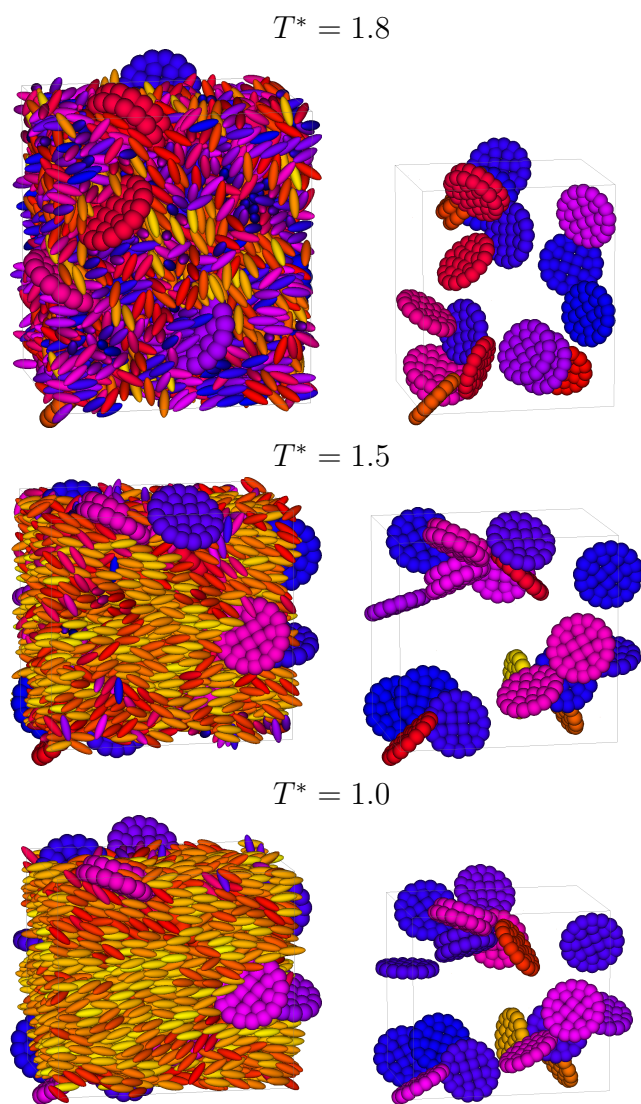


Figure 4.48: Snapshot of instantaneous configurations showing the molecular organization for  $T^* = 1.8, 1.5, 1.0$  at concentration  $c = 0.5\%$ .

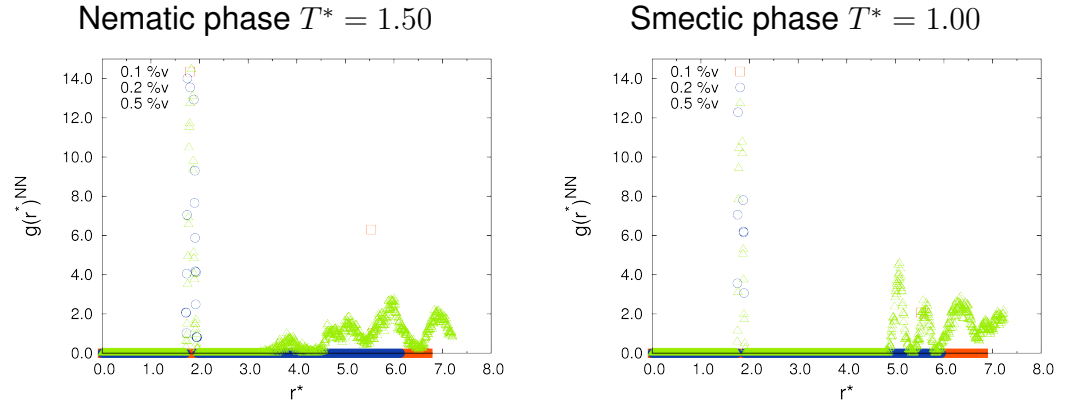


Figure 4.49: Nanoparticle–nanoparticle  $g(r)^{NN}$  correlation functions at  $T^* = 1.0$  and  $T^* = 1.5$  for  $c = 0.1\%$ ,  $0.2\%$ ,  $0.5\%$ .

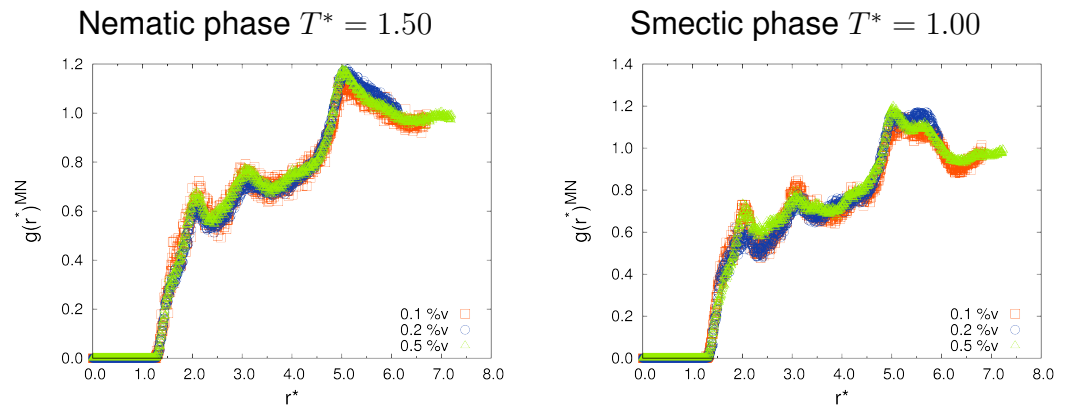


Figure 4.50: Mesogen–nanoparticle  $g(r)^{MN}$  correlation functions at  $T^* = 1.0$  and  $T^* = 1.5$  for  $c = 0.1\%$ ,  $0.2\%$ ,  $0.5\%$ .



## **Chapter 5**

### **Results - Doping LC with nanoparticle**

### **Effect of nanoparticle–mesogen and nanoparticle–nanoparticle interactions**

#### **5.1 NP rod with dipoles**

In the second part of this investigation we attempt to make a closer link with the structure of real LCs by adding a bit of chemical detail. Since charge distribution in typical molecules forming mesophases like 5CB plays an important role in determining their phase structure, we embedded a central electric point dipole, directed along the long molecular axis, in our rod-like mesogen model. Clearly this kind of geometry of the dipole is rather artificial and constitutes only an approximation; nevertheless, the effect of adding simple dipolar contributions to the GB potential has been successfully studied in [78–80] and important modifications have been observed in the overall molecular organization. This polar GB system will be exploited as a suitable solvent for polar dopant nanoparticles.

### 5.1.1 The dipolar interaction

In general the dipolar pair energy between two point dipoles  $i$  and  $j$  is

$$U_d(r_{ij}) = \frac{\mu_i \mu_j}{r_{ij}^3} [\hat{\mu}_i \cdot \hat{\mu}_j - 3(\hat{\mu}_i \cdot \hat{\mathbf{r}}_{ij})(\hat{\mu}_j \cdot \hat{\mathbf{r}}_{ij})] \quad (5.1)$$

where  $r_{ij}$  is the distance between dipolar sites,  $\mu_i, \mu_j$  the molecular dipoles with orientations  $\hat{\mu}_i$  and  $\hat{\mu}_j$  ( $\mu_i = \mu_i \hat{\mu}_i$ ,  $\mu_j = \mu_j \hat{\mu}_j$ ).

The pairwise long range dipolar interactions are the computationally most costly part of molecular simulations. The number of calculations for each atom scales with  $r^3$  where  $r$  is the spherical cutoff radius. To resolve the computational cost problem, Reaction Field (RF) and Ewald summation methods and improved version of these are applied. Ewald approximation methods [40,81–84] rely on splitting dipolar interactions into a short-range component which is computed by pairwise dipole–dipole summation, and a long-range component computed here by evaluating Fourier series directly. This is based on the assumption of exact periodicity within the simulated system.

In the Reaction Field method [40, 84, 85] each dipole is interacting with neighbouring dipoles within a cutoff sphere of radius  $R_c$ . The rest of the sample is approximated, as an electrostatic medium, like an homogeneous dielectric continuum of permittivity  $\epsilon_{RF}$  matching that of the explicit solvent. Continuum electrostatic equations are then solved using spherical symmetry to estimate the dipolar interaction with the particle as:

$$E_{RF} = \left( \frac{\epsilon_{RF} - 1}{2\epsilon_{RF} + 1} \right) \frac{1}{R_c^3} \sum_j \mu_j \quad (5.2)$$

where  $j$  is an index running over all the dipoles contained in the cavity. The energy of the interaction between the central dipole  $i$  and the Reaction Field is then given by:

$$U_{ext}(i) = -\mu_i \cdot \mathbf{E}_{RF} \quad (5.3)$$


in such a way that the contribution to the total energy is

$$U_{RF} = \frac{1}{2} \sum_i U_{ext}(i). \quad (5.4)$$

This long-range correction is then added to the short-range contribution which is computed via explicit summation over the neighbouring dipoles within the cutoff sphere.

### 5.1.2 Pure mesogenic system with dipoles

We investigated systems of Gay–Berne ellipsoids with an embedded central electric point dipole positioned at  $r_x$ ,  $r_y$ ,  $r_z$  in the molecular frame, oriented along the molecular axis with components  $\mu_x$ ,  $\mu_y$ ,  $\mu_z$ , as reported in Table 5.1.



Dipole moment	$r_x$	$r_y$	$r_z$	$\mu_x$	$\mu_y$	$\mu_z$
	0.0	0.0	0.0	0.0	0.0	1.5

Table 5.1

We use a dimensionless dipole moment  $\mu^* = (\mu^2/\varepsilon_0\sigma_0^3)^{1/2} = 1.5$ , expressed in  $\varepsilon_0$  and  $\sigma_0$  units, that correspond to about 5.5D, similar to that of 5CB. We have simulated a system of  $N = 1000$  dipolar rod-like Gay-Berne particles in the NPT ensemble at  $P^* = 8.0$  and  $1.0 < T^* < 2.0$ . The dipolar energy has been computed using the Reaction Field method with cutoff  $R_c = 6\sigma_0$  and dielectric constant of the surrounding medium  $\epsilon_{RF} = 1.5$ .

The behavior for the average  $P_2$  against temperature  $T^*$ , reported in Figure 5.1, evidence a slight shift of the  $T_{NI}$  towards higher temperature, with respect to the apolar system (see Figure 5.2 for instantaneous snapshots). Also, the system shows a more pronounced layering at low temperature as shown by the radial correlation function  $g_0(r)$  and the density along the director  $g(z)$ . In order to analyze in a quantitative way the molecular and dipolar organization, we report the polar orientational correlation function

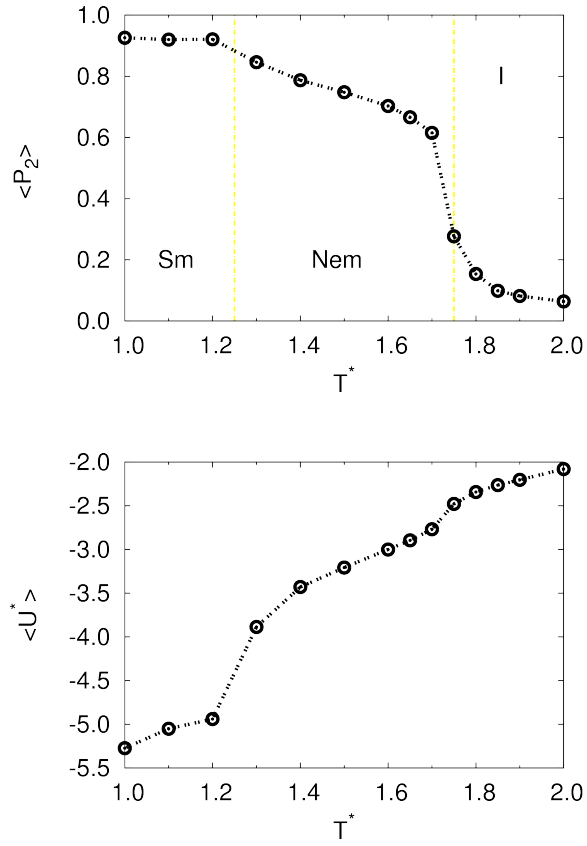
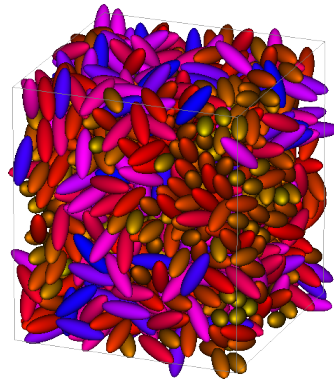
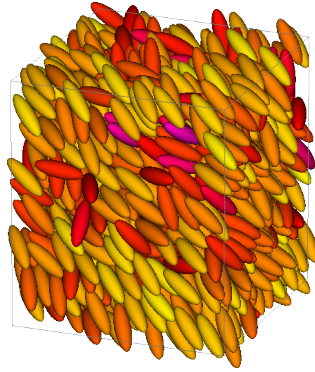


Figure 5.1: Average orientational order parameter  $\langle P_2 \rangle$ , energy  $U^*$  and number density  $N/V$ , plotted against the temperature in dimensionless units, for the system of rod particles without dipoles.

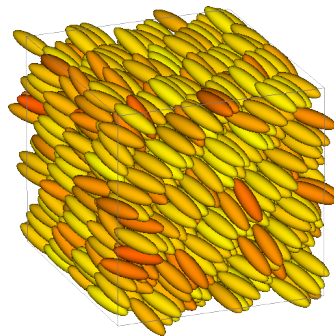
$g_{1z}(r)$  between the longitudinal axis  $z_i$  of a molecule chosen as origin and that of any other found at a distance  $r^*$ , which shows a weak correlation of antiparallel pairs (see Figure 5.3).



*Isotropic*



*Nematic*



*Smectic*

Figure 5.2: Molecular organization for the  $N = 1000$  system with dipoles  $\mu^* = 1.5$ , respectively in isotropic  $T^* = 1.8$ , nematic  $T^* = 1.5$ , and smectic  $T^* = 1.0$ , phase.

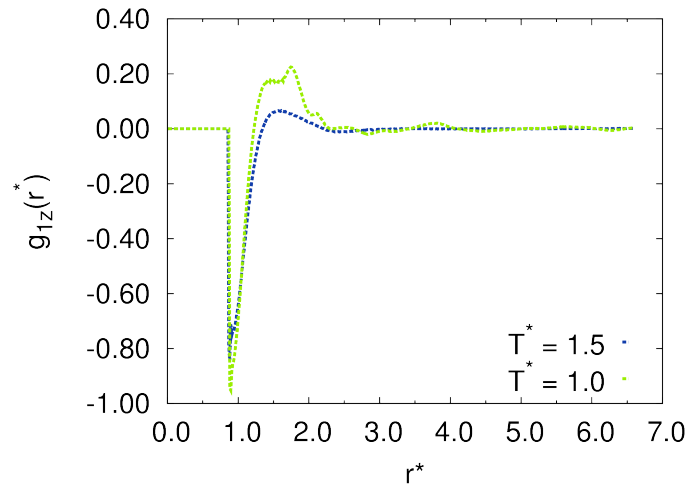


Figure 5.3: Correlation function  $g_{1z}$  for systems in the nematic ( $T^* = 1.5$ ) and smectic ( $T^* = 1.0$ ) phases.

## 5.2 Effect of the strength of interactions (nanoparticle–nanoparticle and nanoparticle– mesogen)

In order to explore the various possibilities of dispersion aggregation of NPs, for the specific nanoparticle with rod-like shape, we now discuss the results of several MC experiments, trying to assess the effect of strength of heterogenous nanoparticle-mesogen interaction (solvent affinity) and strength homogeneous nanoparticle-nanoparticle interaction on liquid crystalline phase (see Figure 5.4).

We performed simulations on mixtures formed by a constant number  $N = N_M + N_N = 5000$  of total particles, where  $N_M = 4975$  is the number of polar mesogenic molecules and  $N_N = 25$  is the number of rod-like nanoparticles corresponding to the solute fraction 0.5%. As in the previous cases, dimensionless pressure  $P^*$  was set to 8 while the temperature  $T^*$  spanned the range 1.0-1.8. We used two different values of the coupling parameter  $e_{NM}$  (defined in eq. 2.15), that is  $e_{NM} = 0.5$  and  $e_{NM} = 2.0$ , corresponding respectively to the low affinity and high affinity regimes. For each value of  $e_{NM}$  we also tested three values of  $\varepsilon_S$  (i.e. well depth of each spherical unit composing the NP) which acts as parameter controlling the homogeneous inter-nanoparticles interaction.

### 5.2.1 High solvent affinity

Figure 5.5 shows the pair potential profiles for both nanoparticle-nanoparticle (NN) and heterogenous nanoparticle-mesogen (NM) for  $e_{NM} = 2.0$ . The curves relative to the well depths  $\varepsilon_S = 0.15$  (already investigated in section 4.2.2), 1.0 and 2.0 are reported.

As turned out for apolar LC, embedding rod-like nanoparticles to the liquid crystal medium results in a shift of the NI transition temperature towards lower values and in a general lowering of the mesogenic orientational or-

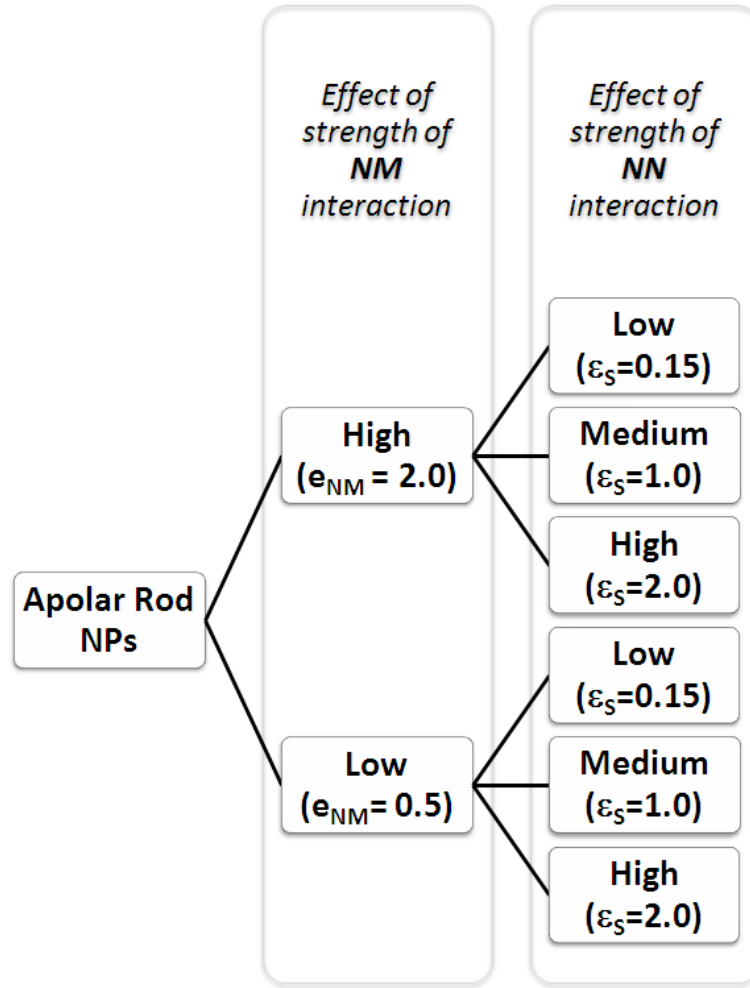


Figure 5.4: Sketch of the plan of work of this section.

der in comparison to the pure system (see Figure 5.6). Interestingly, this effect is observed regardless the values of the well depth  $\varepsilon_S$  (i.e. homogeneous NP–NP interaction); no evidence for local orientational order of nanoparticles is found for any value of  $\varepsilon_S$ . The resulting phase sequence is Iso–Nem–SmA, with suppression of the SmB phase at  $T^* = 1.0$  seen for pure mesogen system, as proven also by the absence of the characteristic double peak in the radial correlation function  $g(r)^{MM}$ , that is a fingerprint of an hexagonal arrangement of molecules in smectic layers (see Figure 5.7). Snapshots of instantaneous MC configurations are given in Figure 5.8, 5.9,



5.10.

A qualitative information about the local arrangement between nanoparticles and mesogenic molecules can be gained by examining the radial pair correlation functions for nanoparticle–mesogen  $g(r)^{NM}$  and  $g_{2z}(r)^{MN}$ <sup>1</sup> in smectic ( $T^* = 1.0$ ) and nematic ( $T^* = 1.5$ ) phases (see Figure 5.12). For any values of  $\varepsilon_s$ , a first small peak at  $r^* = 2.0$  is observed, corresponding to a nanoparticle–mesogen pair in *side–side* configuration with parallel orientations, as well as a second broad peak around  $r^* = 4.0$ , which is consistent with nanoparticle–mesogen still parallelly oriented. As before, this picture is consistent with a planar anchoring situation (see also Figure 5.13).

Focusing on the arrangement of nanoparticles,  $g(r)^{NN}$  curves for both  $T^* = 1.0$  and  $T^* = 1.5$  (Figure 5.11) exhibit a general slight tendency to dimerize, irrespective on the value of  $\varepsilon_s$ , as confirmed by showing a first non-zero value at approximately  $r^* = 3.0$ , which is the contact distance for NN pairs in *side–side* configuration. The scarcely structured profile at long–range suggest that nanoparticles avoid to aggregate in clusters of significant size, irrespective from the values of  $\varepsilon_s$ , as apparent from the snapshots in Figure 5.8, 5.9, 5.10 and also from the aggregates dispersion histograms in Figure 5.23 which report the number of the sampled aggregates against the number of their constituent molecules.

---

<sup>1</sup>Defined as  $g_{2z}(r)^{MN} = \langle \delta(r - r_{ij}) \left[ \frac{3}{2} (\hat{\mathbf{z}}_i \cdot \hat{\mathbf{z}}_j)^2 - \frac{1}{2} \right] \rangle_{ij}$

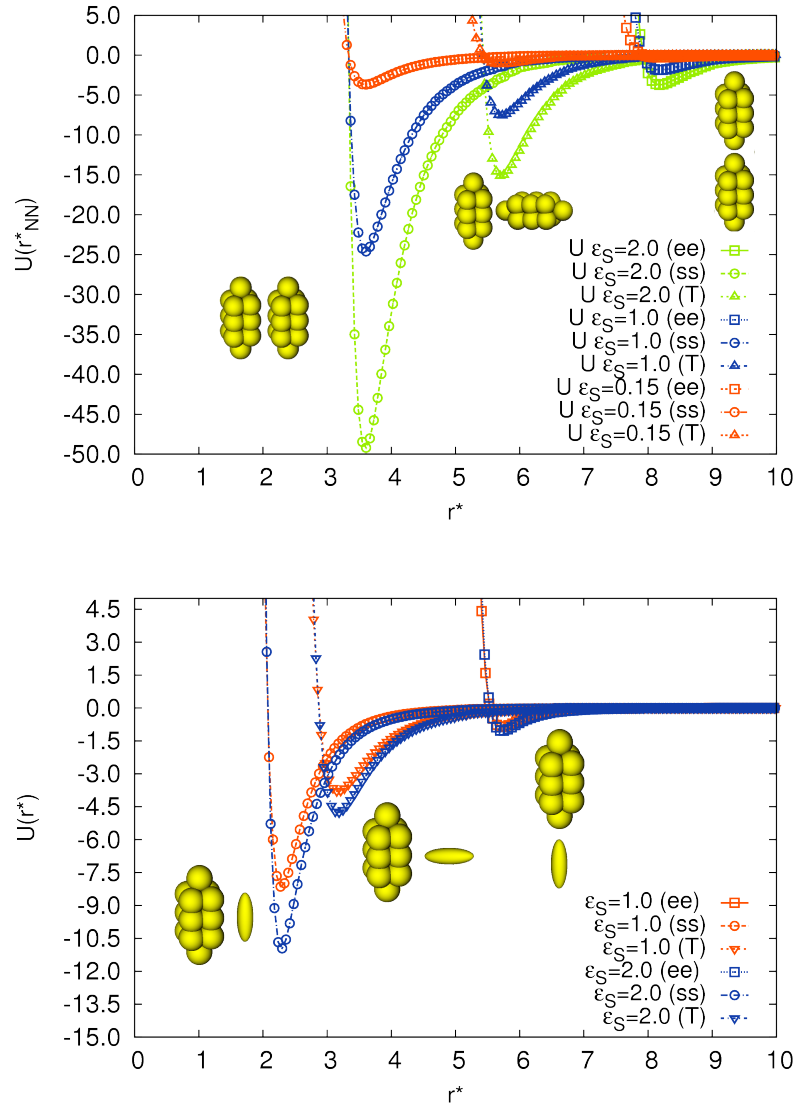


Figure 5.5: Pair potential profiles relative to homogeneous NN (bottom) and heterogeneous NM in the case of high affinity  $e_{MN} = 2.0$  (top) for three different cases of  $\epsilon_S$  (plotted for pairs in ss, ee,  $T$  configuration).

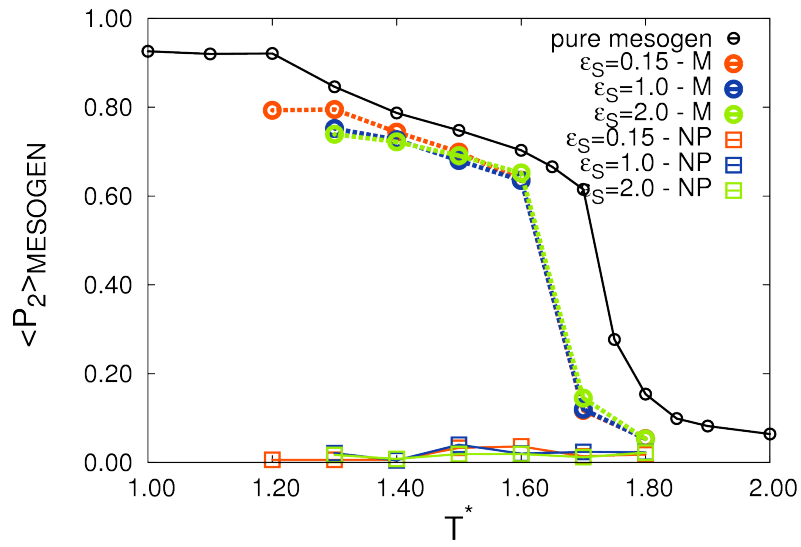


Figure 5.6: LC orientational order parameter  $P_2$  for the NPT simulation at  $P^* = 8$ , against the dimensionless temperature  $T^*$  of the three mixtures of polar LC and apolar rod-like NP. The local orientational order parameter relative to rod-like nanoparticles is also reported.

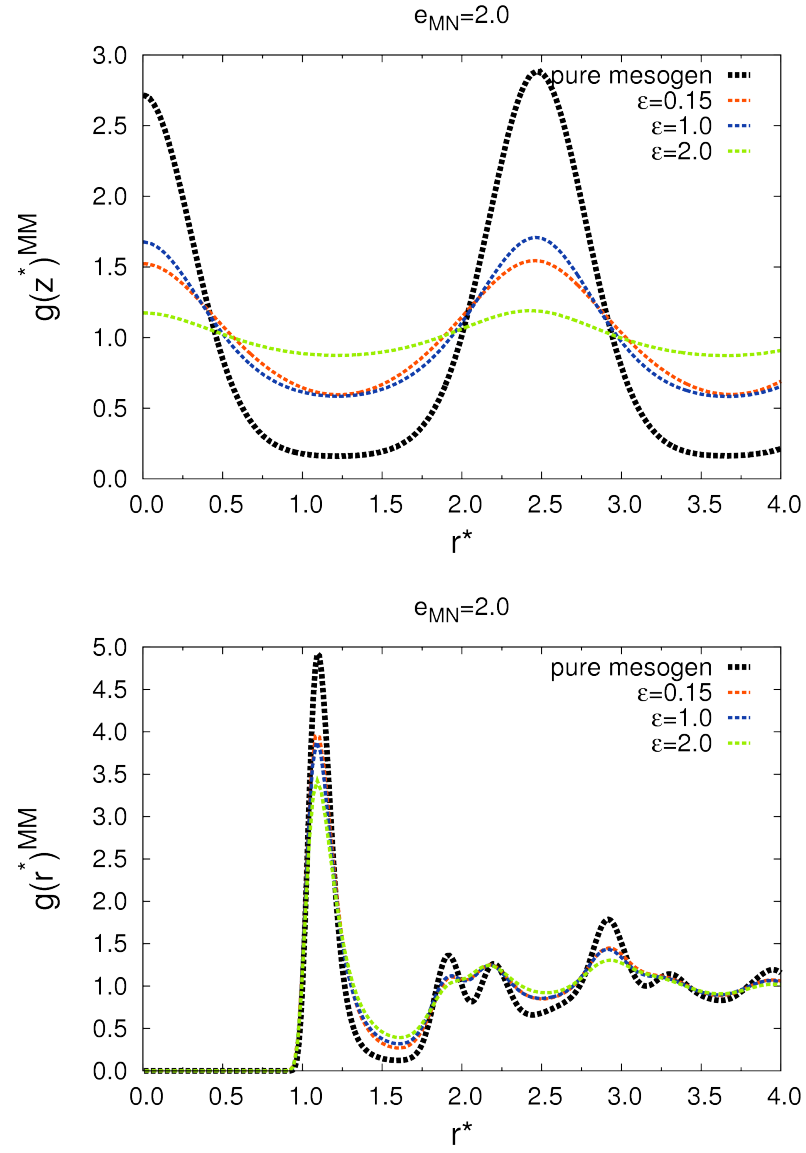
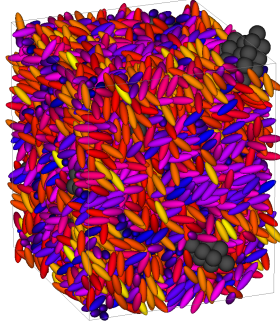
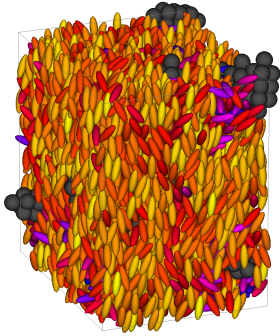


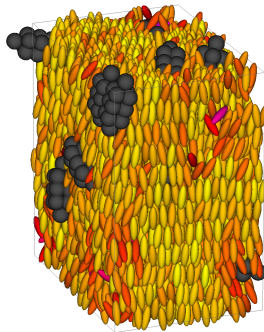
Figure 5.7: Radial correlation function and density correlation function along the director for  $\epsilon_S = 0.15, 1.0, 2.0$  in smectic phase ( $T^* = 1.0$ ). The curves in black report the behavior of the pure polar LC system.



$$T^* = 1.8$$

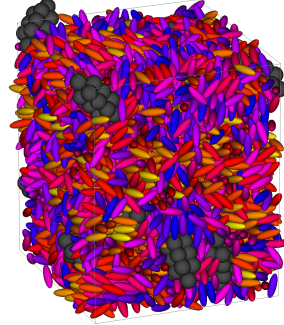


$$T^* = 1.5$$

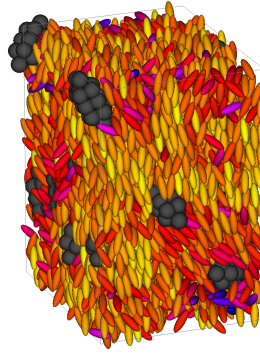


$$T^* = 1.0$$

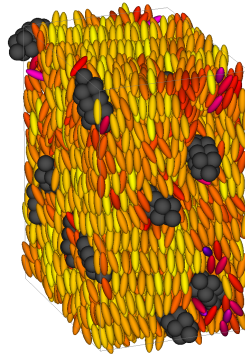
Figure 5.8: Snapshot of instantaneous configurations showing the molecular organization at temperatures  $T^* = 1.0, 1.5, 1.8$  for the system at  $\varepsilon_S = 0.15$ .



$$T^* = 1.8$$

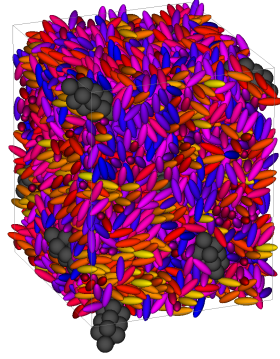


$$T^* = 1.5$$

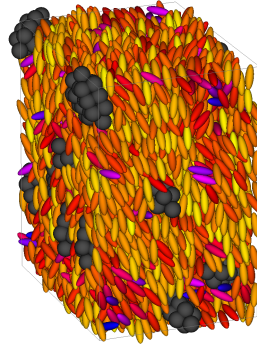


$$T^* = 1.0$$

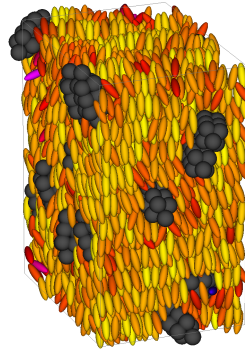
Figure 5.9: Snapshot of instantaneous configurations showing the molecular organization at temperatures  $T^* = 1.0, 1.5, 1.8$  for the system at  $\varepsilon_S = 1.0$ .



$$T^* = 1.8$$



$$T^* = 1.5$$



$$T^* = 1.0$$

Figure 5.10: Snapshot of instantaneous configurations showing the molecular organization at temperatures  $T^* = 1.0, 1.5, 1.8$  for the system at  $\varepsilon_S = 2.0$ .

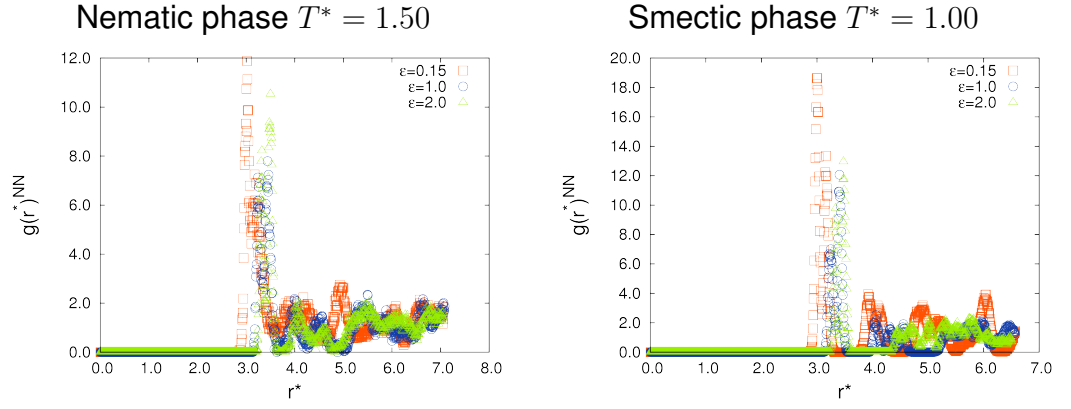


Figure 5.11: Radial correlation function  $g(r)^{NN}$  referred to NN particles for  $\varepsilon_S = 0.15, 1.0, 2.0$  for reference temperatures in smectic ( $T^* = 1.0$ ) and nematic ( $T^* = 1.5$ ) phases.

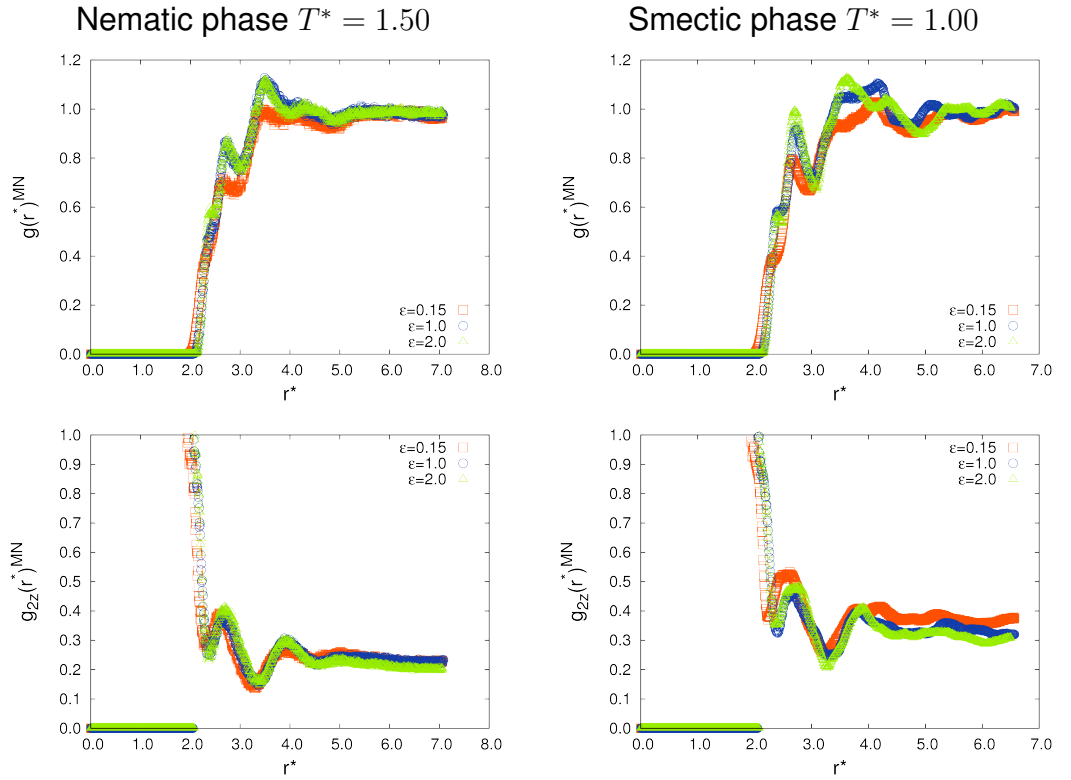


Figure 5.12: Mesogen–nanoparticle  $g(r)^{MN}$  (top) and  $g_{2z}(r)^{MN}$  (bottom) correlation functions at  $T^* = 1.5$  and  $T^* = 1.0$  for  $\varepsilon_S = 0.15, 1.0, 2.0$ .



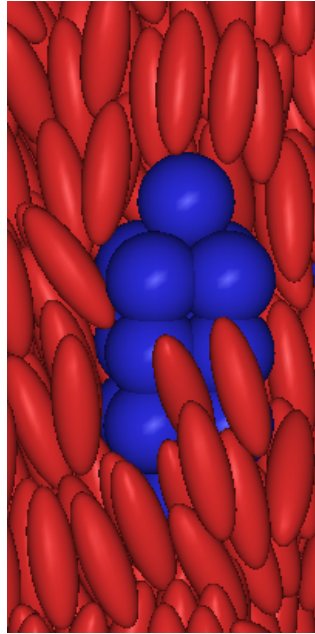
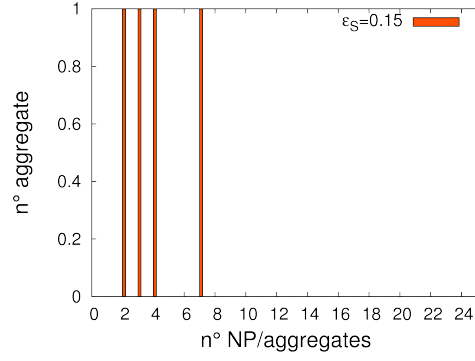


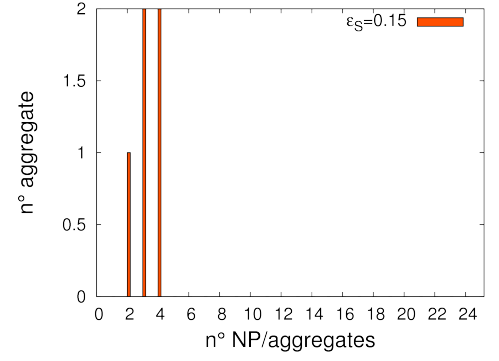
Figure 5.13: Longitudinal section of a portion of an instantaneous configuration at  $T^* = 1.5$ ,  $c = 0.1\%$  and  $\varepsilon_S = 2.0$  showing a parallel anchoring.

Temperature  $T^* = 1.5$  - Nematic phase

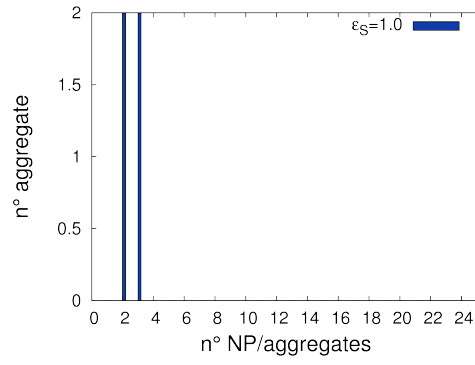
Temperature  $T^* = 1.0$  - Smectic phase



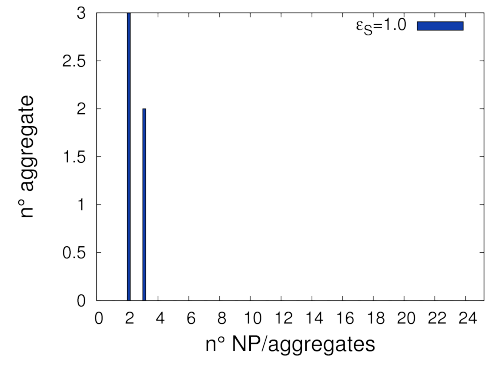
(a)



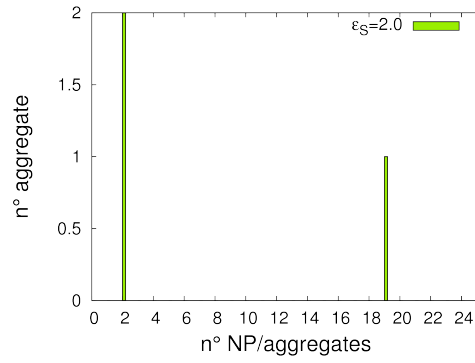
(d)



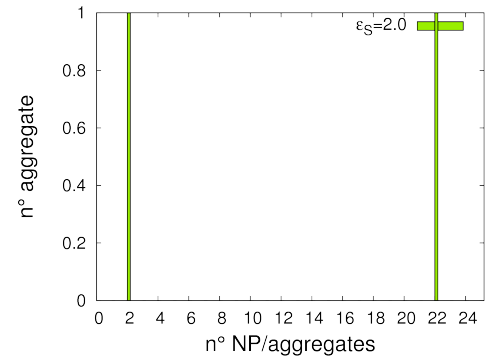
(b)



(e)



(c)



(f)

Figure 5.14: Nanoparticles aggregates dispersion histograms for  $T^* = 1.5$  (left) and  $T^* = 1.0$  (right) for different values of  $\varepsilon_S$ .

## 5.2.2 Low solvent affinity

Figure 5.15 shows the pair potential profiles relative to heterogeneous nanoparticle-mesogen (NM) for the low affinity case (i.e. coupling parameter  $e_{NM} = 0.5$ ). As expected, NM pairs have weaker interactions with respect to the previous, high affinity case and, in turn, the homogeneous NN interactions become dominant.

Looking at the temperature dependence of the order parameter  $\langle P_2 \rangle$  (shown in Figure 5.16 for the three values of  $\varepsilon_S$ ), we notice a shift of the NI transition temperature towards lower values and a general lowering of the mesogenic orientational order in comparison to the pure system even if reduced with respect to the  $e_{MN} = 2$  case; in particular for  $\varepsilon_S = 2.0$  (maximum NP–NP interaction) the LC orientational order is only weakly altered by the dopant NPs. From the radial correlation function and the density correlation function along the director referred to MM particles for  $\varepsilon_S = 0.15, 1, 2$  given in Figure 5.17, we can observe that the phase sequence Iso–Nem–Sm is maintained and in the case of  $\varepsilon_S = 2.0$  the survival of the SmB; snapshots of instantaneous MC configurations are given in Figure 5.18, 5.19, 5.20.

The arrangement between nanoparticles can be gathered by the nanoparticle–nanoparticle radial pair correlation functions  $g(r)^{NN}$  in Figure 5.21, presented here for  $T^* = 1.5$  (nematic phase) and  $T^* = 1.0$  (smectic phase). Interestingly, for the  $\varepsilon_S = 2.0$  case (strong NN interaction), both curves evidence a drastic rise in the magnitude of the first peak (which corresponds to the lateral dimension of NPs), as well as a structure of peaks at large distance. This indicates a situation in which NP strongly aggregate in clusters, as apparent in Figure 5.24. Instead, for the  $\varepsilon_S = 0.15$  case (weak NN interaction) the first peak is sensitively smaller and also the profile at long range is less structured, thus suggesting a situation in which NPs may dimerize, but are prevented from forming large aggregates.

Finally the radial correlation function  $g(r)^{MN}$  and the orientational correlation function  $g_{2z}(r)^{MN}$  referred to nanoparticle–mesogen pairs (Fig-

ure 5.22) convey some information about the local organization of the mesogens around a nanoparticle. Notably both functions are sensitive to the homogenous NN interaction strenght (i.e. the  $\varepsilon_S$  value). In fact, while for  $\varepsilon_S = 0.15$  and  $\varepsilon_s = 1.0$ , behaviors similar to the high affinity case are found, for  $\varepsilon_S = 2.0$  we evidence a reduction of the peak relative to NM pairs parallelly oriented in *side-side* configuration; in addition, and more interestingly, the orientational correlation is lost for  $r^* > 3$ .

From Figure 5.23 we can observe a different aggregation behavior: lowering the affinity between nanoparticle and mesogen allows the formation of clusters, whose dimensions depend on the strength of nanoparticle–nanoparticle interactions. Analyzing a representative cluster (which appear in the most favourable case:  $e_{MN} = 0.5$  and  $\varepsilon_S = 2.0$ ), shown in Figure 5.24, we could see that the NPs tend to maintain a random orientation instead of orienting themselves along a preferred direction. The cluster, characterized by radius of gyration  $R_g = 10.9$ , does not undergo considerable changes of shape and dimension as a function of temperature; moreover it is oriented almost perpendicular with respect to the director of the nematic phase with a tilt angle of  $87^\circ$ , as we can see in Figure 5.24.

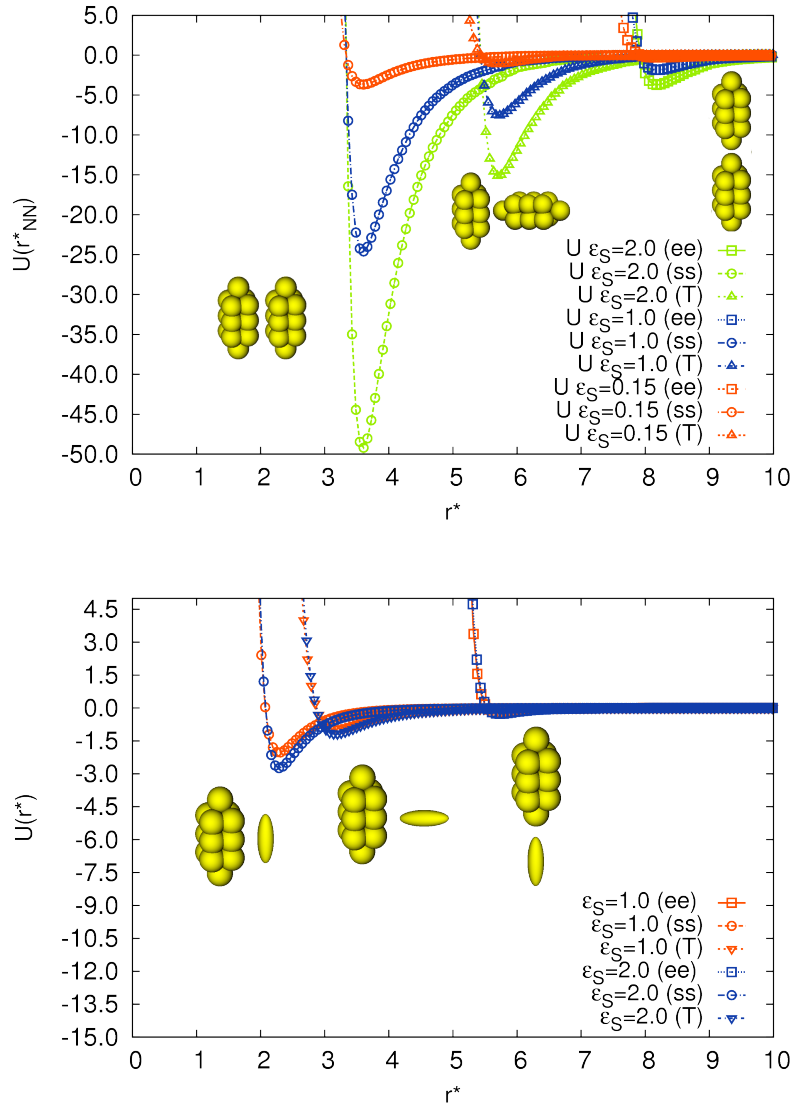


Figure 5.15: Pair potential profiles relative to homogeneous NN (bottom) and heterogeneous NM in the case of low affinity  $e_{MN} = 0.5$  (top) for three different cases of  $\epsilon_S$  (plotted for pairs in ss, ee, T configuration).

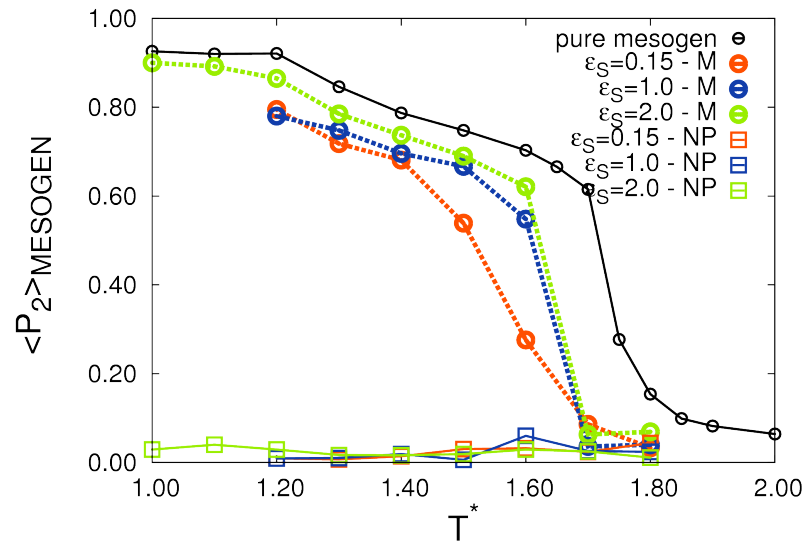


Figure 5.16: LC orientational order parameter  $P_2$  for the NPT simulation at  $P^* = 8$ , against the dimensionless temperature  $T^*$  of the three mixtures of polar LC and rod-like NP. The local orientational order parameter relative to rod-like nanoparticles is also reported.

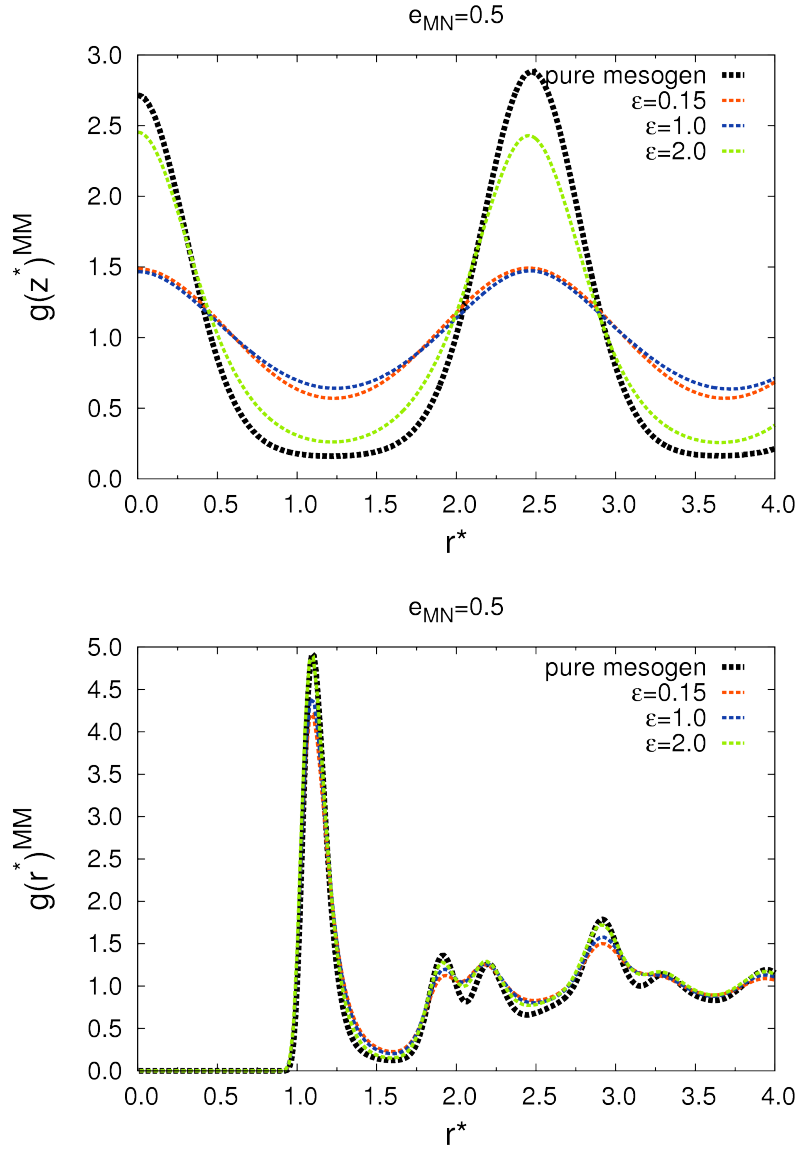
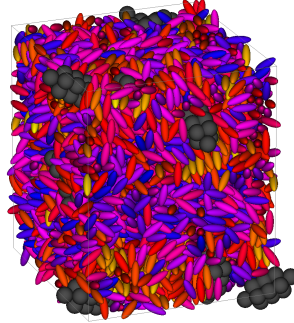
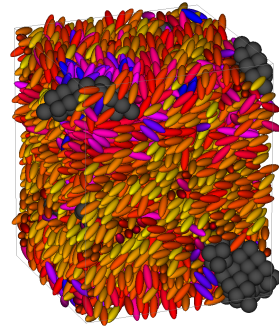


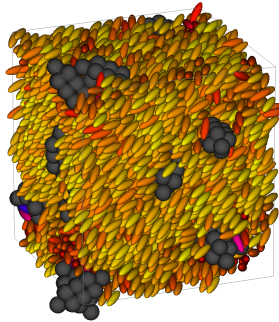
Figure 5.17: Radial correlation function and density correlation function along the director for  $\varepsilon_S = 0.15, 1.0, 2.0$  in smectic phase ( $T^* = 1.0$ ). The curves in black report the behavior of the pure polar LC system.



$$T^* = 1.8$$



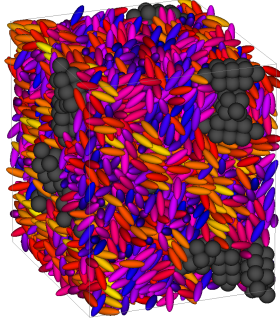
$$T^* = 1.5$$



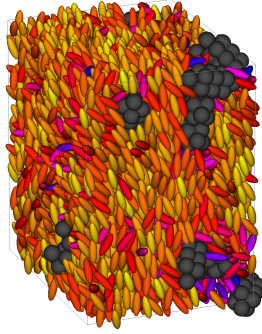
$$T^* = 1.0$$

Figure 5.18: Snapshot of instantaneous configurations showing the molecular organization at temperatures  $T^* = 1.0, 1.5, 1.8$  for the system at  $\varepsilon_S = 0.15$ .

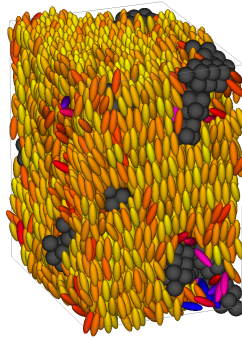




$$T^* = 1.8$$

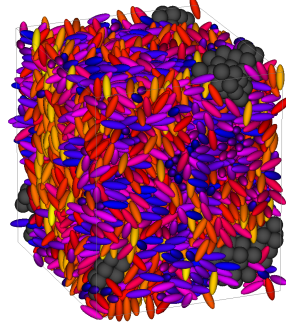


$$T^* = 1.5$$

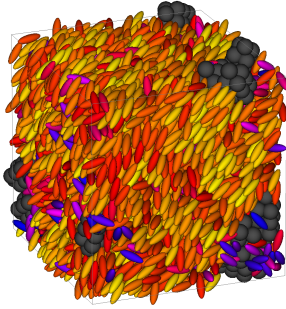


$$T^* = 1.0$$

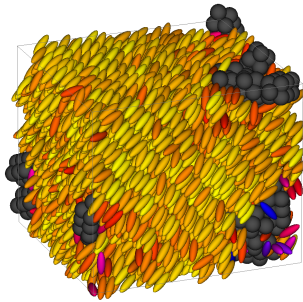
Figure 5.19: Snapshot of instantaneous configurations showing the molecular organization at temperatures  $T^* = 1.0, 1.5, 1.8$  for the system at  $\varepsilon_S = 1.0$ .



$$T^* = 1.8$$



$$T^* = 1.5$$



$$T^* = 1.0$$

Figure 5.20: Snapshot of instantaneous configurations showing the molecular organization at temperatures  $T^* = 1.0, 1.5, 1.8$  for the system at  $\varepsilon_S = 2.0$ .

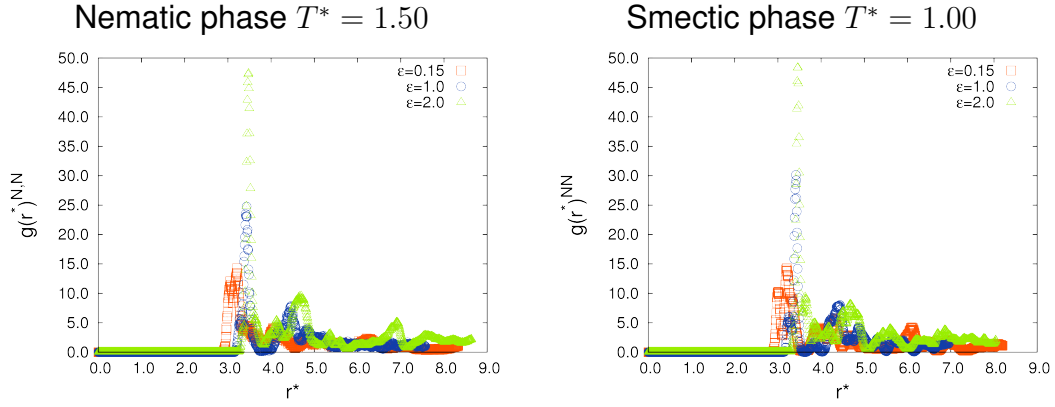


Figure 5.21: Radial correlation function  $g(r)^{NN}$  referred to NN particles for  $\varepsilon_S = 0.15, 1.0, 2.0$  for reference temperatures in smectic ( $T^* = 1.0$ ) and nematic ( $T^* = 1.5$ ) phase.

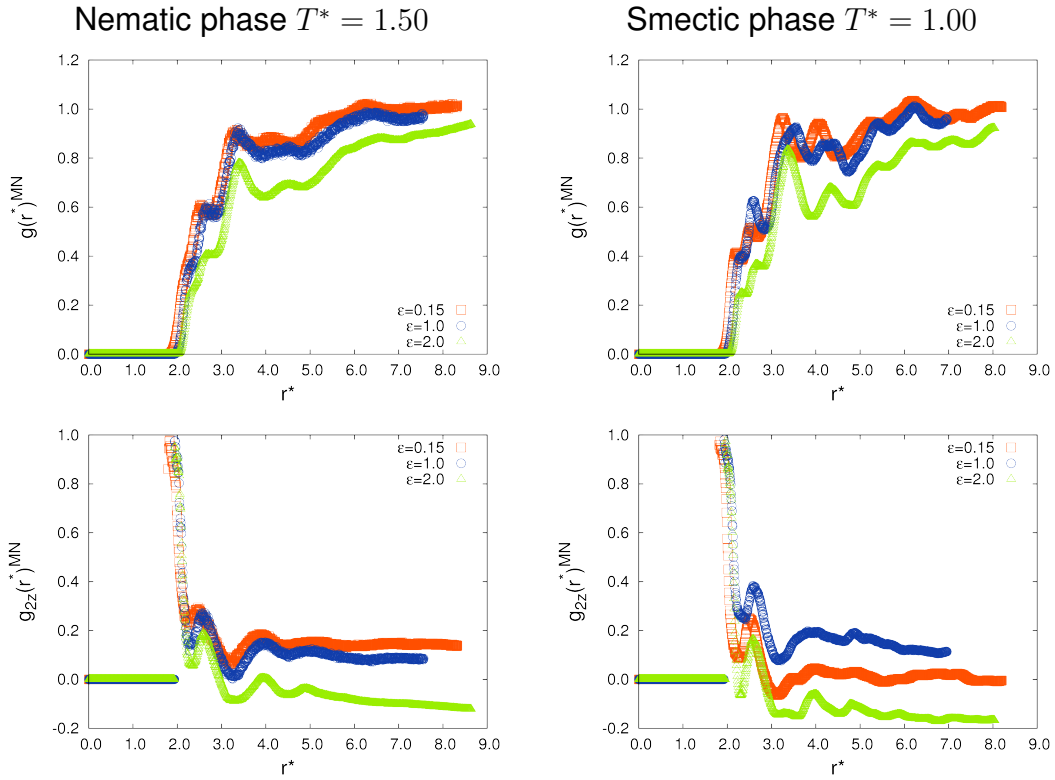
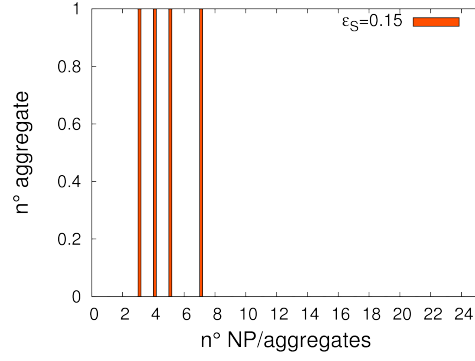


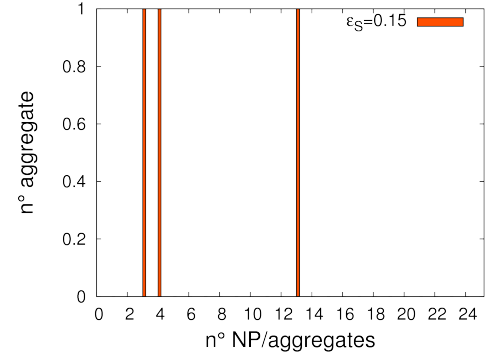
Figure 5.22: Mesogen–nanoparticle  $g(r)^{MN}$  (top) and  $g_{2z}(r)^{MN}$  (bottom) correlation functions at  $T^* = 1.5$  and  $T^* = 1.0$  for  $\varepsilon_S = 0.15, 1.0, 2.0$ .

Temperature  $T^* = 1.5$  - Nematic phase

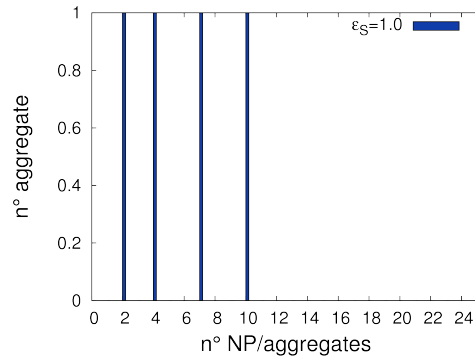
Temperature  $T^* = 1.0$  - Smectic phase



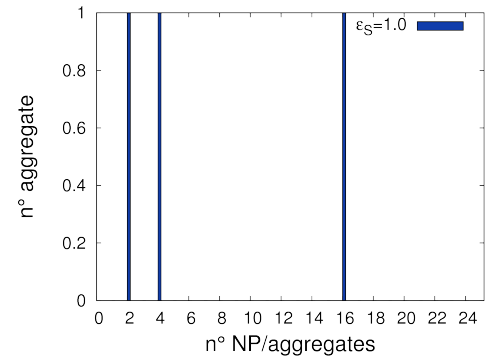
(a)



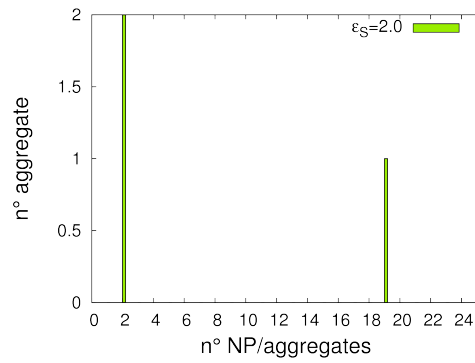
(d)



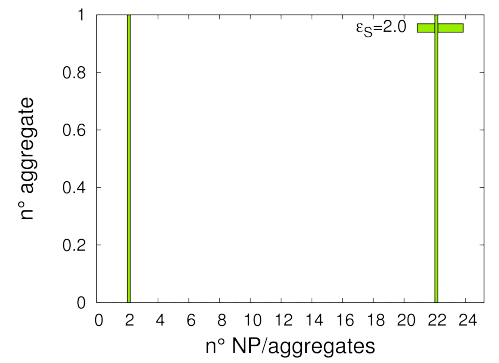
(b)



(e)

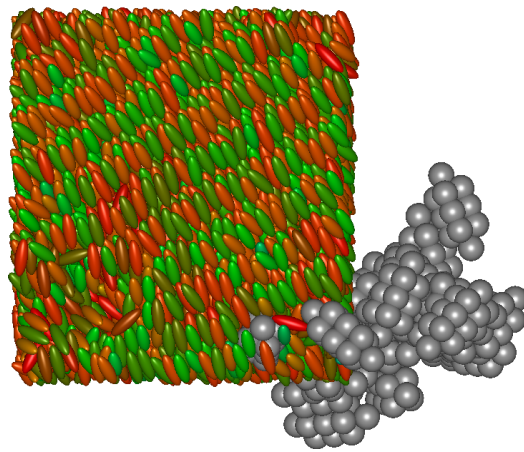


(c)



(f)

Figure 5.23: Nanoparticles aggregates dispersion histograms for  $T^* = 1.5$  (left) and  $T^* = 1.0$  (right) for different values of  $\varepsilon_S$ .



$$T^* = 1.0$$

Figure 5.24: Cluster of nanoparticles (after removing periodic boundary conditions) at temperature  $T^* = 1.0$  for the system with stronger NN interactions ( $\varepsilon_S = 2.0$ ).

### 5.2.3 Effect of nanoparticle embedded dipoles

In this section we focus on the effects on the liquid crystalline phase associated to the presence of longitudinal centered dipole moment in the rod-like NPs with low affinity between nanoparticles and LC solvent, varying the interaction between nanoparticles (see scheme on Figure 5.25).

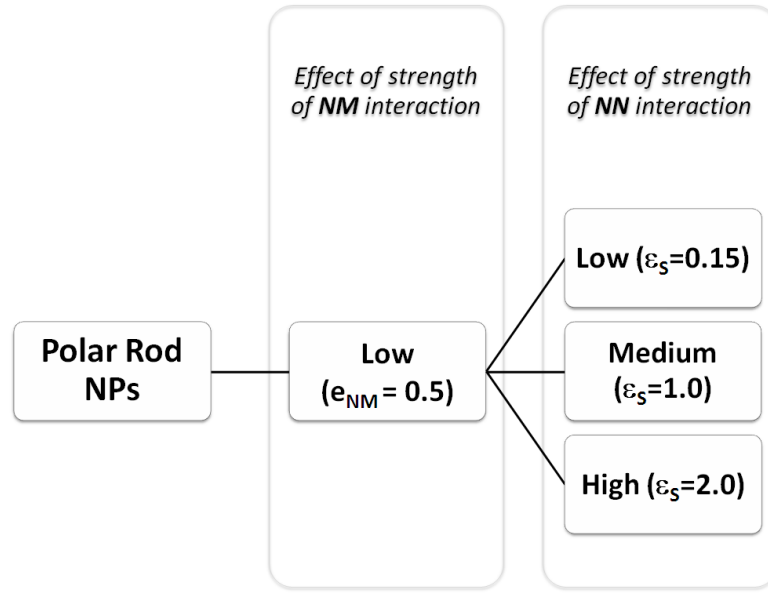


Figure 5.25: Sketch of the plan of work of this section.

We considered a sample mixture formed by constant number  $N_M + N_N = 5000$  total particles, where  $N_M = 4975$  is the number of polar GB molecules and  $N_N = 25$  is the number of rod-like particle corresponding to the solute fraction 0.5%. We assumed a dipole strength  $\mu^* = 1.5$  for the mesogen and  $\mu^* = 20$  for the nanoparticle, corresponding to about 75D. As before, interactions were calculated with the Reaction Field method setting the external permittivity to  $\varepsilon_{RF} = 1.5$  and cutoff  $R_C = 10\sigma_0$ .

### Low solvent affinity

By analysing the order parameter  $\langle P_2 \rangle$  against the temperature  $T^*$  plot, reported in Figure 5.26, we evidenced behaviors comparable to the ones already revealed from apolar NP for small and medium homogeneous NN interactions ( $\varepsilon_S = 0.15$  and  $1.0$ ). Instead, and more interestingly, for the strongest homogeneous NN interaction ( $\varepsilon_S = 2.0$ ), the NI transition remains unvaried with respect to the pure mesogenic system and overall both the orientational and positional order are substantially not affected by the introduction of NPs. This is confirmed by the examination of the radial distribution  $g(r)^{MM}$  and density distribution  $g(z)^{MM}$  at  $T^* = 1.0$  (see Figure 5.27) which, for  $\varepsilon_S = 2.0$ , exhibit stronger nearest neighbour peak compared with the apolar system as well as a stronger layering. Snapshots

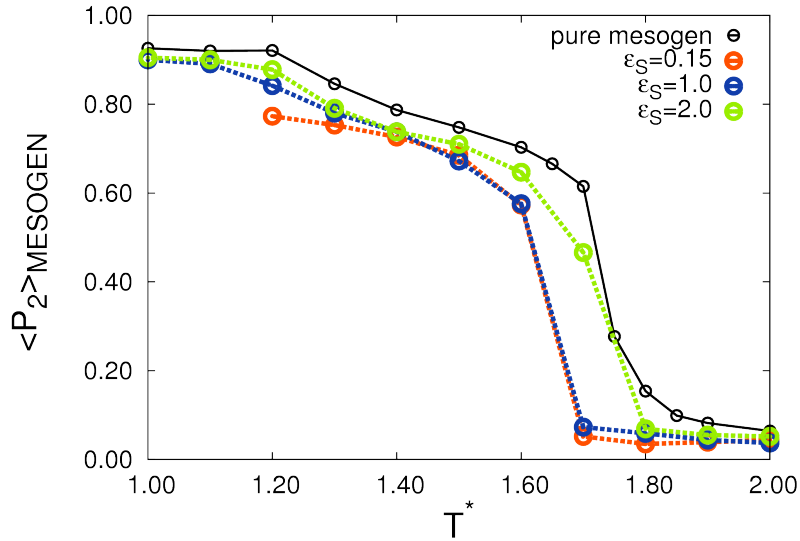


Figure 5.26: LC orientational order parameter  $P_2$  for the NPT simulation at  $P^* = 8$ , against the dimensionless temperature  $T^*$  of the three mixtures of polar LC and rod-like NP.

of instantaneous configurations in Figure 5.28, 5.29, 5.30 for different  $\varepsilon_S$  reveals the phase obtained, and give some hints about the arrangement of nanoparticles.

The radial correlation function  $g(r)^{MN}$  and the orientational correlation function  $g_{2z}(r)^{MN}$  referred to nanoparticle–mesogen pairs (Figure 5.31) convey some information about the local organization of the mesogens around a nanoparticle. Notably both functions are sensitive to the homogenous NN interaction strenght (i.e. the  $\varepsilon_S$  value). In fact, for  $\varepsilon_S = 2.0$ , we evidence a reduction of the peak relative to NM pairs parallelly oriented in *side-side* configuration. The radial correlation function  $g(r)^{NM}$  and the orientational correlation function  $g_{2z}(r)^{NM}$  referred to nanoparticle–mesogen pairs shows similar features of apolar NPs with clear indication of a parallel-type anchoring of mesogens on NPs. As expected, an antiparallel alignment of mesogens with respect to neighbor nanoparticles is found, as pointed out by the correlation function  $g_{1z}(r)^{NM}$ .

Notably, for the maximum NN interaction, nanoparticles tend to form aggregates of large dimension (as detailed by histograms in Figure 5.33), as pointed out also by the  $g(r)^{NN}$  radial pair correlation function which exhibits an enhanced peak at  $r^* = 3.0$  (the lateral contact distance – see Figure 5.32) and a significant structure at long-range.

Still, the aggregate shape does not vary with temperature, but differently from the previous case, NPs tend to orient themselves along the mesophase director (as strenghtened by the behaviour of the  $\langle P_2 \rangle_{LOC}^{NANO}$ ), due to their embedded longitudinal dipole moments. The measured tilt angle between the aggregate principal axis and the mesophase director is approximately  $40^\circ$  (see Figure 5.34).

We calculated both the local first rank  $\langle P_1 \rangle_{LOC}^{NANO}$  and second rank  $\langle P_2 \rangle_{LOC}^{NANO}$  order parameter referred to the nanoparticles, as reported in Figure 5.35. Overall or local polarization is not found for any values of the temperature; instead the values of  $\langle P_2 \rangle$ , computed on the nanoparticles composing the aggregate, assume increasing values upon cooling down the temperature. As a further information on the polar correlation we computed the average scalar product  $g_{1z}^{NN}$  between the longitudinal axis  $z_i$  of a nanoparticle molecule chosen as origin and that of any other found at a distance  $r^*$ ,



reported in Figure 5.32 at  $T^*1.0$  and  $T^* = 1.5$ , that shows an antiparallel arrangement.

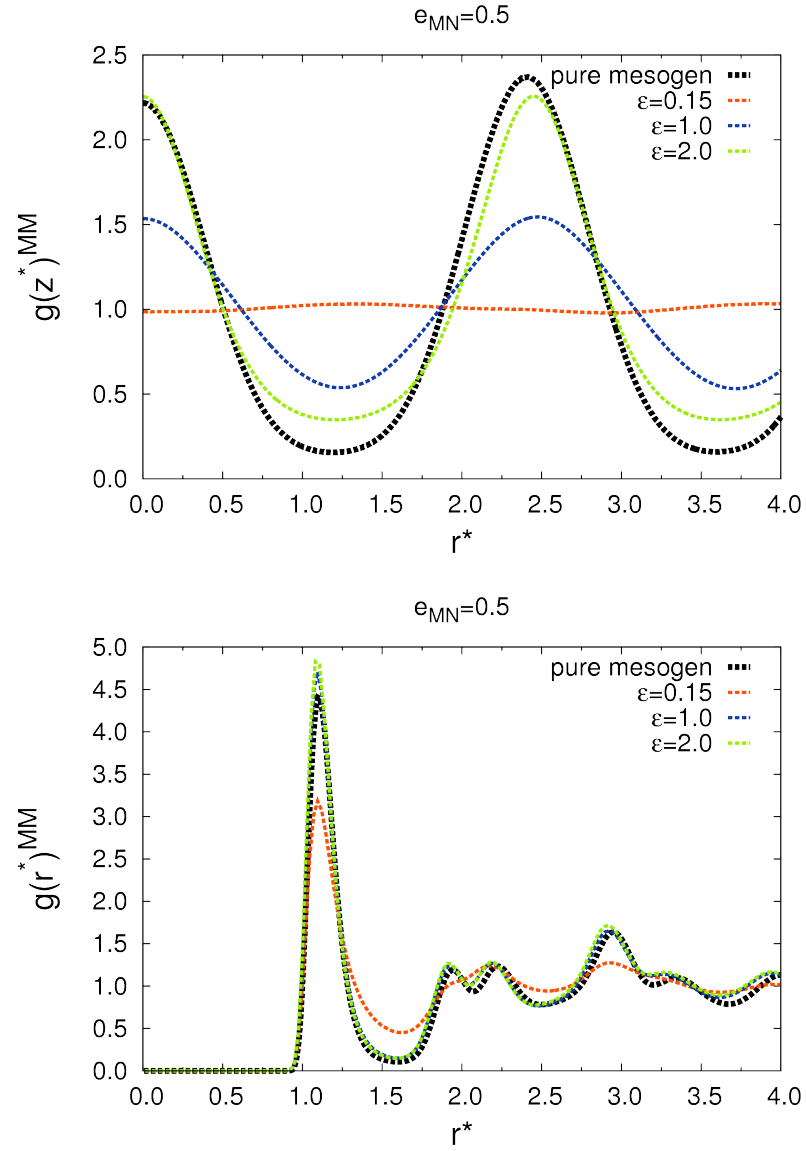
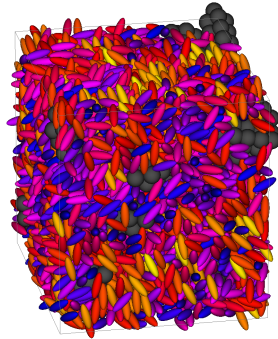
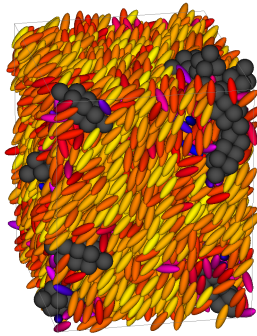


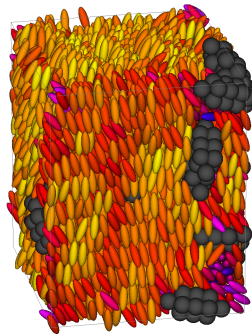
Figure 5.27: Radial correlation function and density correlation function along the director for  $\varepsilon_S = 0.15, 1.0, 2.0$  in smectic phase ( $T^* = 1.0$ ). The curves in black report the behavior of the pure polar LC system.



$$T^* = 1.8$$

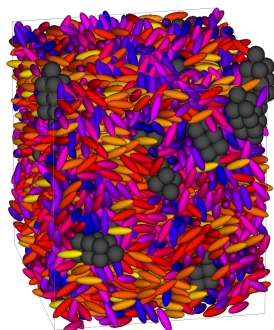


$$T^* = 1.5$$

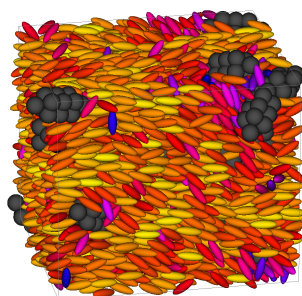


$$T^* = 1.0$$

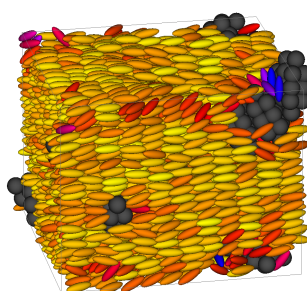
Figure 5.28: Snapshot of instantaneous configurations showing the molecular organization at temperatures  $T^* = 1.0, 1.5, 1.8$  for the system at  $\varepsilon_S = 0.15$ .



$$T^* = 1.8$$

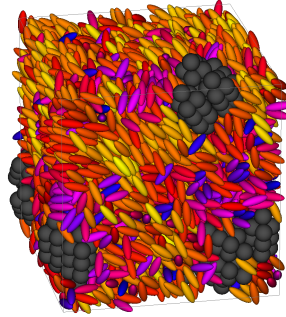


$$T^* = 1.5$$

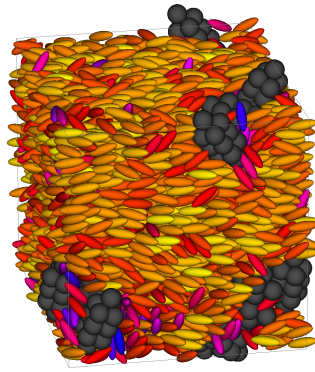


$$T^* = 1.0$$

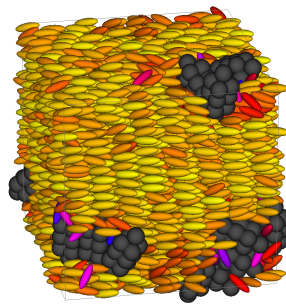
Figure 5.29: Snapshot of instantaneous configurations showing the molecular organization at temperatures  $T^* = 1.0, 1.5, 1.8$  for the system at  $\varepsilon_S = 1.0$ .



$$T^* = 1.8$$



$$T^* = 1.5$$



$$T^* = 1.0$$

Figure 5.30: Snapshot of instantaneous configurations showing the molecular organization at temperatures  $T^* = 1.0, 1.5, 1.8$  for the system at  $\varepsilon_S = 2.0$ .

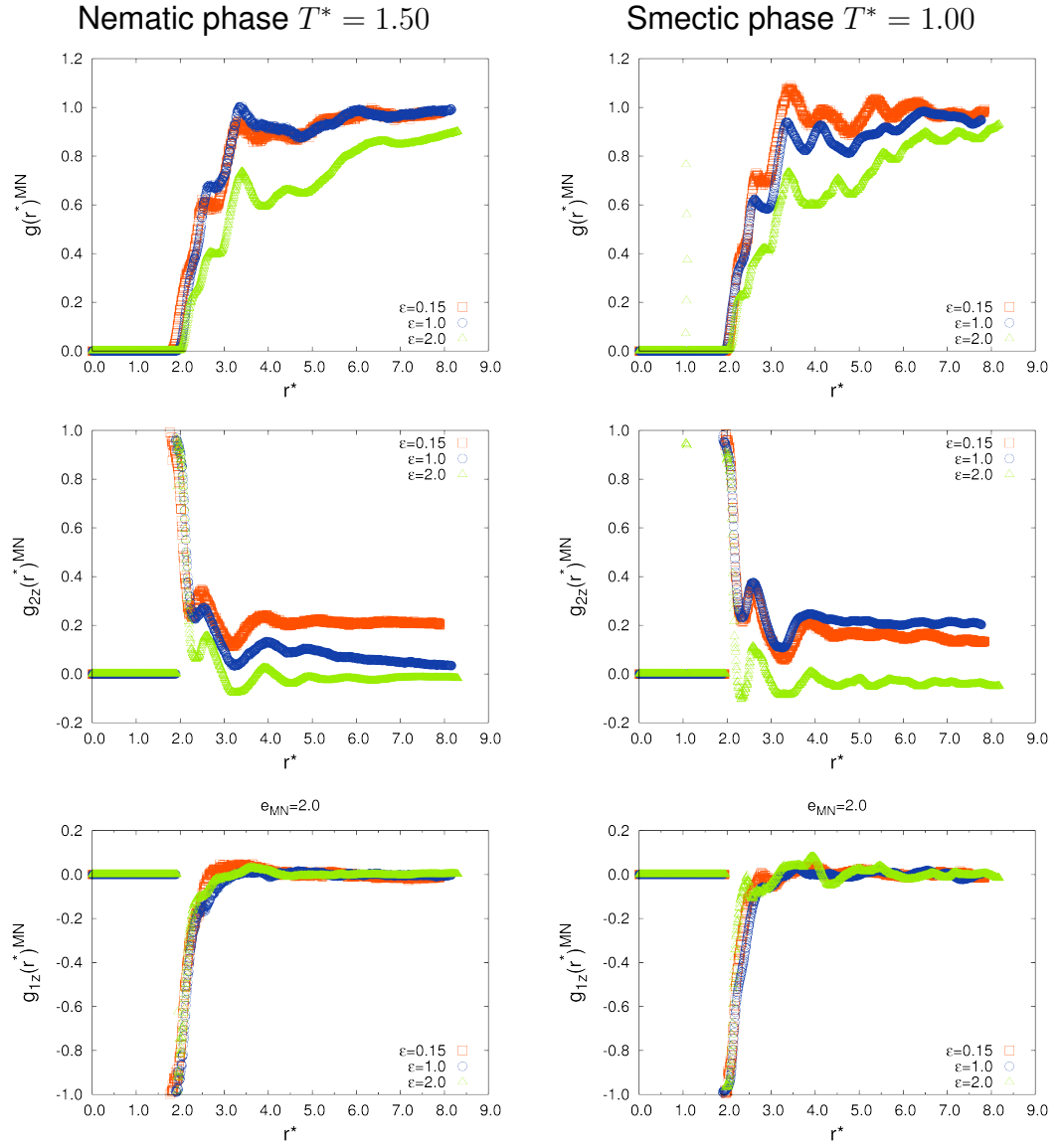


Figure 5.31: Mesogen–nanoparticle  $g(r)^{MN}$  (top),  $g_{2z}(r)^{MN}$  (medium) and  $g_{1z}(r)^{MN}$  (bottom) correlation functions at  $T^* = 1.5$  and  $T^* = 1.0$  for  $\epsilon_S = 0.15, 1.0, 2.0$ .

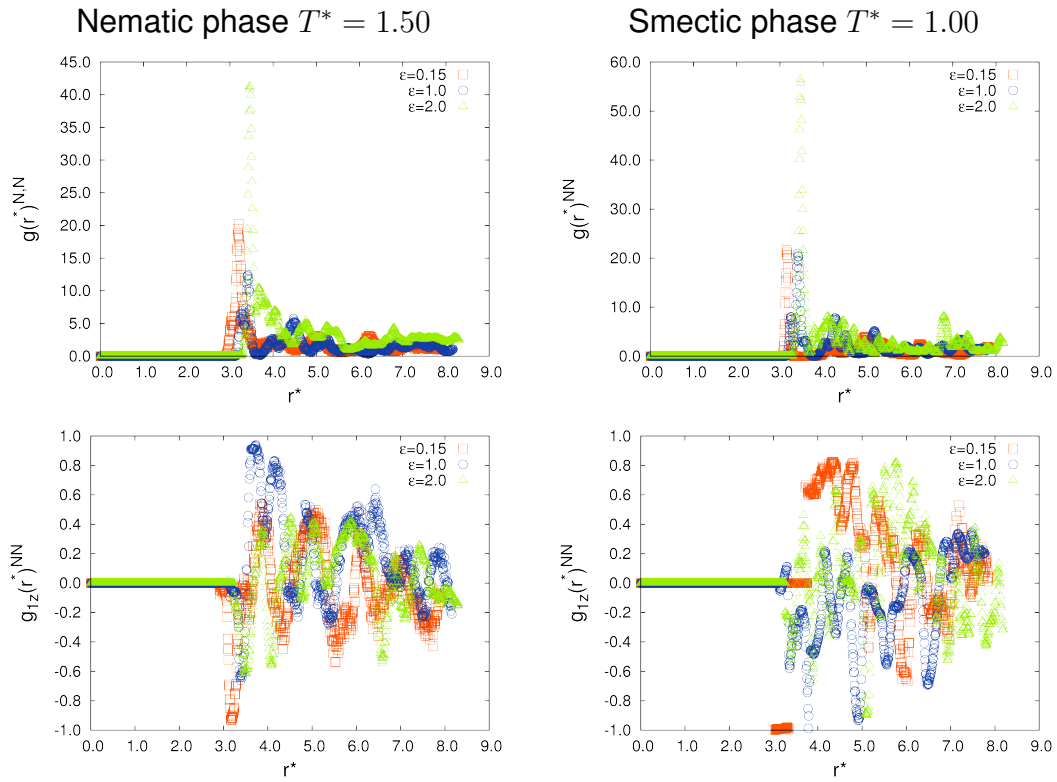
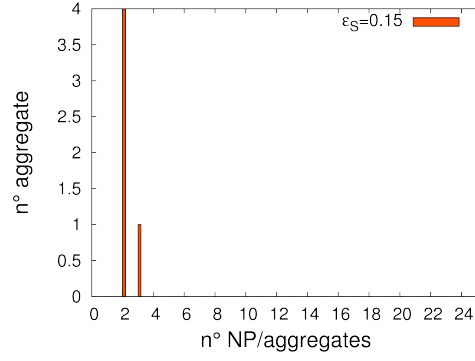


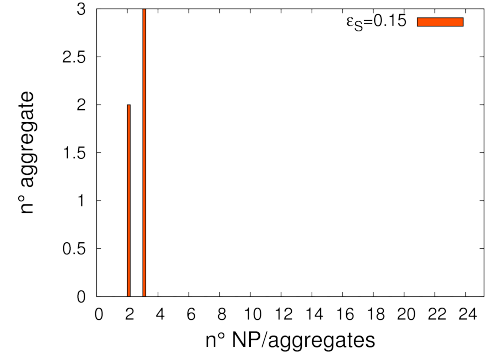
Figure 5.32: Radial correlation functions  $g(r)^{NN}$  and  $g_{1z}(r)^{NN}$  referred to NN particles for  $\epsilon_S = 0.15, 1.0, 2.0$  for reference temperatures in smectic ( $T^* = 1.0$ ) and nematic ( $T^* = 1.5$ ) phase.

Temperature  $T^* = 1.5$  - Nematic phase

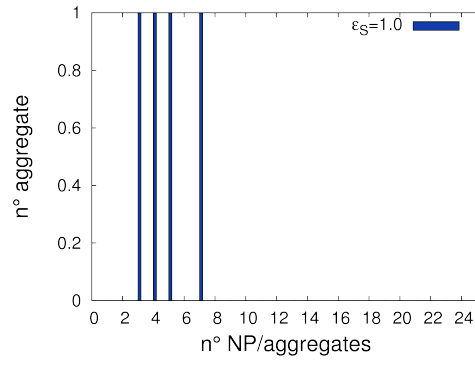
Temperature  $T^* = 1.0$  - Smectic phase



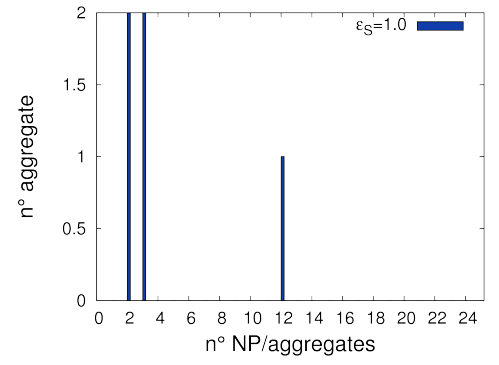
(a)



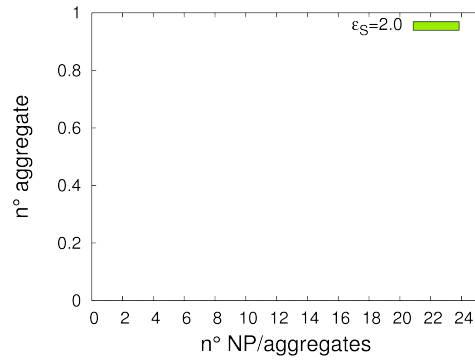
(d)



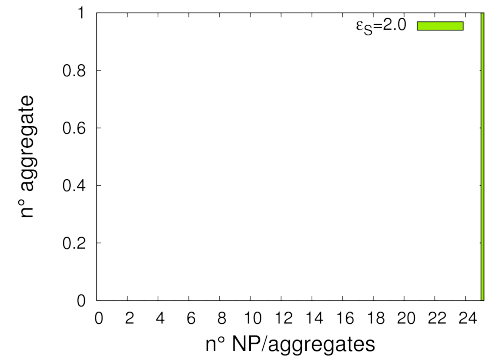
(b)



(e)



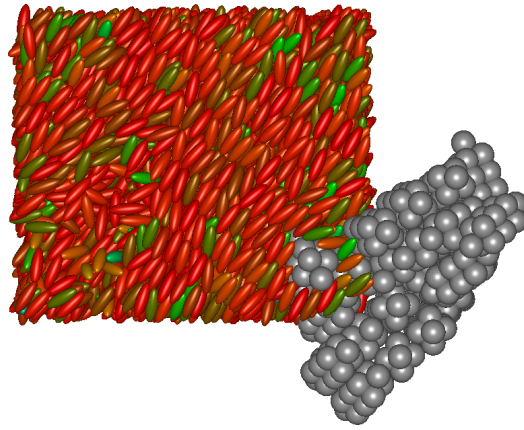
(c)



(f)

Figure 5.33: Nanoparticles aggregates dispersion histograms for  $T^* = 1.5$  (left) and  $T^* = 1.0$  (right) for different values of  $\varepsilon_S$ .





$$T^* = 1.0$$

Figure 5.34: Nanoparticle organization in cluster at temperature  $T^* = 1.0$  for the system with stronger NN interactions ( $\varepsilon_S = 2.0$ ).

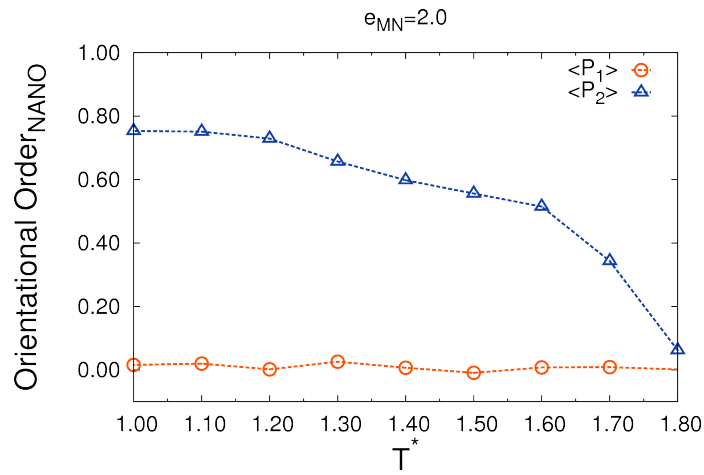


Figure 5.35: Local first  $\langle P_1 \rangle_{LOC}^{NANO}$  and second  $\langle P_2 \rangle_{LOC}^{NANO}$  rank order parameters plotted against temperature.



# Chapter 6

## Conclusions

We have reported the results of Monte Carlo computer simulation studies on systems of rod-like mesogens doped with nanoparticles. In particular, we have focused on the effects of

- nanoparticle shape, considering spherical, rodlike and disc-like cases
- nanoparticle size, relative to that of the mesogen molecules
- strength of the specific interactions between nanoparticles and between nanoparticles and mesogens (solvent affinity)
- polarity of the embedded nanoparticles

on phase behavior, long-range positional and orientational order and overall organization of these mixture systems.

The results clearly show that even a simple model based on a multi-site Gay–Berne potential and dipolar interaction can help to figure out the features which favours the enhancement of the LC order as well as the formation of nanoparticle aggregates.

In particular we found that doping a mesogenic system with nanoparticles of any shape has the overall effect of reducing both the orientational and positional order, with the most disordering effects observed for the embedded spherical nanoparticles.

The specific nanoparticle-solvent interaction has a significant influence in determining the aggregation/dispersion state of the dopant NP, anyway all the mixtures evidence a shift of the TNI temperature towards lower values, if compared with the pure system. The only exception is given by the mesogenic system doped with polar rod-shaped NP with very low solubility features, which essentially shows invariance of the ordering properties and of the relevant transition temperatures. This behavior is related to the formation of nanoparticles aggregates, each aggregate containing a large number ( $> 20$ ) of nanoparticles, overall oriented along the mesophase director. The local arrangement of mesogens around the NP evidences a planar-type anchoring with orientational defects. We can thus claim the overall on stability to be a delicate balance of often contrasting contributions.

These results provide some rationalization elements that we hope will be of help in understanding the effect of NP doping of liquid crystals and in developing a general strategy to control and direct the assembly of NPs in LC.

# Bibliography

- [1] P. G. de Gennes and J. Prost. *"The Physics of Liquid Crystals"*. Clarendon Press, Oxford, 1993.
- [2] I. Dierking. *"Textures of Liquid Crystals"*. Wiley-VCH editor, Weinheim, 2003.
- [3] I. Dierking, W. Blenkhorn, E. Credland, W. Drake, R. Kociuruba, B. Kayser, and T. Michael. "Stabilising liquid crystalline blue phases". *Soft Matter*, 8:4355, 2012.
- [4] R. Tilley. *"Colour and Optical Properties of Materials"*. Wiley, 2000.
- [5] H. Qi, B. Kinkead, and T. Hegmann. "Effects of functionalized metal and semiconductor nanoparticles in nematic liquid crystals". *Proc. SPIE*, 6911:691106, 2008.
- [6] H. Qi and T. Hegmann. "Formation of periodic stripe patterns in nematic liquid crystals doped with functionalized gold nanoparticles". *J. Mat. Chem.*, 16:4197, 2006.
- [7] Y. Shiraishi, N. Toshima, K. Maeds, H. Yoshikawa, J. Xu, and S. Kobayashi. "Frequency modulation response of a liquid-crystal electro-optic device doped with nanoparticles". *Appl. Phys. Lett.*, 81:2845, 2002.
- [8] S. Kobayashi and N. Toshima. "Nanoparticles and LCDs: it's a surprising world". *Society for Information Display*, 9(7):26, 2007.

- [9] H. Yoshida, K. Kawamoto, H. Kubo, T. Tsuda, A. Fujii, S. Kuwabata, and M. Ozaki. "Nanoparticle-dispersed liquid crystals fabricated by sputter doping". *Adv. Mater.*, 22:622, 2010.
- [10] S. Kaur, S. P. Singh, A. M. Biradar, A. Choudhary, and K. Sreeniva. "Cholesterol biosensor based on RF sputtered zinc oxide nanoporous thin film". *App. Phys. Lett.*, 91:023120, 2007.
- [11] A. Kumar, J. Prakash, D. S. Mehta, A. M. Biradar, and W. Haase. "Enhanced photoluminescence in gold nanoparticles doped ferroelectric liquid crystals". *App. Phys. Lett.*, 95:023117, 2009.
- [12] O. Buchnev, A. Dyadyusha, M. Kaczmarek, V. Reshetnyak, and Y. Reznikov. "Enhanced two-beam coupling in colloids of ferroelectric nanoparticles in liquid crystals". *J. Opt. Soc. Am. B*, 24:1512, 2007.
- [13] Yu. Reznikov, O. Buchnev, O. Tereshchenko, V. Reshetnyak, A. Glushchenko, and J. West. "Ferroelectric nematic suspension". *Appl. Phys. Lett.*, 82:1917, 2003.
- [14] F. Li, O. Buchnev, C.I. Cheon, A. Glushchenko, V. Reshetnyak, Y. Reznikov, T. J. Sluckin, and J. L. West. "Orientational coupling amplification in ferroelectric nematic colloids". *Phys. Rev. Lett.*, 97:147801, 2006.
- [15] L. M. Lopatina and J. R. Selinger. "Theory of ferroelectric nanoparticles in nematic liquid crystals". *Phys. Rev. Lett.*, 102:197802, 2009.
- [16] Y. S. Ha, H. J. Kim, H. G. Park, and D. S. Seo. "Enhancement of electro-optic properties in liquid crystal devices via titanium nanoparticle doping". *Opt. Exp.*, 20(6):6448, 2012.
- [17] A. Arcioni, C. Bacchiocchi, L. Grossi, A. Nicolini, and C. Zannoni. "Electron spin resonance studies of order and dynamics in a nematic liquid crystal containing a dispersed hydrophobic aerosil". *J. Phys. Chem. B*, 106:9245–9251, 2002.

- [18] A. Arcioni, C. Bacchiocchi, I. Vecchi, G. Venditti, and C. Zannoni. "A comparison of the effects of dispersed hydrophobic or hydrophilic aerosil nanoparticles on the order and dynamics of the 5CB liquid crystal". *Chem. Phys. Lett.*, 396:433–441, 2004.
- [19] A. Arcioni, C. Bacchiocchi, I. Vecchi, and C. Zannoni. "Glass-like behavior at molecular level induced in a nematic by a dispersion of aerosil nanoparticles". *Mol. Cryst. Liq. Cryst.*, 429:213–225, 2005.
- [20] O. Kurochkin, H. Atkuri, O. Buchnev, A. Glushchenko, O. Grabar, R. Karapinar, V. Reshetnyak, J. West, and Y. Reznikov. "Nano-colloids of Sn<sub>2</sub>P<sub>2</sub>S<sub>6</sub> in nematic liquid crystal pentyl-cianobiphenile". *Cond. Matt. Phys.*, 13(3):33701, 2010.
- [21] V. Domenici, B. Zupancic, V. V. Laguta, A. G. Belous, O. I. Vyunov, M. Remskar, and B. Zalar. "PbTiO<sub>3</sub> nanoparticles embedded in a liquid crystalline elastomer matrix: Structural and ordering properties". *J. Phys. Chem. C*, 114:10782, 2010.
- [22] F. Li, O. Buchnev, C.I Cheon, A. Glushchenko, V. Reshetnyak, Y. Reznikov, T. J. Sluckin, and J. L. West. "Erratum: Orientational coupling amplification in ferroelectric nematic colloids [Phys. Rev. Lett. 97, 147801 (2006)]". *Phys. Rev. Lett.*, 99:219901, 2007.
- [23] E. B. Barmatov, D. A. Pedalk, and M. V. Barmatova. "Influence of silver nanoparticles on the order parameter of liquid crystalline polymers". *Liq. Cryst.*, 33:1059, 2006.
- [24] P. Kopčanský, N. Tomašovičová, M. Koneracká, M. Timko, Z. Mitróová, V. Závišová, N. Éber, K. Fodor-Csorba, T. Tóth-Katona, A. Vajda, J. Jadzyn, E. Beaugnon, and X. Chaud. "Structural phase transition in liquid crystal doped with gold nanoparticles". *Acta Phys. Pol., A*, 33:988, 2010.

- [25] H. Duran, B. Gazdecki, A. Yamashita, and T. Kyu. "Effect of carbon nanotube on phase transitions of nematic liquid crystals". *Liq. Cryst.*, 32(7):815, 2005.
- [26] P. Kopčanský, N. Tomašovičová, M. Koneracká, M. Timko, V. Závišová, A. Džarová, J. Jadzyn, E. Beaunon, and X. Chaud. "Phase transitions in liquid crystal doped with magnetic particles of different shapes". *Liq. Cryst.*, 32 (4):807, 2011.
- [27] G. Cook, J. L. Barnes, S. A. Basun, D. R. Evans, R. F. Ziolo, A. Ponce, V. Y. Reshetnyak, A. Glushchenko, and P. P. Banerjee. "Harvesting single ferroelectric domain stressed nanoparticles for optical and ferroic applications". *J. Appl. Phys.*, 108:064309, 2010.
- [28] J. F. Blach, S. Saitzek, C. Legrand, L. Dupont, J. F. Henninot, and M. Warenthem. "BaTiO<sub>3</sub> ferroelectric nanoparticles dispersed in 5CB nematic liquid crystal : synthesis and electro-optical characterization". *J. Appl. Phys.*, 107:074102, 2010.
- [29] M. R. Herrington, O. Buchnev, M. Kaczmarek, and I. Nandhakumar. "The effect of the size of BaTiO<sub>3</sub> nanoparticles on the electro-optic properties of nematic liquid crystals". *Mol. Cryst. Liq. Cryst.*, 527:72, 2010.
- [30] A. Mertelj, L. Cmok, M. Copic, G. Cook, and D. R. Evans. "Critical behavior of director fluctuations in suspensions of ferroelectric nanoparticles in liquid crystals at the nematic to smectic-A phase transition". *Phys. Rev. E*, 85:021705, 2012.
- [31] A. Lorenz, N. Zimmermann, S. Kumar, D. R. Evans, G. Cook, M. F. Martínéz, and H. S. Kitzerow. "Doping a mixture of two smectogenic liquid crystals with barium titanate nanoparticles". *J. Phys. Chem. B*, 117:937, 2013.



- [32] A. Lorenz, N. Zimmermann, S. Kumar, D. R. Evans, G. Cook, M. F. Martínéz, and H. S. Kitzerow. "X-ray scattering of nematic liquid crystal nanodispersion with negative dielectric anisotropy". *App. Opt.*, 52(22):E1, 2013.
- [33] W. Cai and V. Shalaev. *"Optical Metamaterials: Fundamentals and Applications"*. Springer, 2009.
- [34] M. Draper, I. M. Saez, S. J. Cowling, P. Gai, B. Heinrich, B. Donnio, D. Guillon, and J. W. Goodby. "Self-assembly and shape morphology of liquid crystalline gold metamaterials". *Adv. Funct. Mater.*, 21:1260, 2011.
- [35] H. Yoshida, Y. Tanaka, K. Kawamoto, H. Kubo, T. Tsuda, A. Fujii, S. Kuwabata, H. Kikuchi, and M. Ozaki. "Nanoparticle-stabilized cholesteric blue phases". *Appl. Phys. Express*, 2, 2009.
- [36] V. Y. Reshetnyak, S. M. Shelestiuk, and T. J. Sluckin. "Freedericksz transition threshold in nematic liquid crystals filled with ferroelectric nano-particles". *Mol. Cryst. Liq. Cryst.*, 454:201, 2006.
- [37] S. M. Shelestiuk, V. Y. Reshetnyak, and T. J. Sluckin. "Frederiks transition in ferroelectric liquid crystal nano-suspensions". *Phys. Rev. E*, 83:041705, 2011.
- [38] M. S. S. Pereira, A. A. Canabarro, I. N. de Oliveira, M. L. Lyra, and L. V. Mirantsev. "A molecular dynamics study of ferroelectric nanoparticles immersed in a nematic liquid crystal". *Eur. Phys. J. E*, 31:81, 2010.
- [39] L. M. Lopatina and J. R. Selinger. "Maier-saupe-type theory of ferroelectric nanoparticles in nematic liquid crystals". *Phys. Rev. E*, 84:041703, 2011.
- [40] M. P. Allen and D. J. Tildesley. *"Computer Simulations"*. Oxford University Press, Oxford, 1989.

- [41] C. Frenkel and B. Smit. *"Understanding Molecular Simulation"*. Academic Press, 2002.
- [42] P. Pasini and C. Zannoni. *"Advances in the computer simulations of liquid crystals"*. Kluwer, 2000.
- [43] D. C. Rapaport. *"The art of molecular dynamics simulation"*. Cambridge U.P., 2004.
- [44] N. Metropolis, A. W. Rosenbluth, M. N. Rosenbluth, E. Teller, and M. N. Teller. "Equation of state calculations by fast computing machines". *J. Chem. Phys.*, 21:1087–1092, 1953.
- [45] N. G. van Kampen. *"Stochastic Processes in Physics and Chemistry"*. Elsevier, 1992.
- [46] W. W. Wood. "Monte Carlo calculations for hard disks in the isothermal–isobaric ensemble". *J. Chem. Phys.*, 48:415, 1968.
- [47] B.J. Alder and T.E. Wainwright. "Studies in molecular dynamics and I. General method". *J. Chem. Phys.*, 31:459–466, 1959.
- [48] L. Verlet. "Computer experiments on classical fluids. I. Thermodynamical properties of Lennard–Jones molecules". *Phys. Rev.*, 159:98–103, 1967.
- [49] W.C. Swope and H.C. Andersen. "A molecular dynamics method for calculating the solubility of gases in liquids and the hydrophobic hydration of inert gas atoms in aqueous solution.". *J. Phys. Chem.*, 88:6548, 1984.
- [50] W.C. Swope, H. C. Andersen, P. H. Berens, and K. R. Wilson. "A computer simulation method for the calculation of equilibrium constants for the formation of physical clusters of molecules: application to small water clusters". *J. Chem. Phys.*, 76:637, 1982.

- [51] R. Car and M. Parrinello. "Unified approach for molecular dynamics and density–functional theory". *Phys. Rev. Lett.*, 55 (22):2471, 1985.
- [52] J. Baschnagel, K. Binder, W. Paul, M. Laso, U. W. Suter, I. Batoulis, W. Jilge, and T. Buerger. "On the construction of coarse-grained models for linear flexible polymer chains: distribution functions for groups of consecutive monomers". *J. Chem. Phys.*, 95:6014–6025, 1991.
- [53] C. Zannoni. "Molecular design and computer simulations of novel mesophases". *J. Mat. Chem.*, 11:2637–2646, 2001.
- [54] M. R. Wilson. "Progress in computer simulations of liquid crystals". *Internat. Rev. Phys. Chem.*, 24:421–455, 2005.
- [55] D. J. Michel and D. J. Cleaver. "Coarse-grained simulation of amphiphilic self-assembly". *J. Chem. Phys.*, 126, 2007.
- [56] M. P. Allen, G. T. Evans, D. Frenkel, and B. M. Mulder. "Hard convex body fluids". *Advances in Chemical Physics*, 86:1–166, 1993.
- [57] B. Senyuk. "Liquid crystals: a simple view on a complex matter". Website. <http://dept.kent.edu/spie/liquidcrystals/maintypes.html>.
- [58] J. G. Gay and B.J. Berne. "Modification of the overlap potential to mimic a linear site-site potential". *J. Chem. Phys.*, 74:3316, 1981.
- [59] J. E. Jones. "On the determination of molecular fields". *Proc. Roy. Soc. London*, 106:463, 1924.
- [60] J. Xu, D. Bedrov, and G. D. Smith. "A molecular dynamics simulation study of spherical nanoparticles in a netogenic matrix: Anchoring, interactions and phase behavior". *Phys. Rev. E*, 79:011704, 2009.
- [61] J. K. Whitmer, A. A. Joshi, T.F. Roberts, and J.J. de Pablo. "Liquid-crystal mediated nanoparticle interactions and gel formation". *J. Chem. Phys.*, 138:194903, 2013.

- [62] C. Zannoni, G. R. Luckhurst, and G. W. Gray. "Distribution function and order parameters". In *The Molecular Physics of Liquid Crystals*, volume Chap. 3, pages 51–83. Academic Press, 1979.
- [63] M.E. Rose. *"Elementary Theory of Angular Momentum"*. Wiley, New York, 1957.
- [64] M. Abramovitz and I.A. Stegun. *"Handbook of Mathematical Functions"*. Dover, New York, 1964.
- [65] F. Biscarini, C. Chiccoli, P. Pasini, and C. Zannoni. "Head-tail asymmetry and ferroelectricity in uniaxial liquid crystals. Model calculations". *Mol. Phys.*, 73:439, 1991.
- [66] E. De Miguel, L. F. Rull, M. K. Chalam, and K. E. Gubbins. "Liquid crystal phase diagram of the Gay-Berne fluid". *Mol. Phys.*, 74:405, 1991.
- [67] R. Berardi, S. Orlandi, and C. Zannoni. "Monte Carlo simulation of discotic Gay-Berne mesogens with axial dipole". *J. Chem. Soc. Faraday Trans.*, 93:1493–1496, 1997.
- [68] U. Fabbri and C. Zannoni. "A Monte Carlo investigation of the Lebwohl–Lasher lattice model in the vicinity of its orientational phase transition". *Mol. Phys.*, 58:763, 1986.
- [69] J. Vieillard-Baron. "The equation of state of a system of hard spherocylinders". *Mol. Phys.*, 28:809, 1974.
- [70] R. Eppenga and D. Frenkel. "Monte-Carlo study of the isotropic and nematic phases of infinitely thin hard platelets". *Mol. Phys.*, 52:303, 1984.
- [71] A. P. J. Emerson, R. Hashim, and G. R. Luckhurst. "Computer simulation studies of anisotropic systems XX. On the validity of the Maier–

- Saupe approximations for the Gay-Berne nematogen". *Mol. Phys.*, 76:241, 1992.
- [72] R. I. Humphries, P. G. James, and G. R. Luckhurst. "Molecular field treatment of nematic liquid crystals". *J. Chem. Soc. Faraday Trans. 2*, 68:1031, 1972.
- [73] F. Barmes. "*Computer simulation of confined and flexoelectric liquid crystalline systems*". PhD thesis, Sheffield Hallam University, Great Britain, 2003.
- [74] M. J. Chalam, K. E. Gubbins, E. de Miguel, and L. F. Rull. "A molecular simulation of a liquid crystal model: bulk and confined fluid". *Molecular Simulation*, 7:357, 1991.
- [75] E. de Miguel, L. F. Rull, M. J. Chalam, and K. E. Gubbins. "Location of the isotropic–nematic transition in the gay-berne model". *Molecular Physics*, 72:593, 1991.
- [76] E. de Miguel, L. F. Rull, M. J. Chalam, and K. E. Gubbins. "Liquid crystal phase diagram of the Gay-Berne fluid". *Molecular Physics*, 74:405, 1991.
- [77] R. Berardi, C. Fava, and C. Zannoni. "A Gay–Berne potential for dissimilar biaxial particles". *Chem. Phys. Lett.*, 297 (1):8–14, 1998.
- [78] R. Berardi, S. Orlandi, and C. Zannoni. "Antiphase structures in polar smectics liquid crystals and their molecular origin". *Chem. Phys. Lett.*, 363–368:1996, 261.
- [79] R. Berardi, S. Orlandi, D. J. Photinos, A. G. Vanakaras, and C. Zannoni. "Dipole strength effects on the polymorphism in smectic A mesophases". *Phys. Chem. Chem. Phys.*, 4:770–777, 2002.

- [80] L. Querciagrossa, M. Ricci, R. Berardi, and C. Zannoni. "Mesogen polarity effects on biaxial nematics. Centrally located dipoles". *Phys. Chem. Chem. Phys.*, 15:19065–19072, 2013.
- [81] Ewald P. "Die Berchnung Optischer Und Elektrostatischer Gitterpotentiale". *Ann. Phys.*, 64:253, 1921.
- [82] S. W. De Leeuw, J. W. Perram, and E. R. Smith. "Simulation of electrostatic systems in periodic boundary conditions I. Lattice sums and dielectric constants". *Proc. R. Soc. Lond. A*, 373:27, 1980.
- [83] P. G. Kusalik. "Computer simulation results for the dielectric properties of a highly polar fluid". *J. Chem. Phys.*, 93:3520, 1990.
- [84] A. Gil-Vilegas, S. McGrother, and G. Jackson. "Reaction-field and Ewald summation methods in Monte Carlo simulations of dipolar liquid crystals". *Mol. Phys.*, 92:723, 1997.
- [85] L. Osanger. "Electric moments of molecules in liquids". *J. Am. Chem. Soc.*, 107:1486, 1936.